LOUGHBOROUGH UNIVERSITY

DOCTORAL THESIS

Solidification and structure formation in soft-core fluids

Author:

Morgan WALTERS

Supervisor:

Dr. Andrew ARCHER

A thesis submitted in fulfilment of the requirements

for the degree of Doctor of Philosophy

in the

Mathematical modelling group within the

Department of Mathematical Sciences.

November 8, 2017

Abstract

This thesis analyses the structure, phase behaviour and dynamics of two dimensional (2D) systems of interacting soft-core particles, focussing in particular on how these can solidify and the properties of the resulting crystalline structures. Classical density functional theory (DFT) and dynamical density functional theory (DDFT) is used in the analysis, and an introduction to these is given. The first systems studied are particles interacting via the generalised exponential model of index n (GEM-n) pair potential, including binary mixtures of different types of GEM-n particles. We confirm that a simple mean-field approximate DFT (the RPA-DFT) provides a good approximation for the structure and thermodynamics. We study how solidification fronts advance into the unstable liquid after a temperature quench. We find that the length scale of the density modulations chosen by the front is not necessarily the length scale corresponding the equilibrium crystal structure. This results in the presence of defects and disorder in the structures formed. We analyse how these evolve over time, after the front has passed. We also find that for the binary mixtures, the defects and disorder persists for much longer and in-fact can remain indefinitely.

In the final part of this thesis we analyse the Barkan-Engel-Lifshitz (BEL) model, which consists of particles interacting via a soft core potential that is more complicated than the GEM-n potential and can include a minimum in the potential and soft repulsion over several competing length scales. The form of the BEL potential gives good control over the shape of the dispersion relation, which allows it to be tuned to the regime where the system forms quasicrystals. In this regime, we study in detail the nature of the liquid state pair correlations and in particular the form of the asymptotic decay as the distance between the particles $r \to \infty$. The usual approach used for fluids in three dimensions has to be generalised, in order to be applicable in 2D. It is found that there is a line in the phase diagram at which the asymptotic decay crosses over from being oscillatory with one wavelength to oscillatory with a different wavelength. We expect this to be a

general characteristic of systems that form quasicrystals.

Acknowledgements

I would first like to thank my supervisor Andrew Archer for his help and support throughout this PhD, he is alway happy to make time for his students, which I am very thankful for. This thesis simply would not have been a reality without him. I would also like to thank my colleagues for making the office a enjoyable place to be. Lastly I would like to thank my family for all the encouragement throughout my time in Loughborough.

My work in chapters 2 to 6 of this thesis was published in:

A.J. Archer, M.C. Walters, U. Thiele, E. Knobloch, *Solidication in soft-core fluids: disordered solids from fast solidication fronts*, Phys. Rev. E **90**, 042404 (2014)

A.J. Archer, M.C. Walters, U. Thiele, E. Knobloch, *Generation of defects and disorder from deeply quenching a liquid to form a solid*, Springer Proceedings in Mathematics and Statistics **166**, 1 (2016)

Chapter 7 is original work not yet submitted for publication.

Contents

List of Figures

Chapter 1

Introduction

An important focus of material science and physics is to understand as much as possible about the way different substances behave whether in gas, liquid or solid form. There are many experiments we can do in the 21st century to observe, even at the microscopic level, this behaviour. However it is not always cost effective (in money or time) to do this, which is why the study of accurate theoretical models and computer simulations is very important; they allow us to determine material properties with comparatively little expenditure. There are a variety of different modelling and simulation techniques designed to study the gas, liquid and solid phases of materials. In this thesis we focus on using classical density functional theory (DFT) and dynamical density functional theory (DDFT) to study "soft-core" systems in their liquid and solid phases and in particular how the solid forms from the uniform liquid. Both of these techniques and what we mean by "soft-core" systems, are discussed in more detail below and in subsequent chapters. DFT [1, 2, 3, 4] is a theoretical tool, that can be used to model a variety of natural phenomena, for example: the way liquids behave next to a wall, to determine the effective interactions between larger particles in a solvent made up from much smaller molecules [5] and the structures formed as a liquid is frozen [6]. We present an overview of DFT in Sec 2.2, but first we discuss the nature of the interactions between particles in a fluid and how different fluids are modelled via different pair potentials.

1.1 Pair potentials

The pair potential $v(\mathbf{r})$, where $\mathbf{r}$ is the distance between the pair of particles, defines the energy from the interaction between a pair of particles in the system. The form of the pair potential, whether to input into theory or simulation, depends heavily on the type of molecules being studied. An important piece of information is to know how they interact with each other. In colloid and soft matter science the potential used is often an effective or coarse grained potential [7]. In this section we discuss a few of the different models that are often considered, ranging from hard core to soft core potientials. In Fig 1.1 we see two examples of widely known and used potentials; On the left of Fig 1.1 is displayed the 12-6 potential of Lennard-Jones [3]:

$$v(\mathbf{r}) = 4\epsilon \left[\left(\frac{\sigma}{r}\right)^{12} - \left(\frac{\sigma}{r}\right)^{6} \right], \tag{1.1}$$

where $r = |\mathbf{r}|$ is the distance between the centres of the particles and on the right of Fig 1.1 is the generalised exponential model of index n (GEM-n) potential [7],

$$v(\mathbf{r}) = \epsilon e^{-(r/R)^n}, \tag{1.2}$$

with $n = 8$. In both potentials ϵ determines the interaction energy. An important distinction between these two pair potentials is that in the hard-core cases, such as the Lennard-Jones, there is a strong repulsion between the molecules that prevent them from occupying the same space i.e. they cannot come any closer than one molecular diameter from each other at all reasonable values of the pressure. Studying the Lennard-Jones potential in Fig 1.1 this distinction is realised when noting that generally the potential $v(r)/k_BT >> 1$ for $r < \sigma$, where σ is the diameter of the particles and k_BT is the thermal energy of a typical particle collision; T is the temperature and k_B is the Boltzmann's constant. The part of the potential with the positive gradient, for $\frac{r}{\sigma} \geq 2^{1/6}$, is an attractive region of this particular

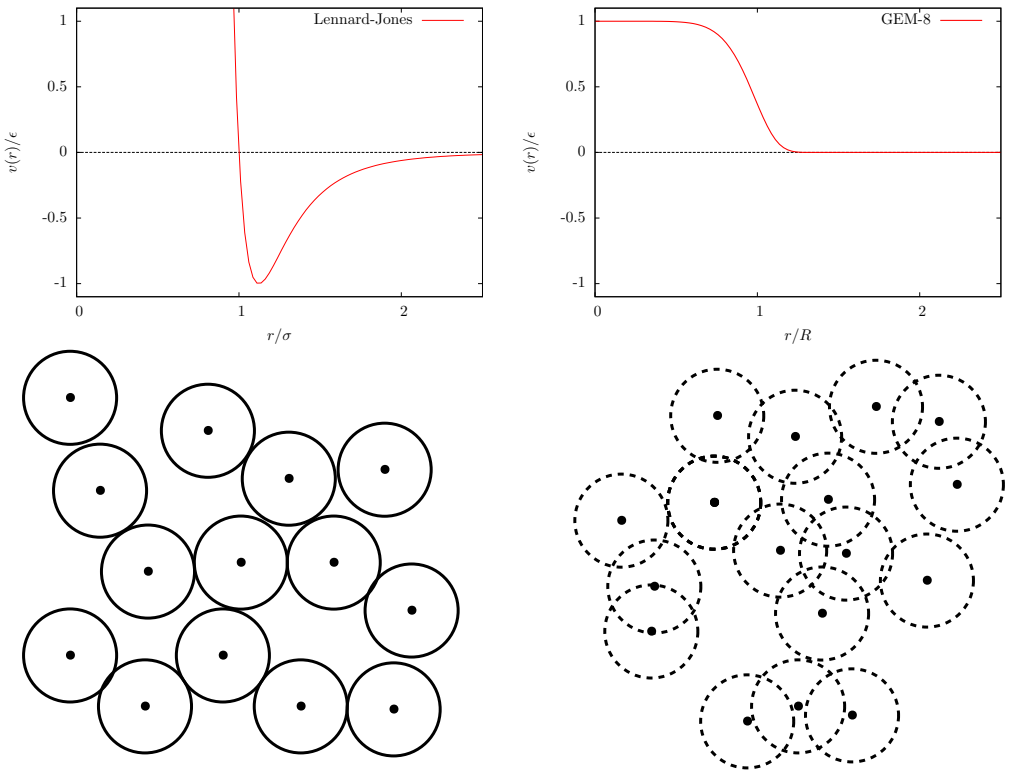

FIGURE 1.1: Examples of potentials for modelling the interactions between fluid particles. In the top left is displayed the Lennard-Jones potential and in the top right the GEM-8 potential. Two sketches of typical configurations of the molecules are shown below.

potential i.e. the molecules want to cluster around each other. In comparison the GEM-n potential in Fig 1.1 (right) is purely repulsive but does allow for molecules to occupy the same space. Note that the value of $v(r \to 0) = \epsilon$, means that the energy remains finite when the particles of radius R are completely overlapping, with value ϵ.

Such soft-core pair potentials typically arise as the effective potentials between the centres of mass of large polymeric molecules in solution. In Fig. 1.2 we sketch a pair of polymer chains in solution. Due to the string-like nature of the molecules, the centres of mass can be close or even coincide in space. To model this kind of system the polymers can be treated as soft 'blobs' that can penetrate one another with effective potential similar to the potential in Eq. (1.2).

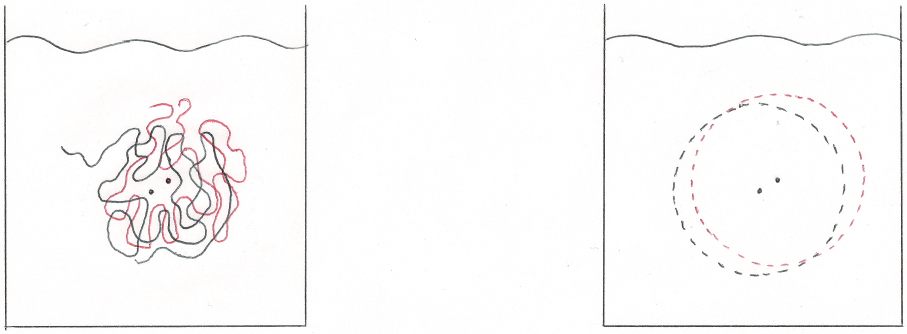

FIGURE 1.2: Sketch to show (left) an example of a pair of polymer chains in solution and (right) the approximation we make in the model for these, as soft penetrable 'blobs'. The points mark the locations of the centres of mass.

1.1.1 Generalised exponential model

In this thesis we consider two dimensional (2D) systems of soft-core particles interacting via the GEM-n pair-potential Eq. (1.2) where the parameter $0 < \epsilon < \infty$ determines the energy penalty for a pair of particles to overlap as they approach one another, R is the radius of the particles and the exponent n determines the 'softness' of the potential. When $n = 2$, the potential varies slowly. In contrast, when n is large, as the separation distance r between a pair of particles is decreased, the potential increases rapidly from ≈ 0 to a value $\approx \epsilon$ over a short distance at $r = R$ - see Fig 1.3. Here, we consider the cases when $n = 4$ and $n = 8$. There is an extensive literature showing how such soft potentials arise as the effective interaction potential between polymers or other such soft macromolecules in solution [7, 8, 9, 10, 11, 12, 13, 14, 15, 16, 17, 18, 19].

The GEM-n potential in Eq. (1.2) with $n = 4, 8$ is a simple effective pair potential used to model the effective potentials between the centres of mass of dendrimers in solution [7, 19], which are branched polymers having a tree-like structure. We also expect this potential to roughly mimic the effective potential between certain star polymers. In Fig. 1.3 we plot the potential [Eq. (1.2)] for several different values of n. Note that when $n = 2$ the GEM is instead called the Gaussian Core model (GCM) and is a good model for simple linear polymers in solution [20, 21]. The lower the index n, the "softer" the molecules in the system.

Fig 1.3 shows the progression of how these potentials change with n. The parameter $0 < \epsilon < \infty$ determines the energy penalty for a pair of particles to overlap completely, when $r < R$. The GEM-n potiential with larger n is a model for polymeric molecules that are more compact [17, 19], as can be seen in Fig. 1.3; the blue line is GEM-4, with $n = 4$ and $\beta\epsilon = 1$ in Eq. (1.2), where $\beta = 1/k_BT$. In this case, the soft repulsion becomes sizeable at $\frac{r}{R} \approx 1.5$. The red line is GEM-8 where the soft particles begin repulsing each other at $\frac{r}{R} \approx 1.25$ and the green line shows the trend as $n \to \infty$, in this case the particles exert the full overlap energy $v(r) = \epsilon$, as soon as they come into contact with each other, for $r < R$. Before discussing the structure, phase behaviour and dynamics of the GEM-n model for soft, we first explain the principles of equilibrium DFT and its origins in thermodynamics.

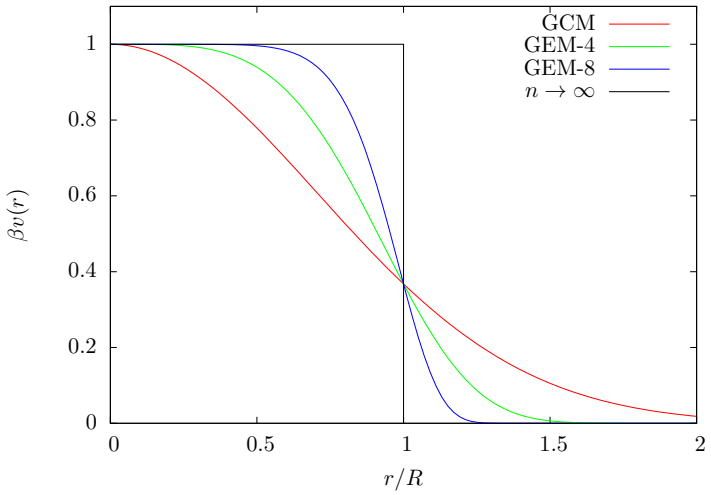

FIGURE 1.3: GEM-n pair potential for $\beta\epsilon = 1$ where $n = 4$, $n = 8$ and the $n \to \infty$ limit. We also show the Gaussian Core Model (GCM), i.e. the GEM-n, when $n = 2$.

Chapter 2

Theory for the equilibrium system

2.1 Laws of thermodynamics

We approach Density Functional Theory (DFT) from thermodynamic principles. The more standard presentation via statistical mechanics can be found in Refs. [1, 2]. The first law of thermodynamics is a statement that energy is conserved in a system. Thus it can be expressed as:

$$dU = dQ + dW, \tag{2.1}$$

where dU is the change in the internal energy, which depends on the heat transfer to the system, dQ, and the work done on the system, dW. In order to continue this explanation, we must consider the ensemble we are working within. The thermodynamic state of a system can be determined via statistical mechanics i.e. determining the average state of the system. This averaging can be performed by considering an ensemble of copies of the system and averaging over the ensemble. There are various ensembles within which it is possible to study a system. The three of most relevance here are the micro-canonical, canonical and grand canonical emsembles. The micro-canonical ensemble is a closed system with fixed volume V, energy U and a fixed number of molecules N. The canonical ensemble is a system which also has fixed V and N, however it can exchange energy with a heat bath leading to it having a fixed temperature T. The Grand canonical ensemble is a system which has fixed T and can exchange both energy

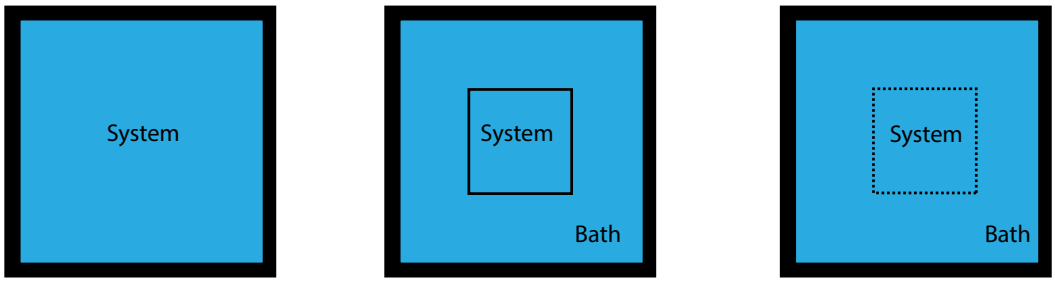

FIGURE 2.1: Sketch of the three ensembles mentioned above: Left the micro-canonical ensemble. Middle: The canonical ensemble. Right: The grand canonical ensemble. The thick black line denotes the boundary through which neither heat nor particles can penetrate. The thin solid line denotes a boundary through which heat can be exchanged, but not particles. The dashed line defines a boundary through which both can pass.

and particles with the heat bath-see Fig.2.1. That it can exchange particles means the chemical potential μ is fixed equal to that in the bath. In this thesis we largely work within the grand canonical ensemble, in which Eq. (2.1) becomes:

$$dU \leq T\,dS - p\,dV + \mu\,dN \tag{2.2}$$

where the volume V, temperature T and the chemical potential μ are all fixed. The term $TdS \geq dQ$ is the heat supplied to the system, where S is the entropy. Since we have fixed V, therefore $dV = 0$ so:

$$\begin{aligned} 0 &\geq dU - T\,dS - \mu\,dN \\ 0 &\geq d\Omega. \end{aligned} \tag{2.3}$$

We now have an expression for the change in the grand potential $d\Omega$ where Ω is defined as:

$$\begin{aligned} \Omega &= U - TS - \mu N \\ \Omega &= F - \mu N, \end{aligned} \tag{2.4}$$

where $F = U - TS$ is the Helmoltz free energy. Thus, from Eq. (2.3) we see that in a grand canonical system, Ω is minimised at equilibrium. We now introduce the number density ρ, which for a uniform system $\rho = \frac{N}{V}$, is the average number

of particles per unit volume. We can now rewrite Eq. (2.4) as:

$$\Omega = \int_V d\mathbf{r}\, f - \int_V d\mathbf{r}\, \mu\rho \tag{2.5}$$

where $\mathbf{r}$ is a continuous vector representing the coordinates of the system. When we consider an inhomogeneous fluid, the density throughout the system varies in space, therefore the number density ρ becomes a function of $\mathbf{r}$. Hence Eq. (2.6) becomes:

$$\Omega[\rho(\mathbf{r})] = \int d\mathbf{r}\, f[\rho(\mathbf{r})] - \mu \int d\mathbf{r}\, \rho(\mathbf{r}) \tag{2.6}$$

or

$$\Omega[\rho(\mathbf{r})] = F[\rho(\mathbf{r})] - \mu \int d\mathbf{r}\, \rho(\mathbf{r}). \tag{2.7}$$

This equation is known as the grand potential functional. With a suitable expression for the Helmholtz free energy functional $F[\rho]$ we can use this equation to find the density profile $\rho(\mathbf{r})$ that minimises $\Omega[\rho]$ and so is the density profile of the equilibrium system.

2.2 Density Functional Theory

Density Functional Theory (DFT) is a theoretical framework that provides a method for calculating the one-body density profile $\rho(\mathbf{r})$ of an inhomogenous system of classical particles and also thermodynamic quantities such as the pressure and interfacial tension. The quantity $\rho(\mathbf{r})d\mathbf{r}$ is the probability of finding a particle in small volume $d\mathbf{r}$ at position $\mathbf{r}$ in the system and is obtained by minimising the grand potential functional $\Omega[\rho]$ with respect to variations in $\rho(\mathbf{r})$ [3, 13]. The Grand potential functional is given in Eq. (2.7). The first term $F[\rho(\mathbf{r})]$ is the Helmholtz free energy and the second term is the contribution due to the system being coupled to a reservoir with chemical potential μ (the energy required for a particle to enter the system). The Helmholtz free energy can be written as:

$$F[\rho(\mathbf{r})] = k_B T \int d\mathbf{r}\rho(\mathbf{r})(\ln[\Lambda^d \rho(\mathbf{r})] - 1) + F_{ex}[\rho(\mathbf{r})] + \int d\mathbf{r}\rho(\mathbf{r})V_{ext}(\mathbf{r}). \tag{2.8}$$

The first term is the ideal gas free energy, the second term is the excess free energy and the third term is the energy due to the external potential $V_{ext}(\mathbf{r})$, for example due to container walls, etc. Other terms are the thermal de Broglie wavelength Λ and the dimensionality of space d. Substituting Eq. (2.8) into Eq. (2.7) we get (with $d = 2$):

$$\Omega[\rho(\mathbf{r})] = k_B T \int d\mathbf{r}\rho(\mathbf{r})(\ln[\Lambda^2 \rho(\mathbf{r})] - 1) + F_{ex}[\rho(\mathbf{r})] + \int d\mathbf{r}\rho(\mathbf{r})(V_{ext} - \mu). \tag{2.9}$$

The equilibrium density profile is obtained by minimising Eq. (2.9). So, we need to find the density profile $\rho^*(\mathbf{r})$ such that it minimises Ω, i.e. it satisfies the Euler Lagrange equation:

$$\left.\frac{\delta\Omega[\rho(\mathbf{r})]}{\delta\rho(\mathbf{r})}\right|_{\rho(\mathbf{r})=\rho^*(\mathbf{r})} = 0 \tag{2.10}$$

Thus, combining Eq. (2.9) and Eq. (2.10) we obtain:

$$k_B T \ln[\Lambda^2 \rho(\mathbf{r})] + \frac{\delta F_{ex}}{\delta\rho} + V_{ext}(\mathbf{r}) - \mu = 0. \tag{2.11}$$

The excess free energy in Eq. (2.11) is in general an unknown quantity, however, there are a great many approximations that have been developed and the one used depends heavily on the system being modelled. We are here interested in soft macromolecules such as polymers, star-polymers and dendrimers. There are different approaches to approximating the excess free energy, two such approaches are detailed below in section 2.2.1. Once an appropriate approximation for the excess free energy has been found, we then substitute this into Eq. (2.11) and rearrange for the density $\rho(\mathbf{r})$. For example, one of the approximations from section 2.2.1 below [Eq. (2.18)] gives:

$$\frac{\delta F_{ex}}{\delta \rho} \approx \mu_{ex} - k_B T \int d\mathbf{r}' c^{(2)}(\mathbf{r}, \mathbf{r}')(\rho(\mathbf{r}') - \rho_0), \tag{2.12}$$

where $c^{(2)}(r)$ is the (Ornstein-Zernike) pair direct correlation function (this is treated as an input to the theory) and ρ_0 is a reference density and μ_{ex} is the excess chemical potential of the bulk fluid with density ρ_0. Thus:

$$\mu_{ex} = \mu - k_B T \ln \Lambda^2 \rho_0. \tag{2.13}$$

Once an appropriate approximation for the excess free energy has been chosen, we then substitute this into Eq (2.11) and Eq. (2.9), and we can then use this to calculate, via Picard iteration, the density profile $\rho(\mathbf{r})$ and the grand potential energy $\Omega[\rho(\mathbf{r})]$, respectively. Using Eq. (2.12) together with Eq. (2.11), we obtain:

$$k_B T \ln[\Lambda^2 \rho(\mathbf{r})] - k_B T \int d\mathbf{r}' c^{(2)}(\mathbf{r}, \mathbf{r}')(\rho(\mathbf{r}') - \rho_0) + V_{ext}(\mathbf{r}) + \mu_{ex} - \mu = 0 \tag{2.14}$$

Rearranging this expression for the density $\rho(\mathbf{r})$ and using Eq. (2.13) we get:

$$\rho(\mathbf{r}) = \rho_0 e^{\int d\mathbf{r}' c^{(2)}(\mathbf{r},\mathbf{r}')(\rho(\mathbf{r}')-\rho_0) - \beta V_{ext}(\mathbf{r})}. \tag{2.15}$$

This equation is the basis for solving the DFT via Picard iteration. Picard iteration is a process which starts by choosing a suitable initial approximation for $\rho(\mathbf{r})$,

then using the right hand side of Eq. (2.15) we obtain a new approximation for $\rho(\mathbf{r})$. We iteratively solve to find the equilibrium density profile, generally with some mixing of the new and the old profile at each iteration, see Appendix A [22, 23].

2.2.1 Approximations for the excess free energy

Approximating the excess free energy F_{ex} accurately is an important focus of classical DFT. One possible approach is to approximate the excess free energy using a Taylor expansion in powers of $\tilde{\rho}(\mathbf{r}) = \rho(\mathbf{r}) - \rho_0$, where ρ_0 is a reference density:

$$\begin{aligned} F_{ex}[\rho(\mathbf{r})] = F_{ex}[\rho_0] + \int d\mathbf{r}\tilde{\rho}(\mathbf{r}) \left.\frac{\delta F_{ex}[\rho(\mathbf{r})]}{\delta\rho(\mathbf{r})}\right|_{\rho_0} \\ + \frac{1}{2}\int\int d\mathbf{r}d\mathbf{r}'\tilde{\rho}(\mathbf{r})\tilde{\rho}(\mathbf{r}') \left.\frac{\delta F^2_{ex}[\rho(\mathbf{r})]}{\delta\rho(\mathbf{r})\delta\rho(\mathbf{r}')}\right|_{\rho_0} + O(\tilde{\rho}^3). \end{aligned} \tag{2.16}$$

By definition [1, 2] the first and second derivatives of the excess free energy can be expressed as follows:

$$\begin{aligned} \frac{\delta F_{ex}[\rho(\mathbf{r})]}{\delta\rho(\mathbf{r})} &= -k_B T c^{(1)}(\mathbf{r}) \\ \frac{\delta F^2_{ex}[\rho(\mathbf{r})]}{\delta\rho(\mathbf{r})\delta\rho(\mathbf{r}')} &= -k_B T c^{(2)}(\mathbf{r},\mathbf{r}'), \end{aligned} \tag{2.17}$$

where $c^{(1)}$ and $c^{(2)}$ are the one and two body direct correlation functions respectively. So Eq. (2.16) is a Taylor expansion with respect to the direct correlation functions. If we substitute in Eq. (2.17) and neglect third- and higher order terms in Eq. (2.16) we get:

$$\begin{aligned} F_{ex}[\rho(\mathbf{r})] = F_{ex}[\rho_0] + \mu_{ex}\int d\mathbf{r}\tilde{\rho}(\mathbf{r}) \\ - \frac{k_B T}{2}\int\int d\mathbf{r}d\mathbf{r}'\tilde{\rho}(\mathbf{r})c^{(2)}(\mathbf{r},\mathbf{r}')\tilde{\rho}(\mathbf{r}'). \end{aligned} \tag{2.18}$$

Where $\mu_{ex} = -k_B T c^{(1)}(\infty)$ is the bulk excess chemical potential. As discussed above, the aim of DFT is to calculate the density profile $\rho(\mathbf{r})$. This can be done using the approximation in Eq. (2.18) as long as a suitable expression for $c^{(2)}(\mathbf{r},\mathbf{r}')$

is supplied. This can be done by connecting with integral equation theory for the liquid state structure which is explained in the following section. We also consider a second approximation for the free energy for which the methodology is outlined in [2]. The functional derivative of the free energy with respect to the pair potential $v(r)$ yields [2]

$$\frac{\delta F[\rho]}{\delta v(\mathbf{r},\mathbf{r}')} = \frac{1}{2}\rho^{(2)}(\mathbf{r},\mathbf{r}'), \tag{2.19}$$

where $\rho^{(2)}(\mathbf{r},\mathbf{r}')$ is the inhomogeneous fluid two-body density distribution function. Suppose we now split the pair potential as follows into two parts:

$$v_\alpha(r) = v_1(r) + \alpha v_2(r), \tag{2.20}$$

where the parameter $0 \leq \alpha \leq 1$ is used to 'turn on' the second part of the pair potential. When $\alpha = 1$, Eq. (2.20) gives the full potential i.e. $v_{\alpha=1}(r) = v(r)$. If we then consider the reference fluid with the same temperature and density profile $\rho(\mathbf{r})$, we can then integrate Eq (2.8) to obtain:

$$F[\rho] = F_r[\rho] + \frac{1}{2}\int_0^1 d\alpha \int d\mathbf{r} \int d\mathbf{r}'\rho^{(2)}(\mathbf{r},\mathbf{r}')v_2(\mathbf{r},\mathbf{r}'), \tag{2.21}$$

where $F_r[\rho]$ is the intrinsic free energy of the reference fluid, in which the potential between the particles is $v_1(r)$. The exact expression in Eq. (2.21) can be approximated as:

$$F[\rho] \approx F_r[\rho] + \frac{1}{2}\int d\mathbf{r} \int d\mathbf{r}'\rho(\mathbf{r})\rho(\mathbf{r}')v(\mathbf{r}-\mathbf{r}'). \tag{2.22}$$

This can be justified recalling that we can express the two body density distribution via

$$\rho^{(2)}(\mathbf{r},\mathbf{r}') = \rho(\mathbf{r})\rho(\mathbf{r}')g(\mathbf{r},\mathbf{r}') \tag{2.23}$$

where $g(\mathbf{r}, \mathbf{r}')$ is the inhomogeneous fluid pair distribution function. Assuming $g(\mathbf{r}, \mathbf{r}') = 1$ we can approximate the two body density with $\rho^{(2)}(\mathbf{r}, \mathbf{r}') \approx \rho(\mathbf{r})\rho(\mathbf{r}')$. This approximation is true for $|\mathbf{r}-\mathbf{r}'| \to \infty$, but not necessarily so for small $|\mathbf{r}-\mathbf{r}'|$. The usual approach is to select $v_1(r)$ to be the pair-potential of a well understood model fluid; for example hard spheres. Given the soft-core nature of the potential $v(r)$ that we study here, that is clearly inappropriate. Here, we use the ideal gas as a reference system, i.e. we set $v_1(r) = 0$, so that $v_2(r) = v(r)$. Eq. (2.22) then gives:

$$F_{ex}[\rho] \approx \frac{1}{2} \int dr \int dr' \rho(\mathbf{r})\rho(\mathbf{r}')v(|\mathbf{r} - \mathbf{r}'|) \tag{2.24}$$

We refer to this as the RPA-DFT approximation since this is the functional that generates the random phase approximation (RPA) for the direct pair correlation function, [1, 2, 3]:

$$c^{(2)}(\mathbf{r}, \mathbf{r}') = -\beta \frac{\delta^2 F_{ex}}{\delta\rho(\mathbf{r})\rho(\mathbf{r}')} = -\beta v(|\mathbf{r} - \mathbf{r}'|). \tag{2.25}$$

2.3 The Ornstein-Zernike equation

In matter, the structure of particles i.e how they are arranged is connected to the physical state, whether that be solid, liquid or vapour. The particles in a solid usually have long ranged structural order i.e. a unit lattice structure that is repeated throughout the crystalline region. Liquid molecules have some short range ordering with the correlations between the particles decreasing as the distance increases. A vapour has almost no order at all and the particles can be anywhere (except overlapping if they have strongly repelling cores). The degree of ordering in a fluid is characterised by two-point correlation functions [3]. One of the most important is the radial distribution function $g(r)$. The radial distribution function is calculated (in 2D) by counting the number of particles lying within concentric discs of increasing radius r centred on one particle. These results are then binned in a histogram and normalised relative to the overall bulk density, ρ_0, as illustrated in Fig.2.3. If we consider the radial distribution in 2D as shown in Fig. 2.3 then any molecules within the area between the two red circles is part of the distribution of molecules at distance r away from the reference molecule. $g(r)$ is

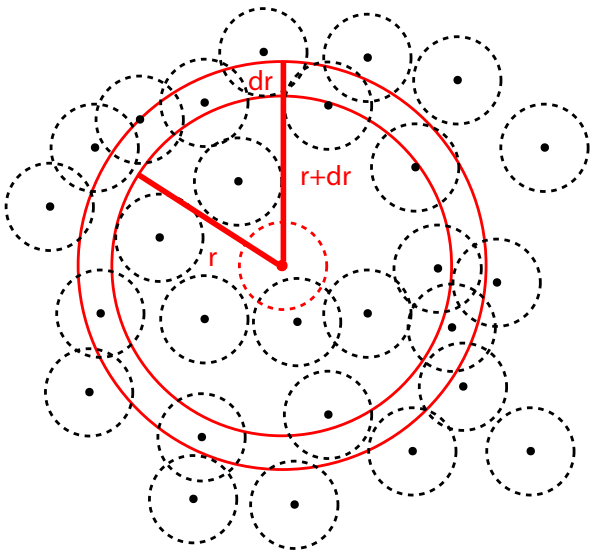

FIGURE 2.2: Sketch of the construction used to define the radial distribution function $g(r)$.

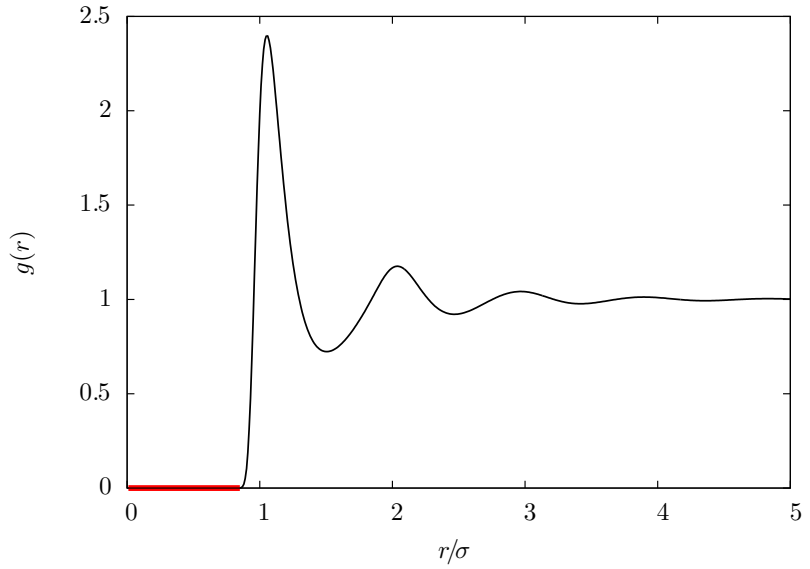

FIGURE 2.3: An example of the radial distribution function for a fluid of LJ particles, where $\beta\epsilon = 0.5$ and $\rho_0\sigma^3 = 0.8$.

defined (in 2D) so that $2\pi r\rho_0 g(r)dr$ is the average number of particles in the area $2\pi r dr$ a distance r from the particle at the centre. If the particles are uncorrelated (i.e. an ideal gas) then $g(r) = 1\ \forall r$. It is possible to measure $g(r)$ in experiments [3]. Some nice microscopy experiments, in which $g(r)$ was measured for colloidal (hard core) particles in a 2D environment were done in Ref. [24]. On the other hand, in a dense liquid, $g(r)$ can be highly structured, exhibiting oscillations - see for example the $g(r)$ displayed in Fig 2.3 for a Lennard-Jones (LJ) fluid.

One can calculate the radial distribution function via the Ornstien-Zernike equation [3]:

$$h(r) = c^{(2)}(r) + \rho_0 \int d\mathbf{r}' c^{(2)}(|\mathbf{r} - \mathbf{r}'|)h(|\mathbf{r}'|), \tag{2.26}$$

where $h(r) = g(r) - 1$ is the total correlation function. Defining the total correlation in this way splits the correlations within the fluid into a direct part given by $c^{(2)}(r)$, which describes the 'direct' correlations between pairs of particles that occur over a distance comparable to that of the interaction range in the pair potential, and the 'indirect' correlations, that are mediated by intermediary other

particles in the fluid. The contribution to $h(r)$ from these is described by the convolution integral [25]. Note that in fluids as $r \to \infty$, $g(r) \to 1$ i.e. as we consider particles further and further away from the reference particle the particles are less likely to be correlated. In this thesis, we calculate $g(r)$ using the so called 'test-particle' method of Percus [26] described below in Sec. 2.5. Once the radial distribution function is known, in addition to the advantages mentioned above we can use it to calculate thermodynamic quantities. For example, the isothermal compressibility χ_T can be found using a relation between the radial distribution function and the static structure factor:

$$S(k) = 1 + \rho_0 \int (g(r) - 1) e^{-i\mathbf{k}\cdot\mathbf{r}} d\mathbf{k}. \tag{2.27}$$

If we consider the Ornstein-Zernike equation in Fourier space:

$$\hat{h}(k) = \hat{c}(k) + \rho_0 \hat{c}(k)\hat{h}(k) \tag{2.28}$$

where $\hat{}$ denotes the Fourier transform and where the Fourier transform of a function $\hat{f}(q)$ is defined as:

$$\hat{f}(q) = \int d\mathbf{r} e^{i\mathbf{q}\cdot\mathbf{r}} f(r). \tag{2.29}$$

The inverse of the Fourier transform is then:

$$f(r) = \left(\frac{1}{2\pi}\right)^d \int d\mathbf{q} e^{i\mathbf{q}\cdot\mathbf{r}} \hat{f}(q). \tag{2.30}$$

Rearranging Eq. (2.28) we are able to get an expression for the Fourier transform of the two body direct correlation function:

$$\hat{c}(k) = \frac{\hat{h}(k)}{1 + \rho_0 \hat{h}(k)}. \tag{2.31}$$

In principle, the total correlation function can be obtained experimentally or numerically from molecular dynamics or Mote Carlo simulations. This, together

with the expression above is one way to obtain $c^{(2)}(r)$. However, another approach is to consider the closure relation [3]:

$$c^{(2)}(r) = -\beta v(r) + h(r) - \ln(h(r) + 1) + b(r), \tag{2.32}$$

where $b(r)$ is the bridge function. This closure relation is formally the exact solution to the Ornstein-Zernike equation. However the bridge function $b(r)$ is unknown for most systems. Nonetheless, there are many approximations for this quantity [3]. We will focus on two such approximations. The first is the Hyper-Netted Chain approximation (HNC):

$$c^{(2)}_{HNC}(r) = -\beta v(r) + h(r) - \ln(h(r) + 1), \tag{2.33}$$

which consists of setting $b(r) = 0$ and the Random Phase Approximation (RPA):

$$c^{(2)}_{RPA}(r) = -\beta v(r) \tag{2.34}$$

Which is accurate when $h(r)$ is small, since then $\ln(1 + h(r)) \approx h(r)$. The RPA is known to provide a good approximation for the fluid structure and thermodynamics for soft core particles i.e when the effective interactions between molecules is finite for all values of r and when interactions are not too strong and the density is sufficiently high [7].

2.4 Test particle method to calculate $g(r)$

Introduced by Percus [26] this method of calculating $g(r)$ for a fluid consists of fixing one particle within the fluid and then calculating the density profile $\rho(r)$ around this particle. The radial distribution function is then:

$$g(r) = \frac{\rho(r)}{\rho_0}. \tag{2.35}$$

The required density profile is that which minimises the grand free energy i.e. the profile satisfies the Euler-Lagrange equation (section section 2.2):

$$\frac{\delta\Omega[\rho(\mathbf{r})]}{\delta\rho(\mathbf{r})} = 0. \tag{2.36}$$

Using Eq. (2.9) and the RPA DFT approximation Eq. (2.24) we get:

$$k_B T \ln[\Lambda^2\rho(\mathbf{r})] + \frac{1}{2}\int d\mathbf{r}' v(|\mathbf{r}-\mathbf{r}'|)\rho(\mathbf{r}') + v(\mathbf{r}) - \mu = 0, \tag{2.37}$$

where, within the test particle method, we consider the external potential to be the pair potential, i.e. $V_{ext}(\mathbf{r}) = v(r)$. In this case as $r \to \infty$, $V_{ext}(\mathbf{r}) = v(r) \to 0$ and $\rho(\mathbf{r}) \to \rho_b$, so Eq. (2.37) becomes for $r \to \infty$:

$$k_B T \ln[\Lambda^2\rho_b] + \frac{1}{2}\rho_b \int d\mathbf{r}' v(|\mathbf{r}-\mathbf{r}'|) - \mu = 0. \tag{2.38}$$

Rearranging for μ and substituting back into Eq. (2.37) we get:

$$k_B T \ln\left[\frac{\rho(r)}{\rho_b}\right] + \int d\mathbf{r}'(\rho(\mathbf{r}') - \rho_b)v(|\mathbf{r}-\mathbf{r}'|) + v(\mathbf{r}) = 0 \tag{2.39}$$

which we then rearrange for $\rho(r)$:

$$\rho(r) = \rho_b e^{-\int d\mathbf{r}'(\rho(\mathbf{r}')-\rho_b)\beta v(|\mathbf{r}-\mathbf{r}'|)-\beta v(\mathbf{r})} \tag{2.40}$$

This equation can then be solved via Picard iteration. Using this test particle method and the above equation, we are able to obtain a good deal of information about the structure of a fluid around this particle. Using Eq. (2.40) to calculate the density profile about the test particle, we can calculate the radial distribution function $g(r)$ via Eq. (2.35).

2.5 RPA DFT and HNC for the GEM-4 fluid

In this section we compare the accuracy of the RPA DFT and the HNC approximations for $g(r)$ for the GEM-4 model. We use the 'test-particle' method of Section 2.4 to calculate the radial distribution function $g(r)$ which is displayed in Fig. 2.4. The density profile of the fluid phase is calculated by solving the Euler-Lagrange equation via a simple iterative algorithm on a 2D discretised grid with periodic boundary conditions and then $g(r)$ is obtained via Eq (2.35). The HNC approximation, which comes from setting the bridge function in the closure to the OZ equation Eq. (2.32) to zero, is in principle more accurate than the simpler RPA DFT approximation, which loses accuracy at low density [7]. Results from the HNC are also displayed in Fig. 2.4. The radial distribution function $g(r)$ is calculated at three state points, of decreasing bulk density from top to bottom $(\beta\epsilon, \rho^b R^2) = (1, 0.36)$, $(5, 0.14)$ and $(10, 0.088)$. We can see that at the higher density there is very good agreement between the two approximations, at lower density however, there is some disagreement as we expected, but nonetheless is surprisingly good. Note that for the two higher density state points that $g(r = 0) \neq 0$, indicating there is some overlap of these soft particles. This is also due to the fact that these are for lower $\beta\epsilon$, or equivalently for higher temperatures.

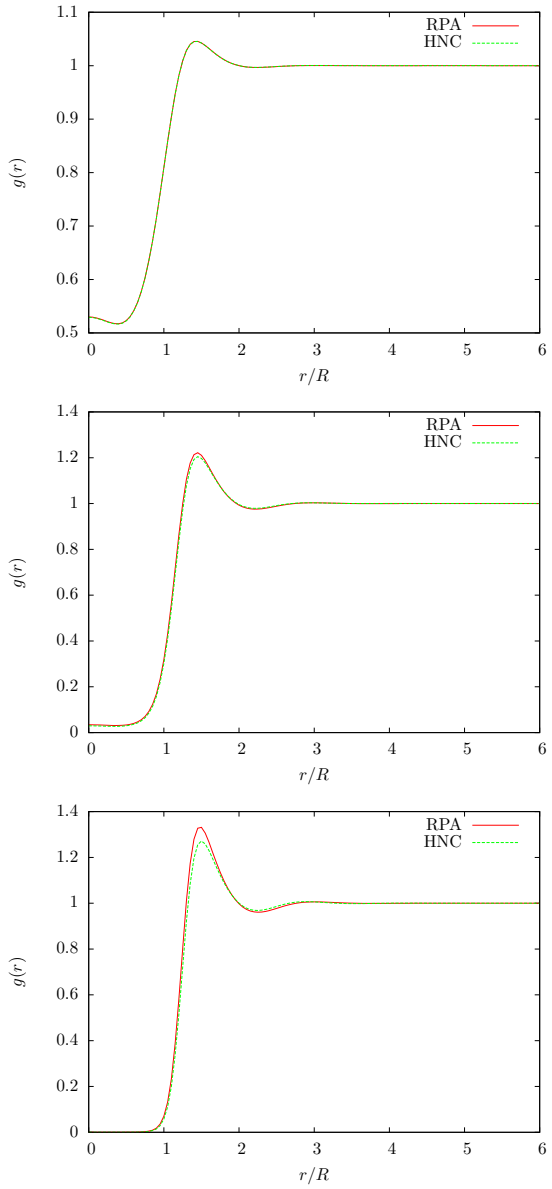

FIGURE 2.4: The radial distribution function $g(r)$ for a GEM-4 fluid with bulk chemical potential $\mu = 0$ obtained from the HNC closure to the OZ equation (dashed lines) and from the RPA DFT via the test particle method (solid lines), for several values of $\beta\epsilon$. The results correspond to the state points (top to bottom) $(\beta\epsilon, \rho^b R^2) = (1, 0.36)$, $(5, 0.14)$ and $(10, 0.088)$. As $\beta\epsilon$ increases, the RPA approximation becomes less good; nevertheless, even for these fairly low density state points and with repulsion strength such as such as $\beta\epsilon = 10$ the agreement is surprisingly good – recall that the RPA approximation improves as the density is increased.

2.6 Phase Coexistance

In the previous sections we have focused on the theory and structure of liquids. In this section we now consider the conditions for coexistence between two phases, namely the liquid and solid phases. Coexistence between a liquid and solid phase occurs when the temperature T, pressure p and chemical potential μ of both phases are equal, and of course, when both density profiles minimise the Euler-Lagrange equation. If we let ρ_l be the density of the liquid and $\rho_x(\mathbf{r})$ be the density of the solid crystalline phase then coexistence can occur when the following conditions are met:

$$T_l = T_x \qquad \mu_l = \mu_x \qquad p_l = p_x, \tag{2.41}$$

where subscript l and x denote the properties of the liquid and crystal phases respectively. This last condition is equivalent to $\Omega[\rho_0] = \Omega[\rho_x(\mathbf{r})]$, where:

$$\left.\frac{\delta\Omega[\rho(\mathbf{r})]}{\delta\rho(\mathbf{r})}\right|_{\rho(\mathbf{r})=\rho_l} = 0 \qquad \left.\frac{\delta\Omega[\rho(\mathbf{r})]}{\delta\rho(\mathbf{r})}\right|_{\rho(\mathbf{r})=\rho_x(\mathbf{r})} = 0. \tag{2.42}$$

An example of coexistence between the solid and liquid phases can be seen in Fig. 2.5. On the left are the density peaks which correspond the crystal structure and on the right is the flat uniform density of the liquid. The structure of these density peaks is important to the properties of the crystal. Note that in Fig. 2.5 the crystal structure does not advance into the liquid and visa versa for the liquid. The interface between the crystal and liquid is sometimes called a front. If it were advancing into the liquid we would consider it a solidification front. We will discuss such fronts in further detail later in this thesis. In Fig. 2.6 we show the phase diagram for the GEM-4 and GEM-8 models (see also [27]) where we have calculated the binodals and spinodals for both systems. The binodals show the average densities of the coexisting liquid and solid phases, the solid being the higher density phase. The spinodals indicate the density value where the

uniform liquid becomes linearly unstable which is discussed in the next chapter. The binodals are calculated using the approximation in Eq. (2.24), which we use to calculate the grand potential for each phase. From this we can then locate where the grand free energies for both the liquid and solid phases are the same. The bulk phase diagrams displayed in Fig 2.6 exhibit a liquid phase at low densities and/or high temperatures which freezes to form a novel cluster crystal phase as the temperature decreases or the density increases. The density profile for the crystal phase is calculated in much the same way as the test particle liquid density profiles discussed in the previous section. An initial guess for the density profile containing density peaks is taken by the model, Picard iteration is then applied to find the density profile that satisfies the Euler-Lagrange equation. In the one component models with pair potentials GEM-4 and GEM-8 we see long range ordering of the peaks throughout the density profiles. These peaks signify the high density of particles at these locations within the crystal structure. Note that the soft nature of the GEM-n potentials allows for complete overlap of particles and so these density peaks can indicate many particles overlapping each other. If we consider the different equilibrium crystal structures that are obtained by moving throughout the lower right half of the GEM-4 and GEM-8 phase diagram Fig. 2.6 we find that the hexagonal crystal structure frequently minimises the free energy i.e. the density profile which corresponds to an hexagonal crystal structure satisfies the Euler-Lagrange equation.

These results for the GEM-n system are based on the approximate free energy in Eq. (2.24). Our main reason for considering this simple model centres on the fact that the structure and phase behaviour (i.e. thermodynamics) of this model is well described by a rather simple approximation for the excess free energy - that in Eq. (2.24). This approximation has also been widely used elsewhere in studies of the structure and phase behaviour of soft-core systems [28, 7, 29, 30, 31, 32, 33, 34, 35, 36, 37, 38, 39, 40, 41, 42, 43, 44, 45, 46, 47, 48, 49].

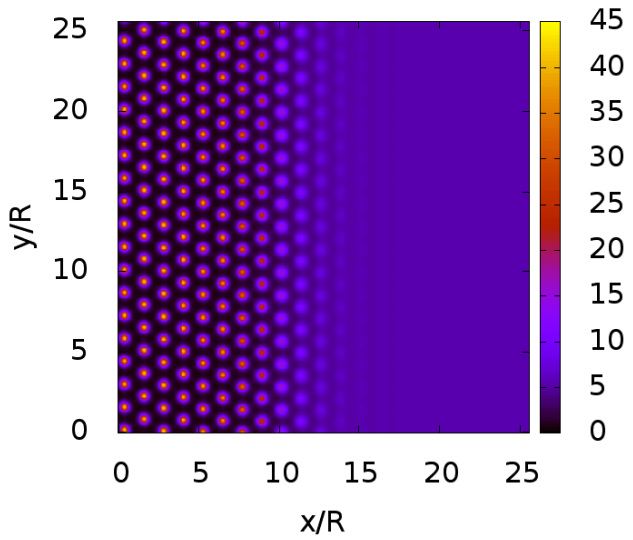

FIGURE 2.5: Density profile at the free interface between the coexisting liquid and solid phases, for $\beta\epsilon = 1$ and $\beta\mu = 17.0$ for the GEM-4 model.

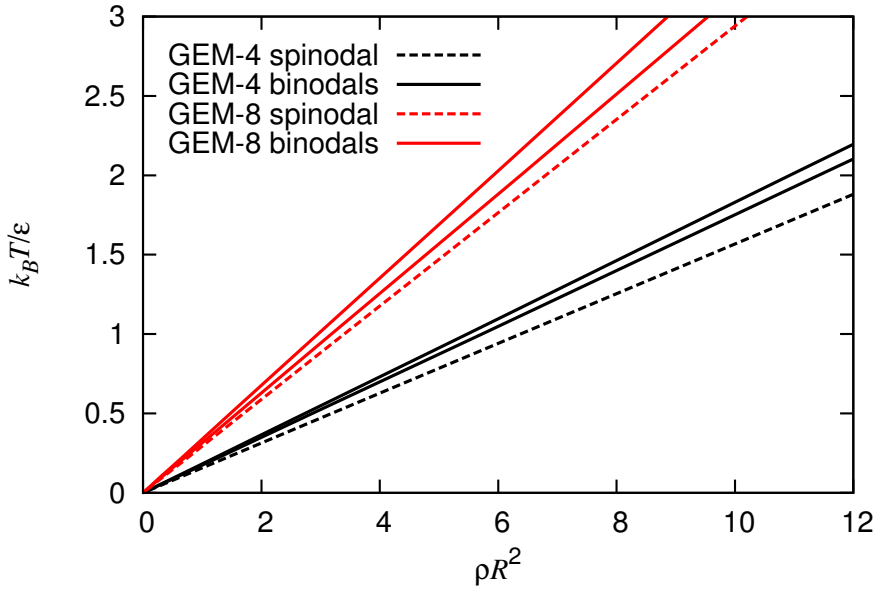

FIGURE 2.6: Phase diagrams of the one component 2D GEM-4 and GEM-8 model fluids. The solid lines are the binodals – i.e., the loci of the coexisting liquid and solid phases. The dashed lines are the spinodal-like instability lines along which the metastable liquid phase becomes linearly unstable.

Chapter 3

Theory for non-equilibrium dynamics

3.1 Dynamical density functional theory

DFT is a useful and successful tool for studying (among many other things) a variety of fluid and solid equilibrium phenomena. To be able to study non-equilibrium situations we need to generalise DFT to study the dynamics. In particular, we assume the soft particles of interest here are Brownian particles with over-damped stochastic equations of motion. The density distribution at time t is $\rho(\mathbf{r}, t)$ and so the time evolution of this density distribution is given by the continuity equation:

$$\frac{\partial \rho}{\partial t} = -\nabla \cdot \mathbf{j}. \tag{3.1}$$

In order to solve this equation we need an expression for the current $\mathbf{j} = \rho\mathbf{u}$, where $\mathbf{u}$ is the local fluid velocity. In general, we only have formal expressions for this quantity, and to actually calculate the fluid dynamics, approximations are required. A reasonable approximation for our model is [50, 51]:

$$\mathbf{j} = -\Gamma\rho\nabla\frac{\delta F[\rho]}{\delta\rho}, \tag{3.2}$$

where $F[\rho]$ is the equilibrium Helmholtz free energy functional, $\Gamma = D/k_BT$ is the mobility coefficient and D is the diffusion coefficient. The result in Eq. (3.2)

was originally derived by Marconi and Tarazona [50]. They presented a new-time dependent "dynamical density functional theory" (DDFT). Starting from the stochastic equations which describe the Brownian motion of N interacting particles they derived a deterministic equation for the ensemble average density $\rho(\mathbf{r},t) = \langle\hat{\rho}(\mathbf{r},t)\rangle$:

$$\begin{aligned}\frac{\partial\rho(\mathbf{r},t)}{\partial t} = \Gamma\nabla\Bigg[\int k_BT\nabla\rho(\mathbf{r},t) + \rho(\mathbf{r},t)\nabla V_{ext}(\mathbf{r}) \\ + \int d\mathbf{r}'\langle\hat{\rho}(\mathbf{r},t)\hat{\rho}(\mathbf{r}',t)\rangle\nabla v(\mathbf{r}-\mathbf{r}')\Bigg],\end{aligned} \tag{3.3}$$

where $\hat{\rho}(\mathbf{r},t) = \sum_{i=1}^{N}\delta(\mathbf{r}-\mathbf{r}_i)$ is the density operator and $\langle\cdot\rangle$ denotes an ensemble average, over all realisations of the stochastic noise [50]. Note that $\langle\hat{\rho}(\mathbf{r},t)\hat{\rho}(\mathbf{r}',t)\rangle = \rho^{(2)}(\mathbf{r},\mathbf{r}',t)$, is the two body density distribution in a system out of equilibrium [50]. Equilibrium density functional theory, which is already a powerful and widely used tool for investigating the equilibrium state of particle systems, can provide an approximation for this quantity. An equilibrium state corresponds to a minimum in the grand potential functional Eq. (2.9). From the general properties of the equilibrium functionals we have the following two exact equilibrium relations between $\rho(\mathbf{r})$ and $V_{ext}(\mathbf{r})$ (external potential): First, the local balance of momentum at any point implies the Born-Bogolubov-Green-Kirkwood-Yvon (BBGKY) relation [50]:

$$\frac{1}{\rho(\mathbf{r})}\nabla\rho(\mathbf{r}) + \beta\nabla V_{ext}(\mathbf{r}) = -\beta\frac{1}{\rho(\mathbf{r})}\int d\mathbf{r}'\rho^{(2)}(\mathbf{r},\mathbf{r}')\nabla v(\mathbf{r}-\mathbf{r}'). \tag{3.4}$$

Second, equilibrium implies that the functional derivative of $F[\rho(\mathbf{r})]$ at any point is equal to the chemical potential μ which is uniform in space. Taking the gradient of Eq. (2.11) gives the equation [50]:

$$\frac{1}{\rho(\mathbf{r})}\nabla\rho(\mathbf{r}) + \beta\nabla V_{ext}(\mathbf{r}) = -\nabla\frac{\delta}{\delta\rho(\mathbf{r})}[\beta F_{ex}[\rho]]. \tag{3.5}$$

Comparing equations (3.4)-(3.5) they were able to express the last term in Eq. (3.4) as:

$$\int d\mathbf{r}' \langle \hat{\rho}(\mathbf{r},t)\hat{\rho}(\mathbf{r}',t)\rangle \nabla v(\mathbf{r}-\mathbf{r}') = \rho(\mathbf{r},t)\nabla \frac{\delta F_{ex}[\rho(\mathbf{r})]}{\delta \rho(\mathbf{r},t)}. \tag{3.6}$$

This is exact for an equilibrium system. Assuming this remain true out of equilibrium is the central approximation made in deriving DDFT. Thus, with Eq. (2.9) and Eq. (3.5) we are able to derive the main result of the dynamical density functional approach, based of the use of the equilibrium functional $F[\rho(\mathbf{r})]$:

$$\frac{\partial \rho(\mathbf{r},t)}{\partial t} = \Gamma \nabla \cdot \left[\rho(\mathbf{r},t) \nabla \frac{\delta F[\rho(\mathbf{r},t)]}{\delta \rho(\mathbf{r},t)} \right]. \tag{3.7}$$

In using Eq. (3.6) to derive the DDFT we have made the approximation that the non-equilibrium fluid two-body correlations are the same as those in the equilibrium fluid with the same one-body density distribution [28]. Note that the equilibrium solutions of Eq. (3.7) are solutions of the equilibrium DFT Eq. (2.9), since at equilibrium $\frac{\partial \rho}{\partial t} = 0$, so Eq. (3.7) gives $\frac{\delta F}{\delta \rho} = constant$. The $constant$ is the chemical potential μ, so equilibria of Eq. (3.7) are solutions to Eq. (2.10) [c.f. (2.11)]. Having Eq. (3.7) we are able to study the non-equilibrium dynamics of the interacting Brownian particles. The dynamical processes that is of particular interest here is to describe what occurs when a super-cooled liquid freezes and how solidification fronts advance. In order to study such fronts we perform a marginal stability calculation in order to gain important information about these fronts, which we will use later within this chapter, but before doing this we must first calculate the dispersion relation.

3.2 Dispersion Relation

In this section we introduce the dispersion relation [52, 53, 28]. This is a quantity that enables us to determine the regions of the phase diagram where the liquid is unstable to periodic density fluctuations occurs where the crystal is the equilibrium state. We begin with the main DDFT Eq (3.7) and the functional derivative of the Helmholtz free energy $F[\rho(\mathbf{r})]$:

$$\frac{\delta F[\rho(\mathbf{r},t)]}{\delta\rho(\mathbf{r},t)} = k_BT\ln(\Lambda^2\rho(\mathbf{r},t)) + \frac{\delta F_{ex}[\rho(\mathbf{r},t)]}{\delta\rho(\mathbf{r},t)} + V_{ext}(\mathbf{r},t) \tag{3.8}$$

where $V_{ext}(\mathbf{r},t)$ is the external potential from a wall or other boundary. If we now take the gradient of Eq. (3.8) we obtain:

$$\nabla\frac{\delta F[\rho(\mathbf{r},t)]}{\delta\rho(\mathbf{r},t)} = \frac{k_BT}{\rho(\mathbf{r},t)}\nabla\rho(\mathbf{r},t) - k_BT\nabla c^{(1)} + \nabla V_{ext}(\mathbf{r},t). \tag{3.9}$$

Note that $c^{(1)} = \frac{\delta F_{ex}[\rho(\mathbf{r},t)]}{\delta\rho(\mathbf{r},t)}$. Rearranging Eq (3.9) we obtain:

$$\beta\rho(\mathbf{r},t)\nabla\frac{\delta F[\rho(\mathbf{r},t)]}{\delta\rho(\mathbf{r},t)} = \nabla\rho(\mathbf{r},t) - \rho(\mathbf{r},t)\nabla c^{(1)} + \rho(\mathbf{r},t)\nabla\beta V_{ext}(\mathbf{r},t). \tag{3.10}$$

Substituting Eq (3.10) into Eq. (3.7) we have:

$$\frac{1}{D}\frac{\partial\rho(\mathbf{r},t)}{\partial t} = \nabla^2\rho(\mathbf{r},t) - \nabla[\rho(\mathbf{r},t)\nabla c^{(1)}] + \nabla[\rho(\mathbf{r},t)\nabla\beta V_{ext}(\mathbf{r},t)] \tag{3.11}$$

where $D = \frac{\Gamma}{\beta}$ is the diffusion coefficient. To study the stability of the uniform liquid we assume we have no contribution from a external potential $V_{ext} = 0$ and we also introduce the notation that $\tilde{\rho} = \rho - \rho_0$ i.e. $\tilde{\rho}$ is the density modulation around a reference density, in this case the bulk fluid density ρ_0. Eq. (3.11) becomes:

$$\begin{aligned}\frac{1}{D}\frac{\partial\rho(\mathbf{r},t)}{\partial t} = \nabla^2\tilde{\rho}(\mathbf{r},t) - \nabla\Big[&(\tilde{\rho}(\mathbf{r},t)+\rho_0)\nabla[c^{(1)}[\rho_0] \\ &+ \int d\mathbf{r}'\tilde{\rho}(\mathbf{r}',t)\frac{\delta c^{(1)}(\mathbf{r}-\mathbf{r}')}{\delta\rho} + ...]\Big]\end{aligned} \tag{3.12}$$

where we have made a functional Taylor expansion of the term involving $c^{(1)}$. Recalling that $c^{(2)}(\mathbf{r},\mathbf{r}') = \frac{\delta c^{(1)}}{\delta \rho}$ is the pair direct correlation function from the Ornstien-Zernike equation. Hence we have:

$$\frac{1}{D}\frac{\partial \rho(\mathbf{r},t)}{\partial t} = \nabla^2\tilde{\rho}(\mathbf{r},t) - \nabla\left[(\tilde{\rho}(\mathbf{r},t)+\rho_0)\nabla\int d\mathbf{r}'\tilde{\rho}(\mathbf{r}',t)c^{(2)}(\mathbf{r}-\mathbf{r}') + ...\right] \tag{3.13}$$

consolidating powers of $\tilde{\rho}(\mathbf{r},t)$ we have:

$$\frac{1}{D}\frac{\partial \rho(\mathbf{r},t)}{\partial t} = \nabla^2\tilde{\rho}(\mathbf{r},t) - \rho_0\nabla^2\int d\mathbf{r}'\tilde{\rho}(\mathbf{r}',t)c^{(2)}(|\mathbf{r}-\mathbf{r}'|) + \mathcal{O}(\tilde{\rho}^2). \tag{3.14}$$

We now consider $\tilde{\rho}$ to be a sum of Fourier modes,

$$\tilde{\rho}(\mathbf{r},t) = \sum_{\mathbf{k}}\tilde{\rho}_{\mathbf{k}}e^{i\mathbf{k}\cdot\mathbf{r}+\omega(k)t}, \tag{3.15}$$

where $k = |\mathbf{k}|$. Substituting Eq. (3.15) into the parts of Eq. (3.14) that are linear in $\tilde{\rho}$ and noting that:

$$\int d\mathbf{r}'e^{i\mathbf{k}\cdot\mathbf{r}'}c^{(2)}(|\mathbf{r}-\mathbf{r}'|) = e^{i\mathbf{k}\cdot\mathbf{r}}\int d\mathbf{r}'e^{i\mathbf{k}\cdot(\mathbf{r}'-\mathbf{r})}c^{(2)}(|\mathbf{r}-\mathbf{r}'|) = e^{i\mathbf{k}\cdot\mathbf{r}}\hat{c}(k), \tag{3.16}$$

where $\hat{c}(k)$ denotes the Fourier transform of $c^{(2)}(r)$, and then dividing through by $\tilde{\rho}$ leads us to the dispersion relation for the growth rate $\omega(k)$ of density fluctuations with wavenumber k, namely:

$$\omega(k) = -Dk^2[1-\rho_0\hat{c}(k)]. \tag{3.17}$$

3.3 Stability of the GEM-n fluid

Wether or not the uniform fluid is linearly stable is completely dependent upon the dispersion relation Eq. (3.17). If we consider the density modes in Eq. (3.15), it is clear that if the dispersion relation $\omega(k)$ is negative for all values of k, then all small amplitude density perturbations will decrease in amplitude and the density profile of the liquid will remain flat i.e. the liquid is in a linearly stable state. If there are some values of k for which $\omega(k)$ is positive, then all density fluctuations corresponding to these k modes will grow which can lead to solidification fronts and to freezing i.e. the liquid is in a linearly unstable state. Note that we have not addressed any situation where the solidification process starts via non-linear means (i.e. large amplitude density perturbations), this scenario will be explained in a later section. In Fig. 3.1 we see an example of the coexistence (binodal) lines and also the linear stability threshold for the GEM-8 model. The dashed line in Fig. 3.1 is the spinodal-like instability line at which the linearly stable liquid become linearly unstable on moving to the right of this line. The inset plot in the top left of Fig. 3.1 is an example of the dispersion relation for the upper half region, where the liquid is linearly stable. Note that in this region of the phase diagram the dispersion relation $\omega(k) < 0$ for all k. The inset plot in the lower right of Fig. 3.1 is an example of the dispersion relation for the lower half region, where the liquid is linearly unstable. Here, the dispersion relation $\omega(k) > 0$ for some k. There is also the possibility that the liquid and crystalline phases are both linearly stable states at the same time. When they have the same pressure, temperature and chemical potiential, then as discussed in Sec 2.6 they are in phase coexistence. The solid lines in the phase diagram Fig. 3.1 are the binodals and indicate such a region of coexistence between the liquid and solid phases.

Within the present mean-field approximation Eq (2.24), the pair direct correlation function is given by Eq (2.25) and so the dispersion relation Eq (3.17) has the

following, very simple form:

$$\omega(k) = -Dk^2[1 + \rho_0\beta\hat{v}(k)], \tag{3.18}$$

where $\hat{v}(k)$ is the 2D Fourier transform of the pair potential $v(r)$. The threshold for linear instability of the uniform fluid is determined by $\omega(k = q) = 0$, where $q \neq 0$ is the wavevector at which $\omega(k)$ has a maximum, i.e., by $1 + \rho_0\beta\hat{v}(q) = 0$. This leads to a very simple linear density dependence of the onset temperature: $k_BT = |\hat{v}(k = q)|\rho_0$, where the marginally stable wavenumber q at onset is determined by the condition

$$\left.\frac{d\hat{v}(k)}{dk}\right|_{k=q} = 0. \tag{3.19}$$

For the 2D GEM-8 system the onset wavenumber $q \approx 5.26/R$. Since $\hat{v}(k = q) \approx -0.294\epsilon R^2$ is independent of the density, the linear instability threshold is a straight line in the phase diagram:

$$\frac{k_BT}{\epsilon} \approx 0.294\rho_0R^2. \tag{3.20}$$

This can also be seen in Fig. 2.6. In addition, the binodals along which the liquid and crystal phases coexist in thermodynamic equilibrium also appear to be straight lines in the phase diagram. This is not obvious because the binodal calculation requires that one first obtains the crystal density profile, which is a highly nonlinear problem. However, fitting the numerically obtained binodals with a straight line proves to be an excellent approximation (Fig. 2.6). For example, for the GEM-8 fluid we find that the binodal for the crystal state at coexistence is given by $k_BT/\epsilon \approx 0.314\rho_0R^2$ and that of the liquid is $k_BT/\epsilon \approx 0.339\rho_0R^2$. Thus, when the temperature $k_BT/\epsilon = 1$, the density of the liquid at coexistence is $\rho_0R^2 \approx 1/0.339 = 2.95$ while that of the crystal is $\rho_0R^2 \approx 1/0.314 = 3.18$.

Having discussed above the linear stability and coexistence of a system, we now consider how an unstable liquid state transforms into the solid state. In particular, we are interested in the situation where the stable solid phase invades the

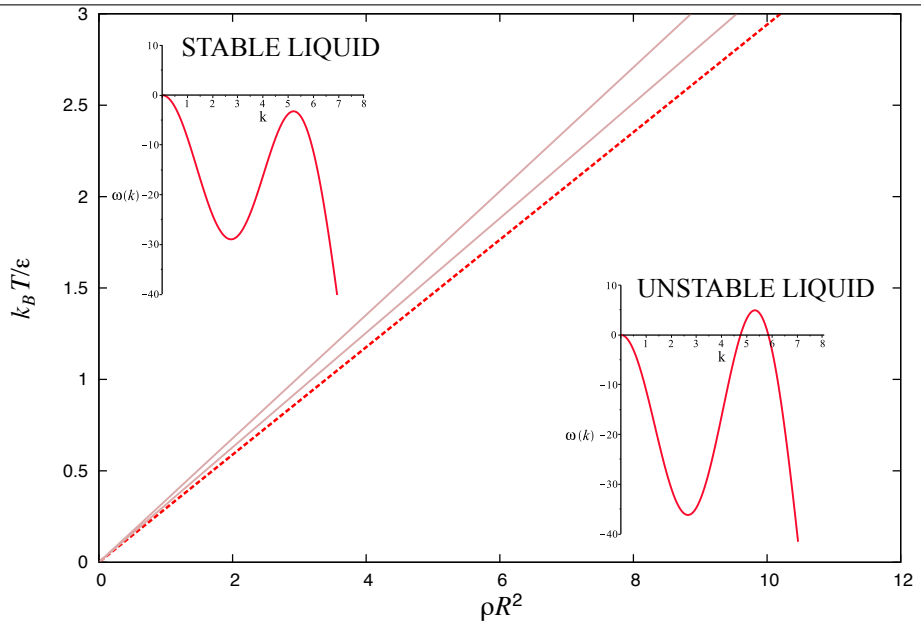

FIGURE 3.1: Linear instability line (dotted) for GEM-8 and typical dispersion relations shown either side.

unstable liquid. Between the two phases is a solidification front that advances. We study in detail the properties of these solidification fronts here and in later sections. Solidification fronts occur when a liquid has been rapidly chilled. This can induce a solidification front to move throughout the liquid leaving a crystal/solid structure behind. Fig. 6 shows an advancing solidification front for the GEM-4 model. The front is initiated by adding a small random value to the otherwise uniform density profile along the line $x/R = 25.6$. This creates a pair of fronts that then advances through the bulk fluid density profile creating density peaks in their wake which corresponds to the crystal structure of the now frozen liquid. The fronts can contain two distinct parts; one being the high density peaks and the other the 'stripes' where the density profile shows oscillation parallel to the front.

The density profile in a crystalline phase is a collection of density peaks which correspond to the location of the now frozen molecules. On the bottom right of Fig. 3.2 we see an example of a density profile for a one-component fluid which has been rapidly cooled (quenched). The yellow dots indicate density peaks and

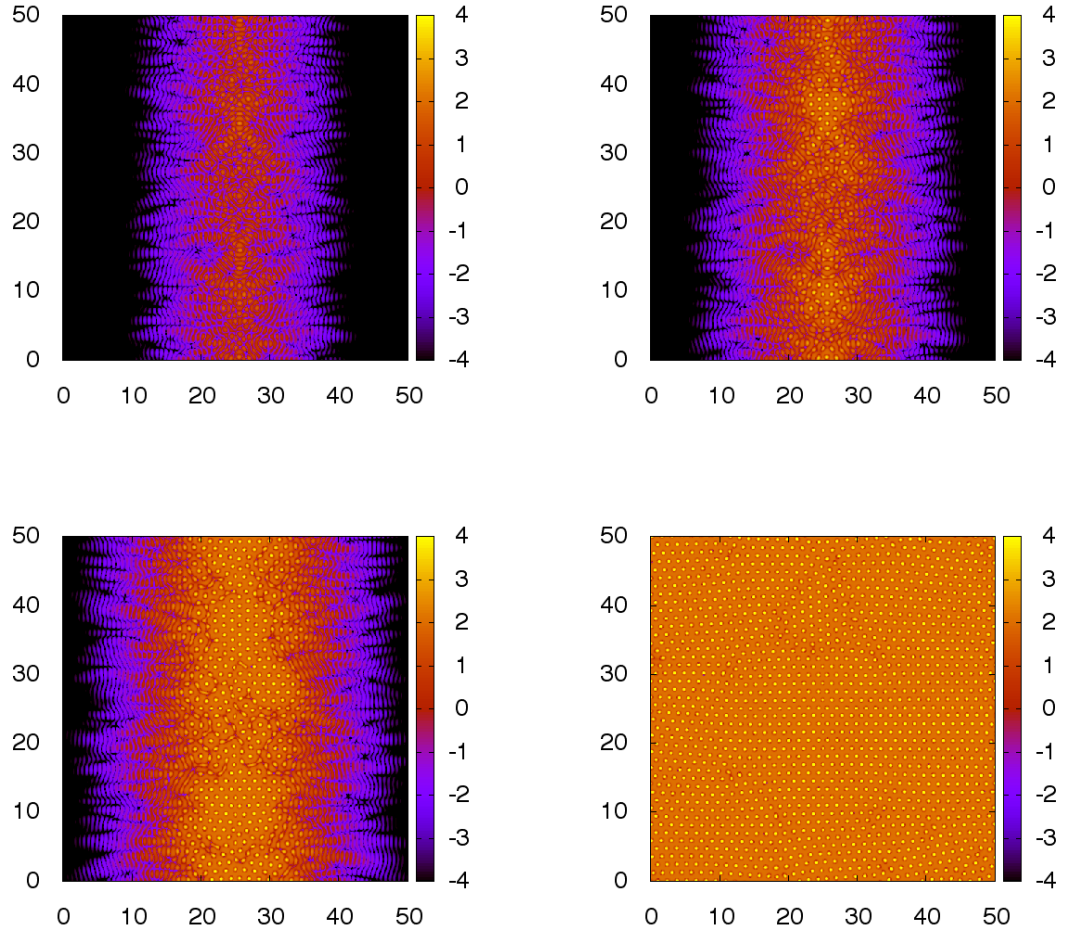

FIGURE 3.2: Solidification fronts moving through an unstable liquid $t^* = 1.0$ (top left), $t^* = 1.2$ (top right), $t^* = 1.4$ (bottom left) and $t^* = 4.8$ (bottom right). Note the above figures show the logarithm of the density profiles ($\ln|\rho(\mathbf{r})|$).

the darker regions showing lower density levels. It is desirable to study the defects that are apparent in the structures formed. We now introduce two methods we use throughout this thesis to analyse crystal structures and quantify the degree of disorder: Delaunay triangulation and Voronoi diagrams - see Fig. 3.3. We first identify the locations of all the density maxima above a certain threshold value, which give us discrete points within the density profile. A Delaunay triangulation is then done by connecting all nearest neighbouring peaks, the result can be seen on the bottom left in Fig. 3.4 which shows a Delaunay triangulation which has been done on the density profile on the left. Using this method can be useful in identifying defect regions within the crystal structure. This statement

can also hold true for the Voronoi Diagram seen of the bottom right of Fig. 3.4. Both the Delaunay and Voronoi diagrams mentioned above are done on the same set of density profile maxima. We now explain in more detail how Delaunay and Voronoi diagrams are created. All of the density peaks in a profile are considered to be points on a 2D plane. For the Delaunay triangulation we connect all of these points to their nearest neighbours, an example sketch of this is in Fig. 3.3 (left). Note that none of the other points is allowed within a triangle and that in a Delaunay triangulation, the minimum angles of all the triangles, is maximised. Once a Delaunay triangulation has been done on a profile, it can be used to create a Voronoi diagram. We start by drawing a perpendicular line through the mid point of every line in the Delaunay triangulation. Comparing Fig 3.3 we notice that if we were to place each of the sketches on top of one another, every line in the left sketch would have an intersecting line through its mid point. These methods created the diagrams we see at the bottom of Fig 3.4. There are several advantages that come from using multiple methods of studying the same crystal structure. If we consider the diagrams at the bottom of Fig 3.4 we can clearly see that that the larger defects in the profile are more easily spotted in the Delaunay triangulation (bottom left) whereas the Voronoi diagram (bottom right) can be used more easily to see defects on a small scale. From the Delaunay triangulation, we have also the angles of the corners in all of the triangles. Putting these in a histogram gives a very illuminating quantity. For example, for the perfect structure in Fig 3.3 the Histogram has a single sharp peak at 60°. However for structures having disorder the peak becomes broader. If there are other structures, the peaks appear at different angles.

In this section we have introduced DDFT and shown how it can be used to study the linear stability of the liquid phase via a dispersion relation. We derived this dispersion relation and used it to study the linear stability for the GEM-n model. Using the dispersion relation we show how to generate stability and coexistance conditions in the form of wavenumber q for the GEM-8 model. We have also considered a particular case of instability which results in a solidification

front and a crystalline structure, and discussed different methods of analysing this structure. Before analysing GEM-n systems in detail we consider a simplified model, from which much insight can be gained.

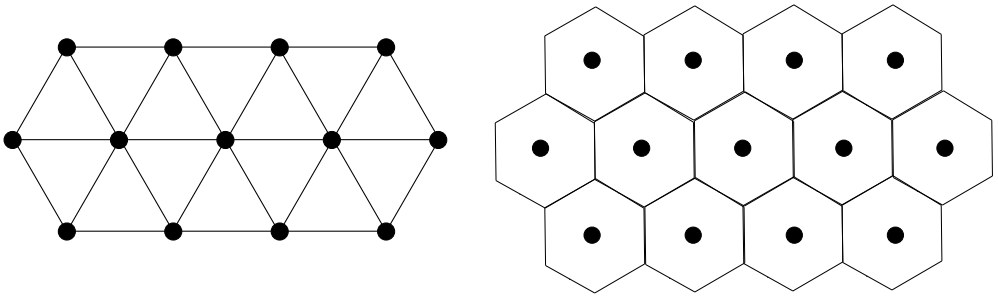

FIGURE 3.3: Sketches to show Delaunay triangulation (left) and Voronoi (right) diagrams. Note the same density peak structure (black dots), but different structure of lines.

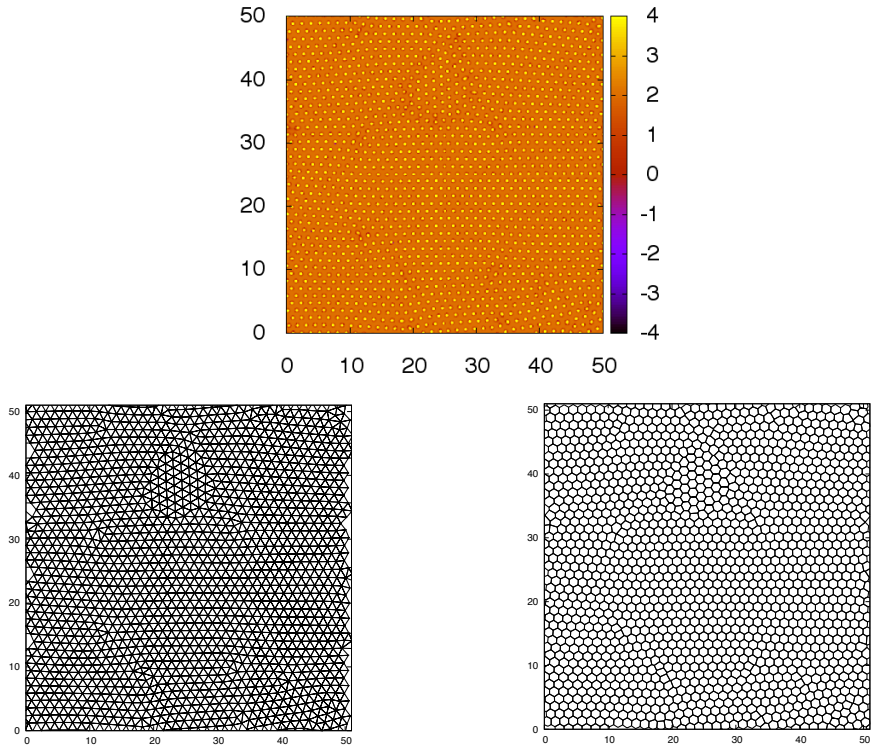

FIGURE 3.4: Example of a density profile for a one-component fluid which has be rapidly frozen (top). The bottom two diagrams are a Delaunay triangulation (bottom left) and a Voronoi diagram (bottom right) both done on the density profile (top).

Chapter 4

Solidification fronts and a minimal model

4.1 Phase field crystal: a minimal model for freezing

Phase field crystal (PFC) models were first introduced [54, 55, 56] as a minimal DFT-like model capable of describing the freezing transition. The main difference between the PFC and regular phase-field models being that microscopic details are included in the model by including periodic ground state solutions. We describe this model and discuss its linear stability and solidification fronts in order to gain insight from this simple model for the more complex GEM-n model of interest later in this thesis.

In the following derivation we follow closely the arguments laid out in [57]. The governing equations of the PFC model are formulated from DDFT by performing a gradient expansion of the approximation for the excess free energy F_{ex} in Eq. (2.18) and expanding the free energy in powers of a order parameter (i.e. a scaled density) ϕ. In order to derive the PFC free energy we first need an approximation for the two body direct correlation function $c^{(2)}(\mathbf{r}, \mathbf{r}')$ which we obtain by considering a gradient expansion truncated at the forth order term:

$$c^{(2)}(\mathbf{r}, \mathbf{r}') \approx -\beta(\hat{A}_0(\rho(\mathbf{r})) + \hat{A}_2\nabla^2 + \hat{A}_4\nabla^4)\delta(\mathbf{r} - \mathbf{r}'). \tag{4.1}$$

Although in principle all the coefficients $\hat{A}_i$ are functions of $\rho(\mathbf{r})$, we assume that

the coefficients $\hat{A}_2$ and $\hat{A}_4$ are constants [58]. Substituting this approximation for the two body direct correlation function into the expression for the excess free energy Eq. (2.18), we get:

$$\begin{aligned} F_{ex}[\rho(\mathbf{r})] = F_{ex}[\rho_0] + \mu_{ex} \int d\mathbf{r}\tilde{\rho}(\mathbf{r}) \\ + \frac{1}{2}\int\int d\mathbf{r}d\mathbf{r}'\tilde{\rho}(\mathbf{r})\left[(\hat{A}_0(\rho(\mathbf{r})) + \hat{A}_2\nabla^2 + \hat{A}_4\nabla^4)\delta(\mathbf{r}-\mathbf{r}')\right]\tilde{\rho}(\mathbf{r}'). \end{aligned} \tag{4.2}$$

Recall that $\tilde{\rho} = \rho(\mathbf{r}) - \rho_0$. This expression for the excess free energy can be combined with the ideal-gas term to write the total intrinsic Helmholtz free energy as:

$$F[\rho(\mathbf{r})] = \int d\mathbf{r}\left[f_0[\rho(\mathbf{r})] + \frac{1}{2}\tilde{\rho}(\mathbf{r})(\hat{A}_2\nabla^2 + \hat{A}_4\nabla^4)\tilde{\rho}(\mathbf{r})\right] \tag{4.3}$$

where

$$f_0(\rho(\mathbf{r})) = k_BT\rho(\mathbf{r})(\ln(\rho(\mathbf{r})) - 1) + f_{ex}[\rho_0] + \mu_{ex}\tilde{\rho}(\mathbf{r}) + \frac{1}{2}\tilde{\rho}(\mathbf{r})\hat{A}_0(\rho(\mathbf{r})). \tag{4.4}$$

The first term is the ideal gas contribution. We now make a further approximation by Taylor expanding the function $f_0(\rho)$ about the bulk density ρ_0, giving:

$$f_0(\rho(\mathbf{r})) \approx f_0(\rho_0) + f_0'(\rho_0)\tilde{\rho}(\mathbf{r}) + \frac{f_0''(\rho_0)}{2}\tilde{\rho}(\mathbf{r})^2 + \frac{f_0^{(4)}(\rho_0)}{4!}\tilde{\rho}(\mathbf{r})^4. \tag{4.5}$$

Note that in the Taylor expansion above we have chosen the reference density ρ_0 such that $f_0^{(3)}(\rho_0) = 0$. We now introduce a change of variables using a non-dimensional variable $\phi(\mathbf{r}) = \frac{\tilde{\rho}(\mathbf{r})}{\rho_1}$ where ρ_1 is some chosen constant density. Incorporating this non-dimensional ϕ into equations (4.3) and (4.5) we obtain:

$$F[\phi(\mathbf{r})] = \int d\mathbf{r}\left[f_0[\phi(\mathbf{r})] + \frac{1}{2}\phi(\mathbf{r})(A_2\nabla^2 + A_4\nabla^4)\phi(\mathbf{r})\right] \tag{4.6}$$

where $A_2 = \hat{A}_2/\rho_1^2$, $A_4 = \hat{A}_4/\rho_1^2$ and

$$f_0(\phi(\mathbf{r})) \approx a_1 + a_2\phi(\mathbf{r}) + \frac{a_3\phi(\mathbf{r})^2}{2} + \frac{a_4\phi(\mathbf{r})^4}{4}, \tag{4.7}$$

where a_1, a_2, a_3, and a_4 are constant. We now derive the dynamical model for PFC, starting with the DDFT equation Eq. (3.7) and consider the case when $\rho_1\phi$ is small. In this limit we can make the approximation $\Gamma\rho(\mathbf{r},t) = \Gamma(\rho_0 + \rho_1\phi) \approx \Gamma\rho_0$ and Eq. (3.7) becomes:

$$\frac{\partial\rho(\mathbf{r},t)}{\partial t} = \Gamma\rho_0\nabla^2\frac{\delta F[\rho(\mathbf{r},t)]}{\delta\rho(\mathbf{r},t)}. \tag{4.8}$$

This is known as "model B" dynamics in the classification of Hohenberg and Halperin [59]. Substituting in our original change of variable $\phi(\mathbf{r}) = \frac{\tilde{\rho}(\mathbf{r})}{\rho_1}$ into Eq. (4.8) we gain the time evolution of the order parameter $\phi(\mathbf{r},t)$:

$$\frac{\partial\phi(\mathbf{r},t)}{\partial t} = \alpha\nabla^2\frac{\delta F[\phi(\mathbf{r},t)]}{\delta\phi(\mathbf{r},t)} \tag{4.9}$$

where $\alpha = \frac{\Gamma\rho_0}{\rho_1^2}$. We now need an expression for the functional derivative of the free energy with respect to the order parameter, which is give by:

$$\begin{aligned}\frac{\delta F}{\delta\phi} &= a_3\phi + a_4\phi^3 + \frac{A_2}{2}\nabla^2\phi + \frac{A_4}{2}\nabla^4\phi + \nabla^2\left(\frac{A_2}{2}\phi\right) + \nabla^4\left(\frac{A_4}{2}\phi\right)\\ &= a_3\phi + a_4\phi^3 + A_2\nabla^2\phi + A_4\nabla^4\phi\\ &= a_4\left(\frac{a_3}{a_4}\phi + \phi^3 + \frac{A_2}{a_4}\nabla^2\phi + \frac{A_4}{a_4}\nabla^4\phi\right)\end{aligned} \tag{4.10}$$

If we now choose ρ_1 such that $\frac{A_4}{a_4} = 1$ and rewrite the other parameter values as $\frac{A_2}{a_4} = 2q^2$ and $\frac{a_3}{a_4} = r + q^4$, we get the commonly used PFC free energy:

$$F[\phi(\mathbf{r})] = \int d\mathbf{r} f(\phi(\mathbf{r})), \tag{4.11}$$

where

$$f(\phi) = \frac{\phi}{2}\left[r + (q^2 + \nabla^2)^2\right]\phi + \frac{\phi^4}{4}. \tag{4.12}$$

When we insert those same parameter values in Eq. (4.10) we get:

$$\frac{\delta F}{\delta\phi} = (r + q^4)\phi + \phi^3 + 2q^2\nabla^2\phi + \nabla^4\phi. \tag{4.13}$$

Now we consider the linear stability of the uniform state with $\phi = \phi_0$ to obtain the dispersion relation for the PFC model. We make the following substitutions:

$$\phi = \phi_0 + \delta\phi \qquad \delta\phi = \chi e^{i\mathbf{k}\mathbf{r}+\omega t}. \tag{4.14}$$

Where the constant χ is the amplitude of the mode with wave number $\mathbf{k}$. This is equivalent to Eq. (3.15) but since we will linearise the equation we need only consider one Fourier mode at a time. Eq. (4.13) now becomes:

$$\frac{\delta F}{\delta \phi} = \left(r + 3\phi_0^2 + \left(q^2 - k^2\right)^2\right)\delta\phi + O(\delta\phi^2). \tag{4.15}$$

From Eqs. (4.9) and (4.15) we then obtain the following expression for the dispersion relation:

$$\omega = -k^2\alpha\left[r + 3\phi_0^2 + \left(q^2 - k^2\right)^2\right]. \tag{4.16}$$

If we now consider Eq. (4.16), note that if $\omega < 0$ then the system is linearly stable and there is no solidification front or freezing via the spontaneous growth of any small amplitude density modulations - i.e. the system is linearly stable. The condition for the system to be linearly unstable is $\omega > 0$ and is conditional on $r > 3\phi^2 + (q^2 - k^2)^2$. Note that the right side of this condition will always be a positive number. To minimise it we must have $q \approx k$. Choosing the value for q effectively picks the wave number (i.e. wavelength) of the density modulations which will grow in amplitude. In Fig. 4.1 we display a plot of the dispersion relation showing the typical behaviour of the system. The curves are for $\phi_0 = 0$ and varying $\mathbf{r}$. We see that as $\mathbf{r}$ is increased, the peak at $k = q$ moves up and at $r = 0$ the system becomes marginally unstable -i.e. $\omega(k = q) = 0$ for $r = \phi_0 = 0$. For $r > 0$ the system is linearly unstable to periodic density modulations with wave number $k = q$. It is in this regime that a localised density perturbation grows and then advances into the unstable liquid with a well defined front speed [53].

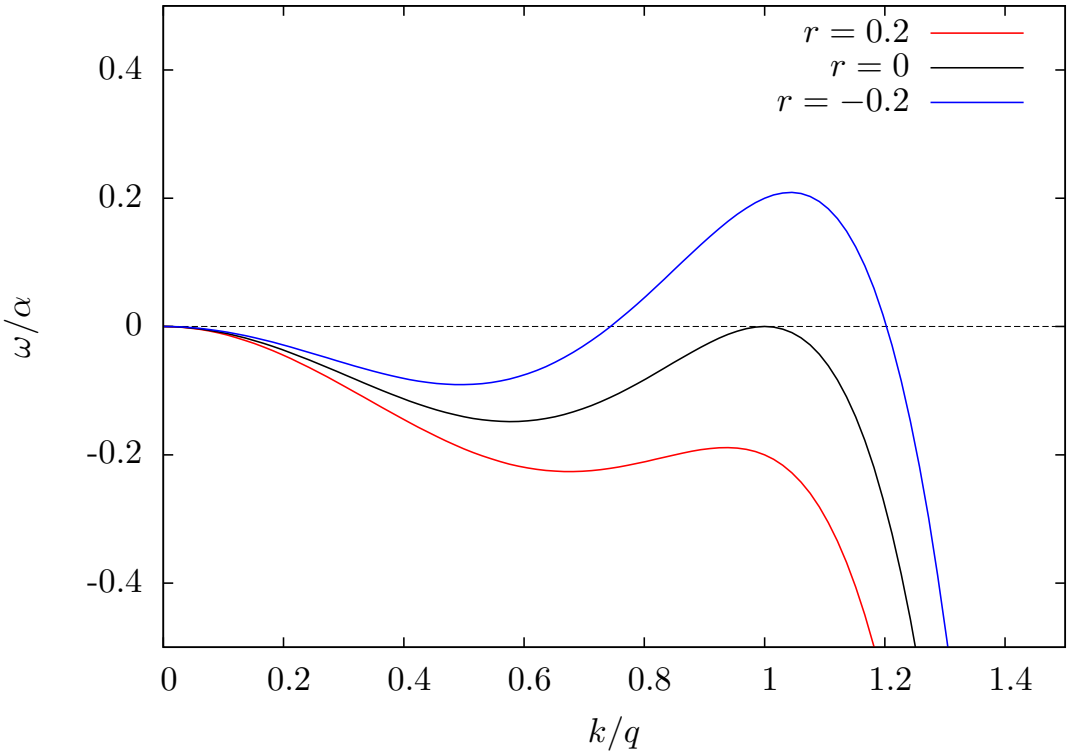

FIGURE 4.1: Dispersion relation for the PFC as the parameter r is varied.

4.2 Solidification Fronts

As mentioned in section 3.3 we define a solidification front as a front that advances through a bulk fluid leaving behind crystalline structure. Solidification fronts occur in unstable systems where the fluid has been deeply quenched into a region of the phase diagram where crystal is the equilibrium phase. By introducing a sufficient density disturbance into these non-equilibrium systems we can create a solidification front which advances through the fluid. The characteristics of the advancing fronts; the speed, shape and the structure of the solid phase left behind, are all dependant on the properties of the system. In Fig 4.2 we can see an example of the density profile for a solidification front advancing into an unstable bulk fluid of GEM-4 particles. This example shows how a structured crystalline region is left behind the front, in the form of density peaks.

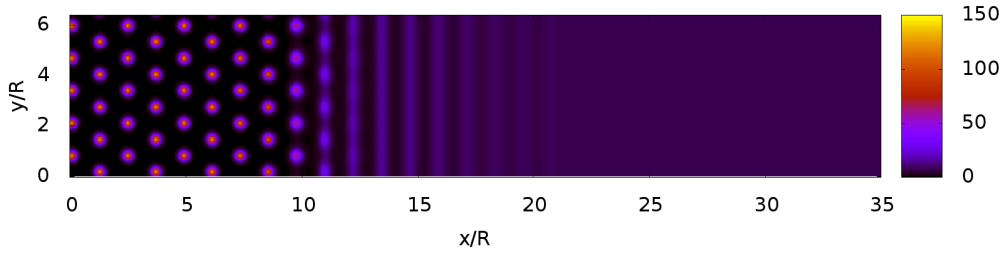

FIGURE 4.2: Density profile across a solidification front advancing from left to right into an unstable GEM-4 liquid with bulk density $\rho R^2 = 8$ and temperature $k_B T/\epsilon = 1$, calculated from DDFT.

When the system is linearly unstable, any localised density modulation will grow and advance into the unstable uniform liquid phase. In Refs. [60, 53], a marginal stability analysis was used to calculate the speed of such a front for the PFC model. Such a calculation allows one to obtain the speed of a front that has advanced sufficiently far for all initial transients to have decayed, so that the front attains a stationary front velocity. In 1D the speed c with which the front advances into the unstable liquid may be obtained by solving the following set of

equations [61, 62, 60, 53]:

$$\mathrm{i}c + \frac{d\omega(k)}{dk} = 0 \tag{4.17}$$

$$\mathrm{Re}[\mathrm{i}ck + \omega(k)] = 0, \tag{4.18}$$

where $k = k_r + k_{im}$ is a complex wavenumber. This pair of equations come from considering the system in a frame of reference moving with speed c, the speed of the front. In that frame the front solution moving with speed c that is marginally stable to infinitesimal perturbations in its frame of reference. In such a front the density profile has travelling component of the form $\tilde{\rho}(\mathbf{r}, t) = \rho_{\mathrm{front}}(x - ct)$, where $\rho_{\mathrm{front}}(x-ct) \sim \exp(-k_{\mathrm{im}}x)\sin(k_{\mathrm{r}}(x-ct)+\mathrm{Im}[\omega(k)]t)$ and in this expression we have also included the time periodic component. Thus k_r determines the wavelength of the density modulations in the front and k_{im} determines the width of the front i.e. decay envelope of the front. More importantly, if no phase slips take place, then the wavenumber of the density modulations left behind by the front is [62, 60, 53]:

$$k^* = k_r + \frac{1}{c} Im[\omega(k)]. \tag{4.19}$$

Thus, at this stage we can make an important observation: k^* is determined by the form of $\omega(k)$, which is obtained by linearising Eq. (3.1). Therefore the wavelength $2\pi/k^*$ of the density modulation created behind the advancing front is in general different from the equilibrium crystal lattice spacing ℓ, just like the wavelength associated with the fastest growing mode.

Thus even if the length scale determined by the maximum in $\omega(k)$ is the same as the equilibrium lattice spacing for the crystal, as is the case in the simple PFC theory for the crystal, solidification fronts advancing into a deeply supercooled liquid will still generate density modulations with a distinct wavelength, requiring substantial subsequent rearrangements of the system in order to form a defect-free crystal without strain. An example of using the above equations to calculate these wave numbers for a simple model is detailed in the next section.

4.3 Marginal stability calculation for simple model

In this section we perform the marginal stability calculation to obtain the front speed c and wavenumber k^* of the density modulations created behind the front to show how these quantities depend on the dispersion relation. We approximate the dispersion relation by making a Taylor expansion around the wavenumber corresponding to the principal peak and truncating after the k^3 term,

$$\omega(k) \approx \omega_m - a(k-q)^2 - b(k-q)^3, \tag{4.20}$$

where $\omega_m = \omega(k = q)$ is the maximum growth rate. The coefficient $a > 0$ is related to the width of the principal peak while b measures its asymmetry around the peak wavenumber $k = q$. Substituting Eq. (4.20) into Eq. (4.17) we obtain:

$$ic - 2a(d + ik_{\rm im}) - 3b(d + ik_{\rm im})^2 = 0, \tag{4.21}$$

where we have written $d = k_r - q$. Separating the real and imaginary parts of this equation, we obtain the following expressions for the front speed and the imaginary part of k:

$$c = 2(a + 3bd)k_{\rm im} \tag{4.22}$$

$$k_{\rm im} = \sqrt{\frac{2ad}{3b} + d^2}. \tag{4.23}$$

Substituting Eq. (4.20) into Eq. (4.18) we obtain:

$$Re[ic(k_r + ik_{\rm im}) + \omega_m - a(d + ik_{\rm im})^2 - b(d + ik_{\rm im})^3] = 0 \tag{4.24}$$

giving

$$-ck_{\rm im} + \omega_m - a(d^2 - k_{\rm im}^2) - b(d^3 - 3dk_{\rm im}^2) = 0. \tag{4.25}$$

Inserting Eqs. (4.22) and (4.23) into Eq. (4.25) we obtain a cubic equation to be solved for d. However, for present illustrative purposes it is instructive to proceed analytically on the assumption that d is a small quantity. In this case Eqs. (4.22) and (4.23) become

$$c \approx 2ak_{\mathrm{im}} \tag{4.26}$$

$$k_{\mathrm{im}} \approx \sqrt{\frac{2ad}{3b}}. \tag{4.27}$$

Linearization of Eq. (4.25) in d now leads to $d = 3b\omega_m/2a^2$, i.e. to

$$k_r \approx q + \frac{3b\omega_m}{2a^2}. \tag{4.28}$$

This result shows that the wavenumber k_r of the density modulation in the advancing solidification front is not equal to the wavenumber of the fastest growing mode for the quenched uniform fluid, q, unless the peak of the dispersion relation is symmetric, i.e. unless $b = 0$. We also see that the difference between these two wave numbers grows with ω_m, the magnitude of which is related to the degree of undercooling. The deeper the quench, the larger is ω_m. Moreover, inserting these results into Eq. (4.19) we obtain the wavenumber k^* of the modulations deposited behind the front:

$$k^* \approx q + \frac{b\omega_m}{2a^2}. \tag{4.29}$$

Thus the wavenumber k^* differs in general from the fastest growing wavenumber q, and neither of these wave numbers is in general equal to $2\pi/\ell$ and so defects and disorder must be present shortly after a deep quench. Some systems are subsequently able to rearrange, but others are not, as we show in the subsequent sections for a particular model fluid composed of soft-core particles.

4.4 Length scales in liquids and solids

In the previous section we have seen how a wave number is selected by a solidification front for a simple model. Even for this simple model the wave number k^* is not equal to the wave number of the fastest growing mode of the front q. This is true more generally,. Recall that the thermodynamic and structural properties of these two phases can in principle be found using classical DFT [1, 2, 4, 3]. In DFT it is shown that there exists a functional $\Omega[\rho]$, together with the minimisation principle in Eq. (2.10). The density profile $\rho^*(\mathbf{r})$ that minimises $\Omega[\rho]$, is the density distribution of the system at equilibrium. Furthermore, $\Omega[\rho^*]$ is the thermodynamic grand potential of the system. Solving Eq. (2.10) for state points in the phase diagram where the crystal is the equilibrium phase yields a density profile that exhibits a regular array of peaks. From this density profile, quantities such as the crystal lattice spacing ℓ can be determined.

The functional $\Omega[\rho]$ is highly nonlinear, and quantities characterising the crystal, such as ℓ, depend on all terms in the functional. In contrast, quantities such as the static structure factor $S(k)$ Eq. (2.27) of the liquid only depend on the linear response of the liquid and so only depend on the terms in $\Omega[\rho]$ that are quadratic in the density fluctuation $\tilde{\rho} \equiv \rho - \rho_0$. Related to the static structure factor is the Fourier transform of the linear density response function $\chi(\mathbf{r} - \mathbf{r}')$, viz., $\hat{\chi}(k) = -(\rho_0/k_BT)S(k)$, that relates the change in the density $\delta\rho(\mathbf{r})$ to a change $\delta V_{ext}(\mathbf{r})$ in the external potential [1]:

$$\delta\rho(\mathbf{r}) = -\int d\mathbf{r}'\chi(\mathbf{r},\mathbf{r}')\delta V_{ext}(\mathbf{r}'). \tag{4.30}$$

This formula applies for both uniform and non-uniform fluids; in particular, in the case of a uniform fluid with density ρ_0 and $V_{ext} = 0$ perturbed by a small amplitude external potential $\delta V_{ext}(\mathbf{r})$, Eq. (4.30) determines the resulting change

in the density profile: $\delta\rho \equiv \rho - \rho_0 = \tilde{\rho}$.[1]

The main point of the above comments is to emphasise that quantities pertaining to the crystal, such as ℓ, depend on all terms in $\Omega[\rho]$, but quantities such as $S(k)$ and the dispersion relation $\omega(k)$ [52, 53, 28], only depend on the quadratic terms in $\tilde{\rho}$. We emphasise this point because when a uniform liquid is deeply quenched, the length scales of the density modulations that initially grow after the quench are determined by $\omega(k)$ and so only depend on the quadratic terms in $\tilde{\rho}$. In particular, the principal peak in the dispersion relation $\omega(k)$ determines the wavenumber of the density fluctuation that grows the fastest. The fact that this wavenumber is determined by a quantity that only depends on the quadratic terms in $\tilde{\rho}$ shows that these fastest growing modes need not have the equilibrium wavenumber $2\pi/\ell$, i.e. they do not necessarily generate the correct density modulations for a perfect equilibrium crystal. From these considerations, one can infer that a deeply quenched liquid may well produce a disordered solid, because the length scale of the fastest growing modes is not in general equal to ℓ. This argument does not address whether, as solidification proceeds, the system can rearrange and subsequently anneal all the defects generated in the initial stages of the solidification process to produce a perfect crystal. Nonetheless, the observation that the initial dynamics after the quench do not in general produce density fluctuations of the correct length scale is an important observation.

[1] The result in Eq. (4.30) also applies to non-uniform liquids, i.e. to liquids initially at equilibrium with a density profile $\rho_{old}(\mathbf{r})$ in an external potential $V_{old}(\mathbf{r})$, disturbed by an infinitesimal change to the external potential, $V_{old}(\mathbf{r}) \to V_{new}(\mathbf{r})$. The resulting change in the density profile $\delta\rho(\mathbf{r}) \equiv \rho_{new}(\mathbf{r}) - \rho_{old}(\mathbf{r})$ is then also given by Eq. (4.30), where $\delta V_{ext}(\mathbf{r}) \equiv V_{new}(\mathbf{r}) - V_{old}(\mathbf{r})$.

Chapter 5

Solidification fronts in one component system

5.1 The GEM-4 system

In this chapter we show results we have obtained for solidification fronts in the GEM-4 system. As discussed in section 2.6, the theodynamic coexistence, at the temperature $T = T_{\rm coex}$ and the chemical potential $\mu = \mu_{\rm coex}$, a front between the crystal and the liquid state is stationary. However, on decreasing the temperature below $T = T_{\rm coex}$ (or increasing μ above $\mu = \mu_{\rm coex}$), the liquid state is no longer the equilibrium state. For a shallow quench, the liquid state remains linearly stable but a crystal can still grow if it is nucleated: only a crystal seed that is larger than the critical size grows and the interface (front) between the two phases advances at a well-defined speed $c_{\rm nl}$ determined by nonlinear processes [28, 63]. This (pushed) front propagation for the GEM-4 model is described now (see also [28]). At $T = T_{\rm coex}$, the front speed $c_{\rm nl} = 0$; as the temperature T decreases below $T_{\rm coex}$ the speed $c_{\rm nl}$ increases with increasing quench depth $|T - T_{\rm coex}|$. If the quench is to a temperature $T < T_{\rm sp}$, where $T_{\rm sp}$ is the temperature determined by Eq. (3.20) at which the uniform liquid becomes linearly unstable (i.e. the spinodal), then front propagation via linear processes is possible, with the speed c determined by the marginal stability analysis described in section 4.3. However, as can be seen from Eqs. (4.26), (4.27) and (4.28), $c = 0$ at $T = T_{\rm sp}$ since $\omega_m = 0$ at $T_{\rm sp}$. As

the temperature is decreased below $T_{\rm sp}$, c increases but remains less than $c_{\rm nl}$ for small $|T - T_{\rm sp}|$. In this regime the front remains a pushed front even though the liquid is already unstable [28, 63, 64]. However, the speed c increases faster than $c_{\rm nl}$ with decreasing T resulting in a crossover in speeds at temperature $T = T_{\rm x}$, where $T_{\rm x} < T_{\rm sp} < T_{\rm coex}$. At $T_{\rm x}$, the two speeds are equal, $c = c_{\rm nl}$, but for a sufficiently deep quench $c > c_{\rm nl}$, and for these temperatures ($T < T_{\rm x}$) it is the linear process that determines how the crystal state advances into the unstable liquid [28, 63, 64]. The variation of the speed of the crystallisation front with increasing chemical potential μ (at fixed temperature) is analogous to that described above for decreasing temperature (at fixed chemical potential). The metastable uniform liquid becomes linearly unstable at $\mu_{\rm sp} > \mu_{\rm coex}$ and for $\mu > \mu_{\rm sp}$ front propagation via linear processes is possible. However, it is only when $\mu > \mu_{\rm x} > \mu_{\rm sp}$ that linear processes govern the propagation of the front and the front speed is determined by the marginal stability result. In Fig. 5.1 (see also Fig. 4 of Ref. [28]) we show for a GEM-4 fluid with temperature $k_BT/\epsilon = 1$ that for $\beta\mu > \beta\mu_{\rm x} \approx 21$ the front speed obtained from solving the DDFT equations numerically in 2D does indeed agree precisely with the speed c predicted by the marginal stability analysis. Figure 5.2 (see also Fig. 6 of Ref. [28]) compares the wavenumber k^* deposited behind a front generated by a deep quench ($\mu > \mu_{\rm x}$, equivalently $T < T_{\rm x}$) with the wavenumber $k_{\rm eq}$ corresponding to the equilibrium crystal lattice spacing. Our aim below is to explore the consequences of the dramatic difference between k^* and $k_{\rm eq}$ revealed in the figure for the subsequent evolution of the solid phase, and to demonstrate that it is responsible for the inevitable presence of defects and disorder.

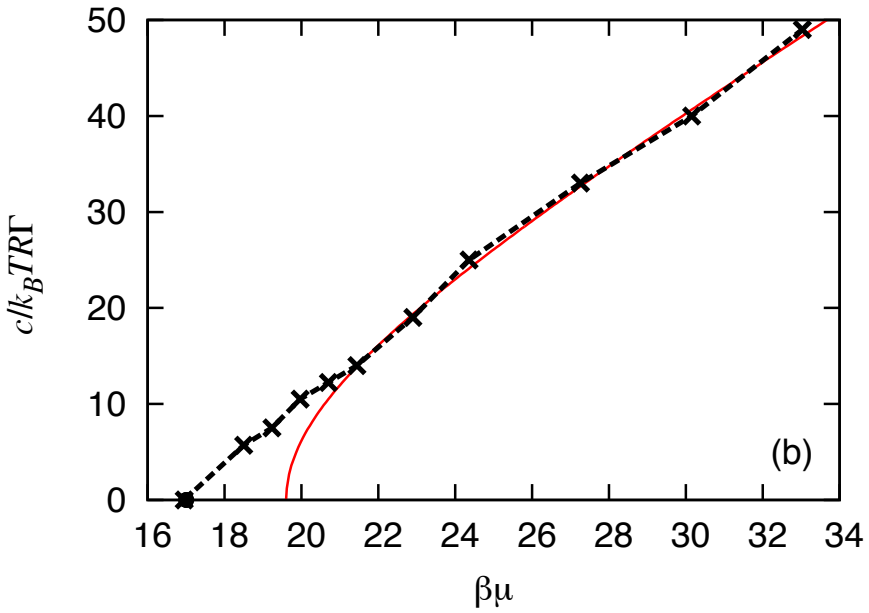

FIGURE 5.1: The front speed c as a function of the chemical potential μ for the GEM-4 fluid with temperature $k_BT/\epsilon = 1$. The solid line is the result of the marginal stability calculation while the symbols connected with a dashed line summarise the results from numerical simulations of the 2D DDFT equations.

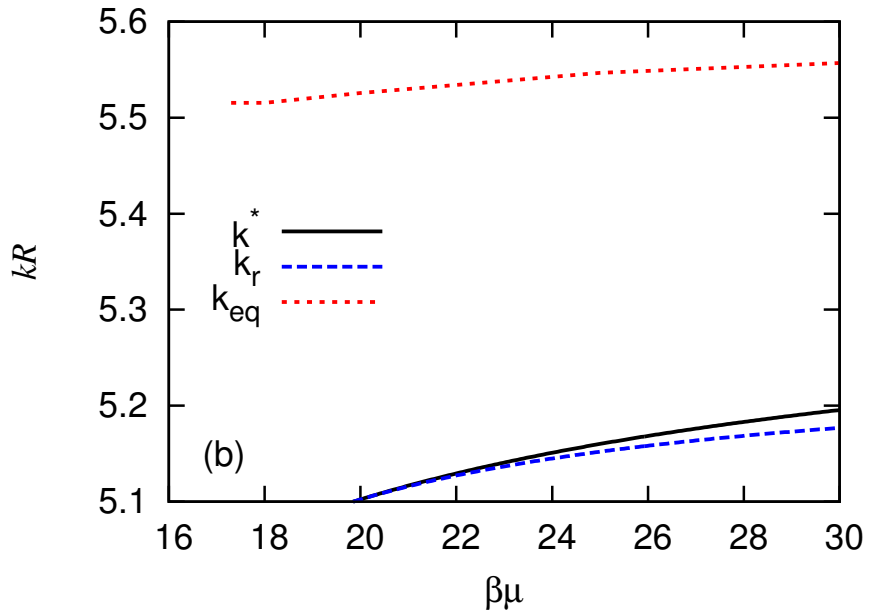

FIGURE 5.2: The wavenumber k_r of the density modulation selected by the moving front, the wavenumber k^* deposited behind the front (both calculated from the marginal stability condition), and the wavenumber $k_{\rm eq}$ of the equilibrium crystal. The difference between k^* and $k_{\rm eq}$ implies that rearrangements behind the front are inevitable as the system seeks to minimise its free energy.

5.2 Solidification front speed

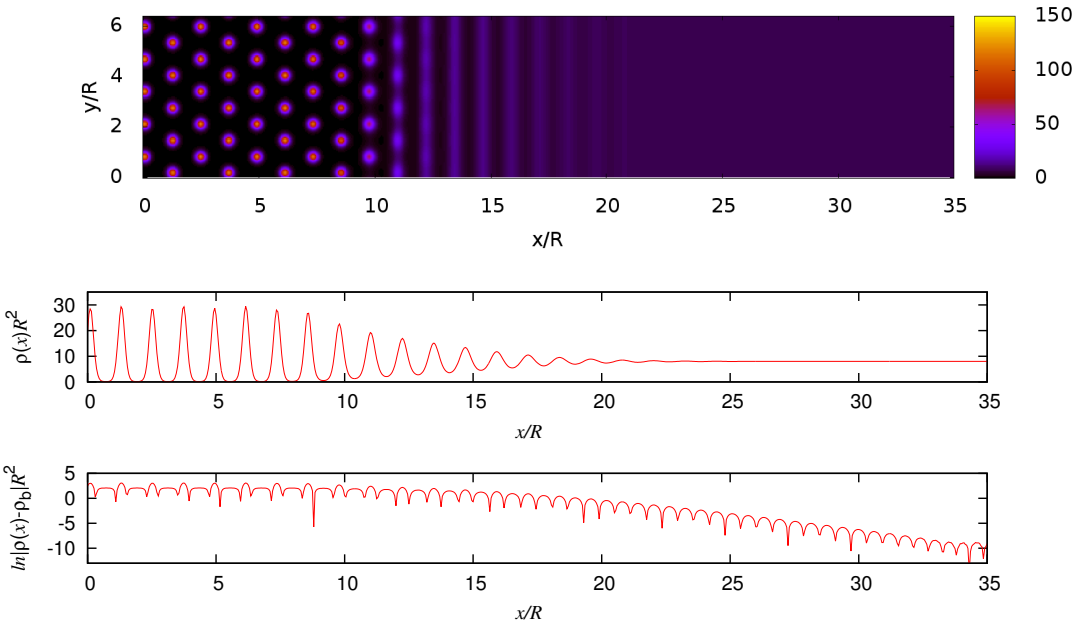

FIGURE 5.3: (Color online) Density profile across a solidification front advancing from left to right into an unstable GEM-4 liquid with bulk density $\rho R^2 = 8$ and temperature $k_BT/\epsilon = 1$, calculated from DDFT. The top panel shows the full 2D density profile $\rho(x, y)$ while the panel below shows the 1D density profile $\rho(x)$ obtained by averaging over the y-direction, perpendicular to the front. The bottom panel shows $\ln(|\rho(x) - \rho^b|R^2)$ in order to reveal the small amplitude oscillations at the leading edge of the advancing front.

Using Eqs (4.17-4.19) we are able to calculate properties of a solidification front, as shown in section 4.3. We show the results of these calculations in Fig. 5.2. The speed calculated from this approach for the one-component GEM-4 model is displayed as the solid red line in Fig. 5.1 as a function of the density of the unstable liquid and in Fig. 5.2 as a function of the chemical potential μ, both for $\beta\epsilon = 1$. We also display the front speed calculated numerically using DDFT in 2D. Figure 5.3 shows typical 2D and 1D density profiles used for determining the front speed c. The figure shows that the invasion of the metastable liquid state in fact occurs via a *pair* of fronts, the first of which describes the invasion of the liquid state by an unstable pattern of stripes, while the second describes the invasion of the unstable stripe pattern by a stable hexagonal state. By "stripes" we mean a

density profile with oscillations perpendicular to the front, but no density modulations parallel to the front. This double front structure complicates considerably the description of the invasion process in 2D – see Appendix in Ref. [28]. Figure 5.1 shows measurements of the speed of propagation of the hexagons-to-stripes front, obtained by comparing profiles like that in Fig. 5.3 (top) at two successive times and determining the speed of advance of the hexagonal state when it first emerges from the unstable stripe state. The speed of the stripe pattern is harder to measure since the pattern is itself unstable and so never reaches a substantial amplitude. For this reason we measure the speed of the stripe-to-liquid front from plots of the logarithm of the density fluctuations Fig. 5.3 (bottom) which emphasizes the spatial growth of the smallest fluctuations at the leading edge of the front.

For $\beta\epsilon = 1$ the uniform liquid is linearly stable for $\beta\mu \lesssim 19.6$ and unstable for $\beta\mu \gtrsim 19.6$. The marginal stability prediction, obtained by solving Eqs. (4.17) and (4.18), predicts that the 1D speed increases with $\beta\mu$ (or with increasing density ρ) in a square-root manner, as indicated by the solid red line in Fig. 5.1. Since the theory is 1D this prediction applies to the invasion of the liquid state by the stripe pattern. Despite this we find that the prediction correctly describes the speed of the hexagons-to-stripes front for $\beta\mu \gtrsim 21.5$ (i.e. for $\rho R^2 \gtrsim 7$), as measured in numerical simulations of the DDFT for the GEM-4 fluid, suggesting that the two fronts are locked together and that the front speed is selected by linear processes at the stripe-to-liquid transition, i.e., the resulting double front is a *pulled* front [65]. For smaller values of $\beta\mu$ the speed of the hexagonal state departs substantially from the marginal stability prediction and the stripe section is swallowed by the faster moving hexagons-to-liquid front. Indeed, for $\beta\mu \lesssim 19.6$ (i.e. for $\rho R^2 \lesssim 6.38$) the stripe state is absent altogether, as can be verified by performing a parallel study in one spatial dimension. The bifurcation to stripes is therefore supercritical. The hexagons-to-liquid front present in the metastable regime below the onset of linear instability of the liquid state is stationary at the

Maxwell point at $\beta\mu \approx 17.0$, corresponding to the location of thermodynamic coexistence between the liquid and hexagonal states. For $\beta\mu > 17.0$ the hexagonal state advances into the liquid phase (the opposite occurs for $\beta\mu < 17.0$) and the hexagons-to-liquid front is *pushed* [65]: in this regime the front propagates via a nonlinear process since the liquid phase is linearly stable. The situation is more subtle when plotted as a function of the liquid density ρR^2: when the liquid density takes a value in the interval $5.48 \lesssim \rho R^2 \lesssim 5.73$, i.e., between the densities of the liquid and crystalline states at coexistence, one cannot define a unique front speed. In this regime any front between these two states will slow down and, in any finite domain, eventually come to a halt. This occurs because the density ρ_0 of the liquid state into which the front moves is less than the density $\rho_{\rm s}$ of the crystal at coexistence but larger than the density $\rho_{\rm l}$ of the liquid at coexistence. In this situation, the moving 'front' has a substructure consisting of two transitions: one from $\rho_{\rm s}$ to a depletion zone of a density close to $\rho_{\rm l}$ and another one from the depletion zone to the initial ρ_0. As the depletion zone widens in time and limits the diffusion from the region of density ρ_0 to the crystalline zone of density $\rho_{\rm s}$ the front slows down. In a finite system, the depletion zone moves and extends until it reaches the boundary and the system equilibrates in a state partitioned between a liquid with density $\rho_{\rm l}$ and crystal with density $\rho_{\rm s}$ with a stationary front between them. For a PFC model the role of the depletion zone in crystal growth is discussed in Ref. [66].

The speed of the hexagons-to-liquid front in the regime $17.0 \lesssim \beta\mu \lesssim 19.6$ is determined uniquely (see Appendix in Ref. [28]). Refs. [63] and [67] predict that this is no longer the case for $\beta\mu \gtrsim 19.6$, but in practice we find that the front has a well-defined speed, possibly as a result of pinning of the stripes-to-liquid front to the stripes behind it, and of the hexagons-to-stripes front to the heterogeneity on either side. Both effects are absent from the amplitude equation formulation employed in Refs. [63] and [67]. Moreover, when the hexagon speed reaches the speed predicted by the marginal stability theory for the stripe state, the two fronts appear to lock and thereafter move together. In the theory based

on amplitude equations summarized in the Appendix in Ref. [28], the interval of stripes between the two fronts appears to have a unique width, depending on $\beta\mu$, a prediction that is consistent with our DDFT results. We have not observed the "unlocking" of the hexagons-to-stripes front from the stripes-to-liquid front noted in Ref. [63] at yet larger values of $\beta\mu$. Possible reasons for this are discussed in the Appendix of Ref. [28].

5.3 Consequences of wave number selection for the structure formed

It is clear, therefore, that the 1D analysis based on Eqs. (4.17) and (4.18) allows us to calculate the front speed when the unstable liquid is quenched deeply enough so that fronts propagate via linear processes. In addition to the front speed c this analysis gives $k_{\rm r}$, the wave number of the growing perturbation at the leading edge of the front and $k_{\rm im}$, which defines the spatial decay length of the density oscillations in the forward direction. Within the 1D description the pattern left behind by the front is a large amplitude periodic state with wave number k^*, say. When no phase slips take place, this wave number is given by Eq. (4.19). The wave number k^* differs in general from $k_{\rm r}$. Moreover, as demonstrated in Ref. [53] and confirmed in Fig. 5.2 for a GEM-4 crystal with temperature $\beta\epsilon = 1$, the wavelength $2\pi/k^*$ of the density modulation that is created by the passage of the front can be very different from the scale $2\pi/k_{\rm eq}$ of the minimum free energy crystal structure which corresponds here to hexagonal coordination. The propagation of the solidification front therefore produces a frustrated structure that leads to the formation of defects and disorder in the crystal. Thus, we identify two sources of frustration: the wave number mismatch and the competition between the stripe state deposited by the advancing front and its subsequent transformation into a 2D hexagonal structure with a different equilibrium wavelength. Both effects generate disorder behind the advancing front and significant rearrangements in the structure of the modulation pattern occur as the system attempts to lower its free energy via a succession of local changes in the wavelength of the density modulation [53].

This ageing process can be rather slow [53]. We illustrate its properties in Figs. 5.4 - 5.5. Figure 5.4 displays the density profile in a part of the domain as computed from DDFT, and confirms the presence of substantial disorder in the

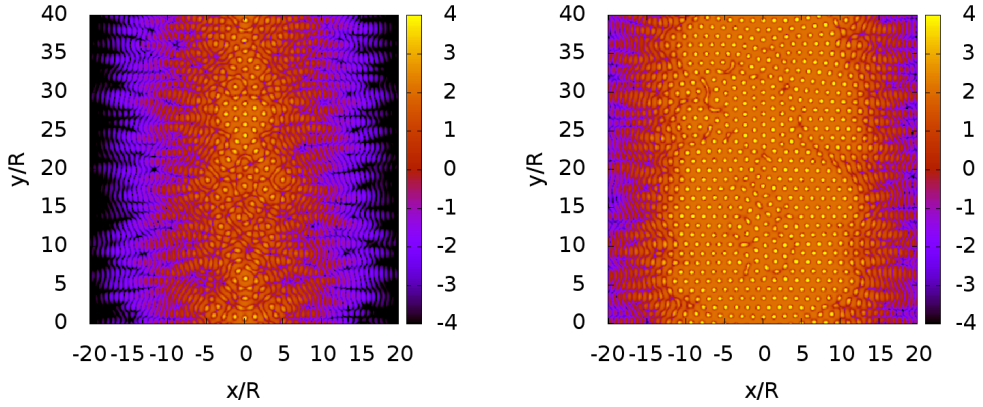

FIGURE 5.4: (Color online) Density profiles obtained from DDFT for an unstable GEM-4 fluid with bulk density $\rho_0 R^2 = 8$. To facilitate clear portrayal of the front structure we plot the quantity $\ln(R^2|\rho(\mathbf{r}) - \rho_0|)$. Solidification is initiated along the vertical line $x = 0$ at time $t^* = 0$. This produces two solidification fronts, one moving to the left, the other to the right, moving away from the line $x = 0$. The upper profile is for the time $t^* = 1$ and the lower for $t^* = 1.4$. We see significant disorder as the front creates density modulations that are not commensurate with the equilibrium crystal structure.

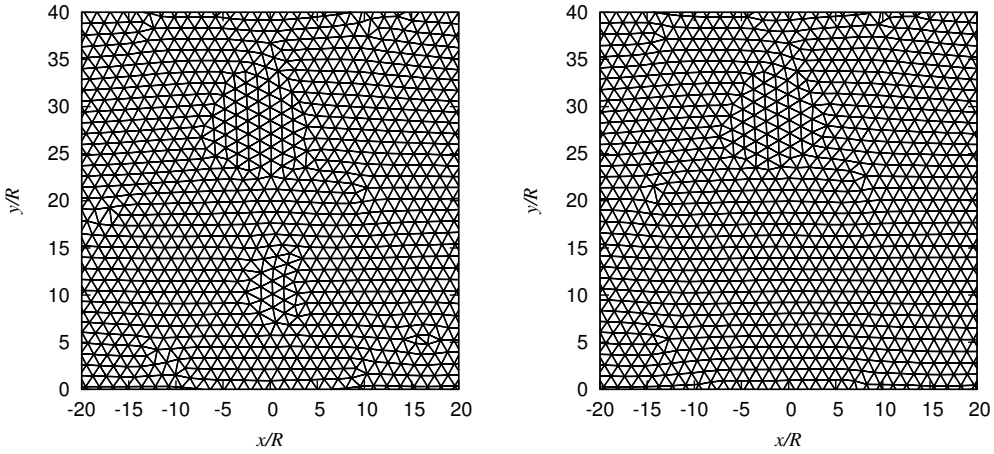

FIGURE 5.5: (cf. Fig. 5.4) computed from the triangles of a Delauney triangulation on the density peaks of the profile from DDFT (left panel: $t^* = 2.2$, right panel: $t^* = 4.4$).

crystalline structure close behind the advancing solidification front. There are actually two fronts in the profiles displayed in Fig. 5.4, moving to the left and to the right away from the vertical line $x = 0$, where the fronts are initiated at time $t = 0$. Although there is substantial disorder close behind the front, further back the crystal has had time to rearrange itself into its equilibrium structure, thereby reducing the free energy. Overall, the process is similar to that observed in the

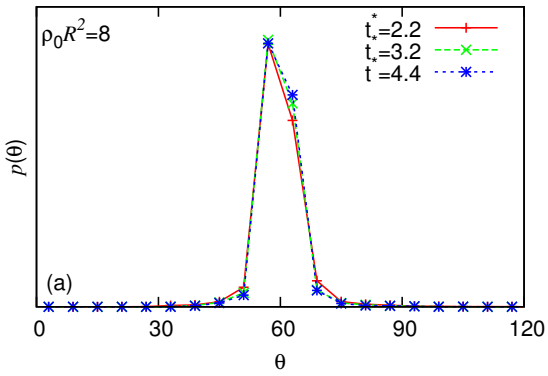

FIGURE 5.6: (Color online) Top panel: the angle distribution $p(\theta)$ at times $t^* = 2.2$, 3.2 and 4.4 after the initiation of a solidification front for a GEM-4 fluid with bulk density $\rho_0 R^2 = 8$.

PFC model [53]. We quantify the rearrangement process using Delauney triangulation [68], as shown in Fig. 5.5. Figure 5.6 displays the bond angle distribution $p(\theta)$ obtained from Delauney triangulation on the peaks of the density profile at various times after the solidification front was initiated. The distribution $p(\theta)$ has a single peak centered near 60°, which is not surprising since the triangulation on a hexagonal crystal structure yields equilateral triangles. The initial structure has a significant number of (penta-hepta) defects. Over time, the number of these defects gradually decreases, as shown by the fact that the width of the peak in $p(\theta)$ decreases over time, but the defects never completely disappear. These results show that the one-component GEM-4 system is able to rearrange itself after solidification to form a reasonably well-ordered polycrystalline structure, albeit with defects, but with the equilibrium scale $2\pi/k_{\rm eq}$ present throughout the domain.

Chapter 6

Solidification in binary systems

6.1 DDFT for binary systems

In this chapter we consider a binary mixture and the effect of having two types of molecules - i.e. two length scales in the system. As discussed above – in particular in Sec. 4.4, the length scale chosen by the solidification front is not always the one corresponding to the equilibrium length scale. This creates a disordered crystal structure that must rearrange over time, toward the equilibrium crystal structure. When we consider a binary mixture, the presence of the second species can lead to a glassy disordered structure, i.e. one which is a solid structure with density peaks, but does not have the long range order of the crystal. We also observe how changing the concentrations of the two species of molecules affects the structure of the system. The equations we use for the binary system are similar to the DDFT equations introduced in section 3.1. The two-component generalization of DDFT takes the form [69, 70]

$$\frac{\partial \rho_i(\mathbf{r},t)}{\partial t} = \Gamma_i \nabla \cdot \left[\rho_i(\mathbf{r},t) \nabla \frac{\delta \Omega[\{\rho_i(\mathbf{r},t)\}]}{\delta \rho_i(\mathbf{r},t)} \right], \tag{6.1}$$

where $\rho_i(\mathbf{r},t)$ are the time-dependent non-equilibrium fluid one-body density profiles, where $i = 1, 2$ labels the two different species of particles.

6.1.1 Stability of binary system

We now consider the stability properties of a uniform fluid binary mixture with densities ρ_1^b and ρ_2^b. We set the external potentials $V_{ext}^i = 0$ and consider small amplitude density modulations $\tilde{\rho}_i(\mathbf{r},t) = \rho_i(\mathbf{r},t) - \rho_i^b$ about the bulk values. Substituting $\tilde{\rho}_i(\mathbf{r},t)$ into Eq. (6.1) and linearising, we get:

$$\frac{\beta}{\Gamma_i}\frac{\partial\tilde{\rho}_i(\mathbf{r},t)}{\partial t} = \nabla^2\tilde{\rho}_i(\mathbf{r},t) - \sum_{j=1}^{2}\rho_i^b\nabla^2[\int d\mathbf{r}' c_{ij}^{(2)}(|\mathbf{r}-\mathbf{r}'|)\tilde{\rho}_j(\mathbf{r}',t)] + \mathcal{O}(\tilde{\rho}^2). \tag{6.2}$$

Note that the above equations reduce to Eq. (3.14) if the desnity of one of the species is set to zero. The quantities $c_{ij}^{(2)}$ are the pair direct correlation functions between the different species i and j. If we now consider Eq. (6.2) in Fourier space and ignore the terms of order $\tilde{\rho}^2$ and higher, we have:

$$\frac{\beta}{\Gamma_i}\frac{\partial\hat{\rho}_i(k,t)}{\partial t} = -k^2\hat{\rho}_i(k,t) + \rho_i^b\sum_{j=1}^{2}k^2\,\hat{c}_{ij}(k)\hat{\rho}_j(k,t), \tag{6.3}$$

where $\hat{}$ denotes the Fourier transform. If we assume that the time dependence of the Fourier modes follows $\hat{\rho}_i(k,t) \propto e^{\omega(k)t}$ we obtain:

$$\mathbf{1}\omega(k)\hat{\rho} = \mathbf{M}\cdot\mathbf{E}\hat{\rho}, \tag{6.4}$$

where $\hat{\rho} \equiv (\hat{\rho}_1, \hat{\rho}_2)$ and the matrices $\mathbf{M}$ and $\mathbf{E}$ are given by

$$\mathbf{M} = \begin{pmatrix} -k_BT\Gamma_1\rho_1^bk^2 & 0 \\ 0 & -k_BT\Gamma_2\rho_2^bk^2 \end{pmatrix}, \tag{6.5}$$

$$\mathbf{E} = \begin{pmatrix} \left[\frac{1}{\rho_1^b} - \hat{c}_{11}(k)\right] & -\hat{c}_{12}(k) \\ -\hat{c}_{21}(k) & \left[\frac{1}{\rho_2^b} - \hat{c}_{22}(k)\right] \end{pmatrix}. \tag{6.6}$$

It follows that

$$\omega(k) = \frac{1}{2}\mathrm{Tr}(\mathbf{M}\cdot\mathbf{E}) \pm \sqrt{\frac{1}{4}\mathrm{Tr}(\mathbf{M}\cdot\mathbf{E})^2 - |\mathbf{M}\cdot\mathbf{E}|}. \tag{6.7}$$

where $|\mathbf{M}\cdot\mathbf{E}|$ denotes the determinant of the matrix $\mathbf{M}\cdot\mathbf{E}$. When $\omega(k)<0$ for all wave numbers k, the system is linearly stable. If, however, $\omega(k)>0$ for any wave number k then the uniform liquid is linearly unstable. Since $\mathbf{M}$ is a (negative definite) diagonal matrix its inverse $\mathbf{M^{-1}}$ exists for all nonzero densities and temperatures, enabling us to write Eq. (6.4) as a generalised eigenvalue problem:

$$(\mathbf{E}-\mathbf{M^{-1}}\omega)\hat{\rho}=0. \tag{6.8}$$

As $\mathbf{E}$ is a symmetric matrix, all eigenvalues are real as one would expect for a relaxational system. It follows that the threshold for linear instability is determined by $|\mathbf{E}|=0$, i.e., by the condition

$$D(k)\equiv[1-\rho_1^b\hat{c}_{11}(k)][1-\rho_2^b\hat{c}_{22}(k)]-\rho_1^b\rho_2^b\hat{c}_{12}^2(k)=0. \tag{6.9}$$

6.1.2 Results for binary GEM-n mixtures

We use the GEM-n potential (section 1.1.1) generalised to a binary mixture as the effective interaction between molecules. The pair potentials are:

$$v_{ij}(r)=\epsilon_{ij}e^{-(r/R_{ij})^n}. \tag{6.10}$$

The parameter ϵ_{ij} defines the energy for complete overlap of a pair of molecules of species i and j and R_{ij} defines the range of interaction. In the following we obtain results for various concentrations ϕ of the two species i and j, where $\phi=\frac{\rho_1}{\rho_1+\rho_2}$, and different total densities $\rho=\rho_1+\rho_2$.

In Fig. 6.1 we display the linear instability threshold in the concentration ϕ versus total density ρ plane, for $\beta\epsilon_{ij}=1$, for all i,j, $R_{22}/R_{11}=1.5$ and $R_{12}/R_{11}=1$. For state points above the linear instability threshold line in Fig. 6.1 the uniform fluid is unstable and the system freezes to form a periodic solid. This line is obtained by tracing the locus defined by $D(k_c)=0$, where $D(k)$ is given by Eq. (6.9) and $k_c\neq 0$ is the wave number at the minimum of $D(k)$ (i.e. $\frac{d}{dk}D(k=k_c)=0$). The

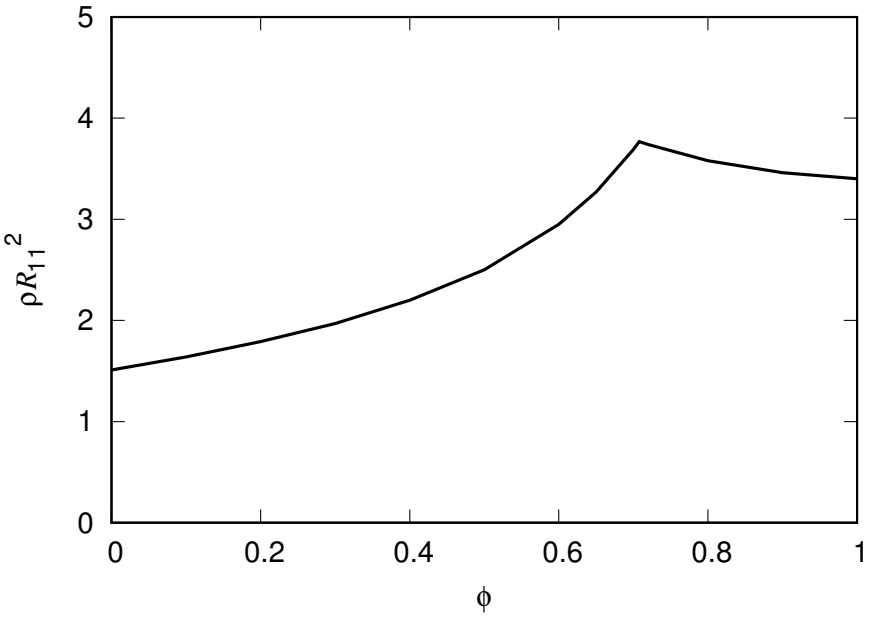

FIGURE 6.1: The linear stability limit for a binary mixture of GEM-8 particles with $\beta\epsilon = 1$ and $R_{22}/R_{11} = 1.5$ and $R_{12}/R_{11} = 1$, plotted in the total density $\rho \equiv \rho_1 + \rho_2$ vs concentration $\phi \equiv \rho_1/\rho$ plane.

cusp in the linear instability threshold in Fig. 6.1 is a consequence of a crossover from linear instability at one length scale to linear instability at a different length-scale. At the cusp point, which is at $\rho R_{11}^2 = 3.77$ and $\phi = 0.708$, the system is marginally unstable at two length scales [49]. We now consider quenching the uniform fluid to state points above the linear stability line in Fig. 6.1, and we study the structures formed in the wake of a solidification front.

In Fig. 6.2 we can see results for $\phi = 0.5$ – i.e. a 50:50 mix of the two species. The plots in Fig. 6.2 are for two distinct times, one soon after a solidification front has passed through the fluid (left) and one where the crystal structure has had time to rearrange (right). These two crystal structures are displayed in three different ways. The top two panels are Voronoi diagrams (see section 3.3) – the construction reveals the disorder created by the front. The hexagons and squares correspond to two competing crystal structures. The middle panels show the Delauney triangulation (see section 3.3) – domains of the hexagonal phase (equilateral triangles) are highlighted in red, while the remainder, including the right-angled triangles of the square phase, are shown in black. On the bottom panels in Fig. 6.2 we display the density maxima in $\rho(\mathbf{r})$. These are color-coded according

to the nature of the local crystal structure around that point. The square crystal regions are displayed as black circles, the hexagonal regions as red circles and the density peaks with neither square nor hexagonal local coordination are plotted as open circles. The criteria for deciding to which subset a given density peak belongs is based on the Delauney triangulation: any given triangle with corner angles θ_1, θ_2 and θ_3 is defined as equilateral if $|\theta_i - \theta_j| < 5^\circ$ for all pairs $i, j = 1, 2, 3$. The vertices of these triangles are colored black. Similarly, triangles are defined as right-angled if for the largest angle θ_1 we have $|\theta_1 - 90^\circ| < 5^\circ$ AND for the other two angles $|\theta_2 - \theta_3| < 5^\circ$. The vertices of these triangles are colored red. The remaining vertices which fall into neither of these categories are displayed as open circles. We see that there are roughly equal-sized regions of both square and hexagonal ordering. The typical size of these different regions increases with the elapsed time after the solidification front has passed through the system. Likewise, the number of maxima that do not belong to either crystal structure (open circles) decreases with elapsed time, as the system seeks to minimize its free energy. In Fig 6.3 we see how the change in the concentration ϕ effects the structure, not only right after the solidification front has past, at $t^* = 1$, but at a longer time scales $t^* = 50$ as well. When $\phi = 0.25$ we see that the system prefers to form a square structure, whereas when $\phi = 0.75$ the system prefers the hexagonal structure. At $\phi = 0.5$ the system forms both the square and hexagonal structure, with portions of neither structure in between. To characterise and understand further the rearrangements of the structure in further detail, we consider the bond angle distributions over time.

For three different concentrations $\phi = 0.25, 0.5, 0.75$ Fig. 6.4 through to Fig. 6.6 show the distribution function $p(\theta)$ for the different bond angles obtained from Delauney triangulation, for three different times after the initiation of the solidification front. The distribution shown in Fig. 6.5 with $\phi = 0.5$ has three maxima: one near 45°, another at 60° and the other near 90°. The peak at 60° is the contribution from the regions of hexagonal ordering (equilateral triangles) and the two

peaks at 45° and 90° come from the regions of square ordering (right-angled triangles in the Delauney triangulation). The peak at 45° is, of course, twice as high as the peak at 90°. We also observe that the peaks are much broader at short times, $t^* = 1, 2$, after the solidification front was initiated, than in the later structure from time $t^* = 50$. These results provide an indication of the degree of disorder and number of defects in the system; the fact that the peaks become sharper over time is a consequence of the fact that the amount of disorder in the system decreases over time. Nonetheless, the peaks in $p(\theta)$ are still rather broad in the final state, indicating that significant strain and disorder remain in the structure. This observation that broad peaks in the distribution function $p(\theta)$ indicates a higher level of disorder is even more visible when we consider Fig 6.4 with $\phi = 0.25$ i.e. where the majority of particles are species two $\rho_2 > \rho_1$. We see at time $t^* = 1, 2$ that the peaks are very broad and at a later time $t^* = 50$ the peaks have become sharper and are localised around 45° and 90°. These features indicate a large amount of disorder just after the front has advanced through the fluid and after a rearrangement period, the square structure is the preferred structure (see top right Fig 6.3). In Fig. 6.6 where $\phi = 0.75$ i.e. $\rho_1 > \rho_2$, we see a sharp peak at 60° indicating a dominant hexagonal structure. This is not suprising if we compare Fig. 6.6 to Fig 5.5 which is the distribution for the single species model of the same particle. What is particularly remarkable about these $\phi = 0.75$ results is that the peak at 60° is actually sharper at the early times ($t^* = 2$) than at later times ($t^* = 50$): over time the peak broadens! This is due to the fact that in this case the solidification front produces modulations with wavenumber k^* that is close to the wavenumber for the hexagonal crystal structure. However, these do not match exactly so that the hexagonal crystal that is initially formed is strained. Over time, the system lowers the free energy by *introducing* defects which alleviate the strain. These defects lead in turn to the broadening of the peak in $p(\theta)$ at 60°.

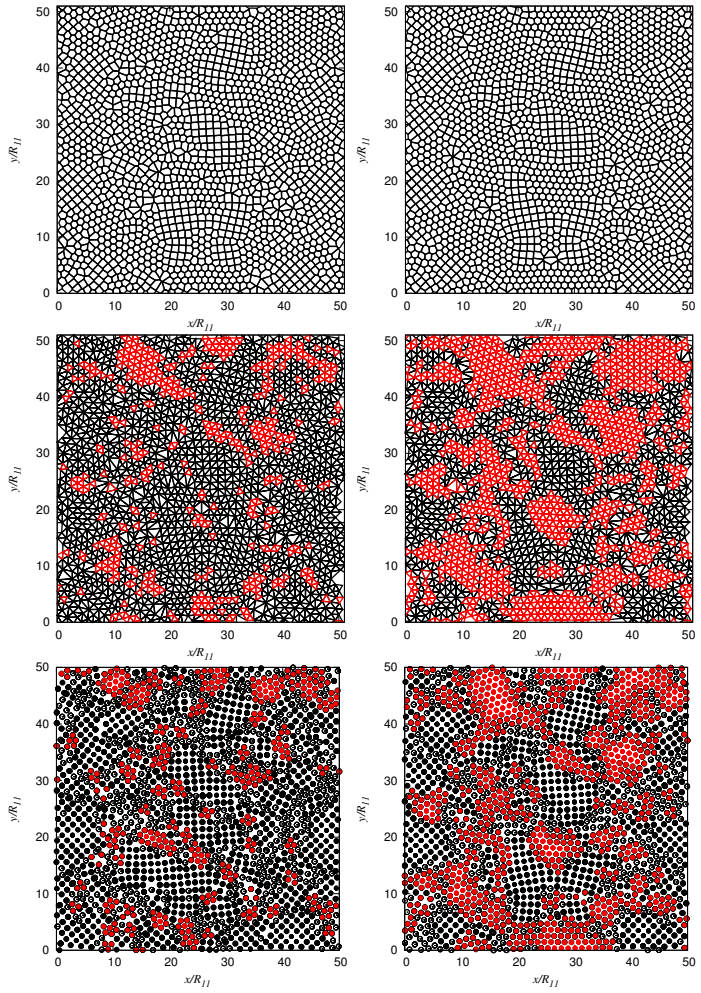

FIGURE 6.2: Analysis of the density peaks in the density profile in a GEM-8 mixture with $\beta\epsilon_{ij} = 1$ for all $i, j = 1, 2$, $R_{22}/R_{11} = 1.5$ and $R_{12}/R_{11} = 1$ and average total density $\rho R_{11}^2 = 8$ and concentration $\phi = 0.5$, formed by a solidification front initiated along the line $x = 25$ at time $t = 0$. The diagrams on the left correspond to time $t^* = 2$, shortly after the solidification front has exited the domain and before the structure has had time to relax, while the diagrams on the right correspond to time $t^* = 400$, when the profiles no longer change in time – the system has reached a minimum of the free energy. Top: Voronoi diagrams – the construction reveals the disorder created by the front. The hexagons and squares correspond to two competing crystal structures. Middle: Delauney triangulation – domains of the hexagonal phase (equilateral triangles) are highlighted in red, while the remainder, including the right-angled triangles of the square phase, are shown in black. Bottom: the density maxima are color-coded according to the triangle type they belong to: right-angled triangles are black, equilateral are red and scalene are open circles. Comparing the left and the right diagrams, we see that over time there is an increase in the size of the domains of the two different crystal structures.

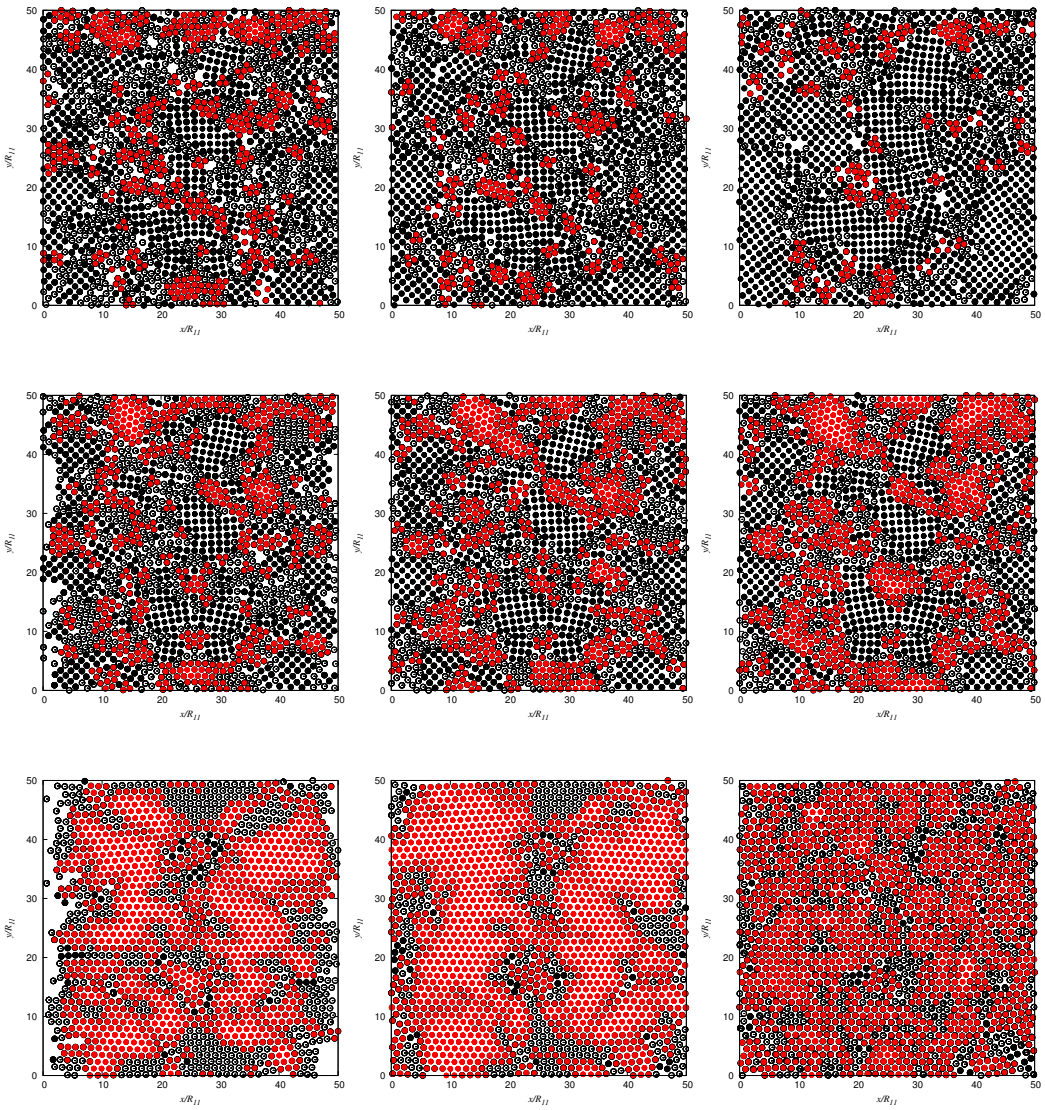

FIGURE 6.3: The peaks in the density profile formed by a solidification front initiated along the line $x = 25$ at time $t = 0$. The system is a GEM-8 mixture with $\beta\epsilon_{ij} = 1$ for all $i, j = 1, 2$, $R_{22}/R_{11} = 1.5$ and $R_{12}/R_{11} = 1$ and average total density $(\bar{\rho}_1 + \bar{\rho}_2)R_{11}^2 \equiv \bar{\rho}R_{11}^2 = 8$. The top row are profiles from a mixture with concentration $\phi = 0.25$, the middle row with $\phi = 0.5$ and the bottom row with $\phi = 0.75$. In each row the plot on the left is for an early time $t^* = 1$, shortly after the solidification front has exited the domain and before the structure has had time to relax, while the middle profiles are at $t^* = 2$ and the right hand profiles are at a later time $t^* = 50$. The density maxima are colour-coded according what kind of triangle they belong to in a Delauney triangulation: right-angled are black, equilateral are red and scalene are open circles. Portions of the hexagonal crystal is red, whilst the competing square crystal structure is black.

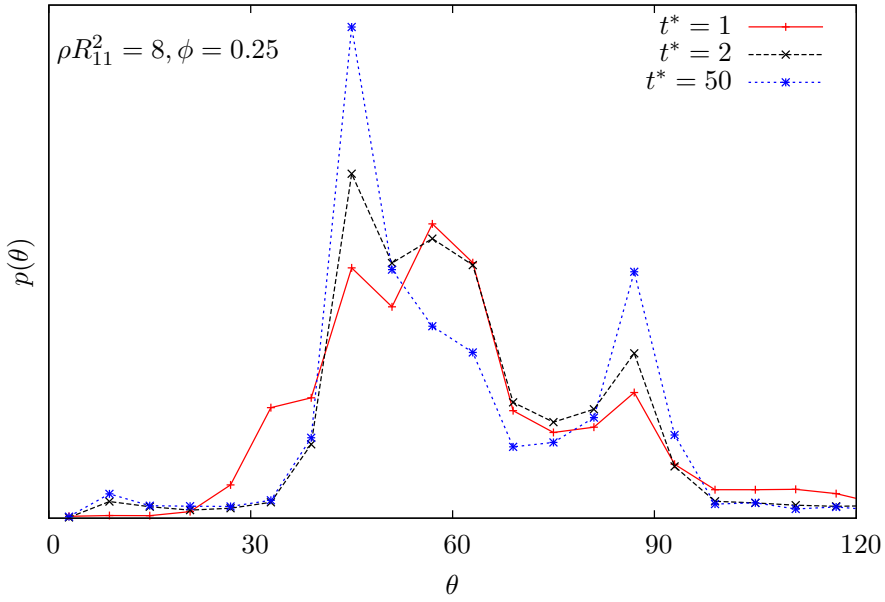

FIGURE 6.4: Time evolution of the bond angle distribution function from Delauney triangulation, corresponding to the top row of profiles in Fig. 6.3

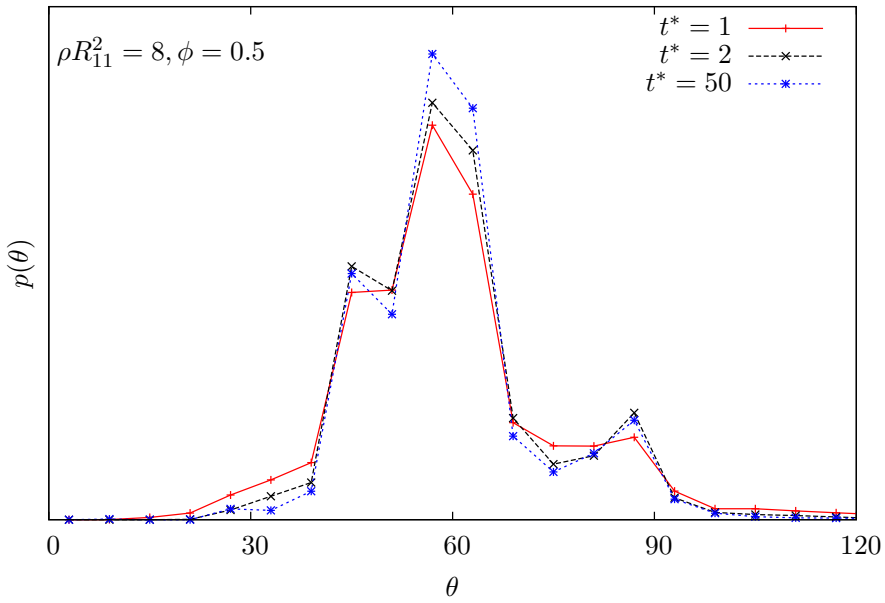

FIGURE 6.5: Time evolution of the bond angle distribution function from Delauney triangulation, corresponding to the middle row of profiles in Fig. 6.3

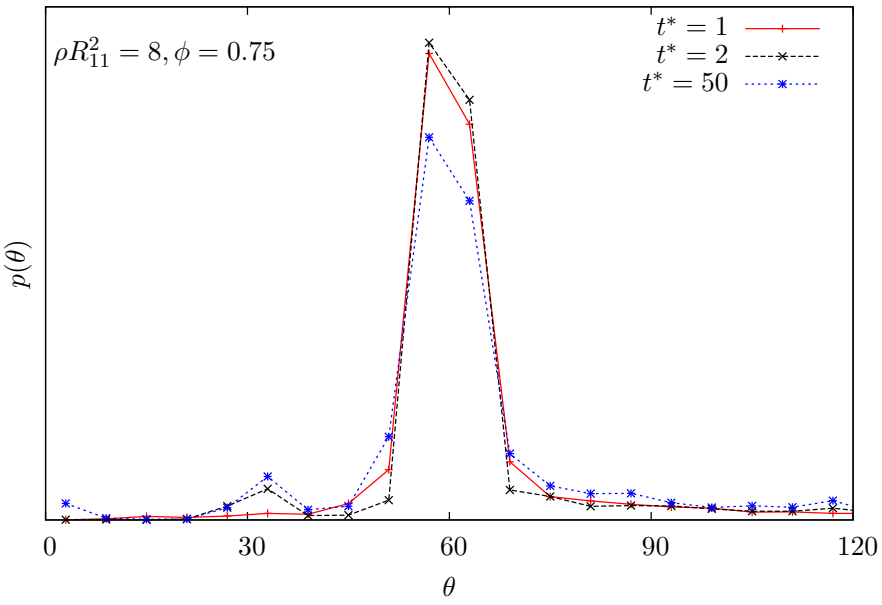

FIGURE 6.6: Time evolution of the bond angle distribution function from Delauney triangulation, corresponding to the bottom row of profiles in Fig. 6.3

6.2 Concluding remarks

In this chapter we have discussed a mechanism that results in the formation of disordered structures, when a liquid is deeply quenched to temperatures where the thermodynamic equilibrium state is a well-ordered crystal. This occurs because solidification fronts in deeply quenched liquids propagate via a mechanism that generates periodic density modulations in the system with wavelength that is not necessarily the same as the wavelength required for an equilibrium crystal. The wavelength mismatch means that the formation of a well-ordered equilibrium crystal state requires significant rearrangements after the front has passed. In monodisperse one-component systems, these rearrangements should generally be possible; this is certainly the case in the model fluid studied in chapter 4. However, for polydisperse systems or multi-component mixtures, such as the binary mixtures studied here, these rearrangements are frustrated and in some cases hindered by the fact that there is a variety of particle sizes in the system. We should emphasise that the front propagation mechanism focused on in this chapter operates only when the quench is sufficiently deep, to temperatures below the crossover temperature $T_{\rm x}$. Only for $T < T_{\rm x}$ do solidification fronts propagate via the linear mechanism, with the speed v and wavenumber k^* determined by linear considerations. Above $T_{\rm x}$ the front speed is determined by nonlinear considerations and in this regime the structure formed behind the front is generally much better ordered.

The results presented in this section are for rather simple 2D model systems composed of soft particles. Nevertheless, we believe that the mechanism that we describe should be rather general, although much further work is required to determine the nature of crystallisation fronts in other deeply quenched systems, and in particular to determine whether one can reach the regime where the fronts propagate via the linear mechanism that we describe. In other systems, it may be the case that the speed c never overtakes $c_{\rm nl}$. For example, it is not known whether

this regime is physically accessible for particles with a hard core; it may be that this regime only arises at densities near or even beyond random close-packing.

We should also mention that the mechanism described here is not the only means of introducing disorder as liquids solidify. Other mechanism include: (i) Defects created by impurities. (ii) Different grains, with defects on the grain boundaries, generated in the nucleation regime when growing crystals with different orientation nucleated at different points in the system collide. (iii) Defects introduced by crystal growth under the influence of external forces or shear. (iv) Disordered materials produced in shallow quenches where the growing crystal forms dendritic type structures (diffusion limited growth), leading to the formation of crystal grains and defects.

Chapter 7

Correlations in the liquid state of a two–length scale model

7.1 BEL potential

In this chapter we study a two dimensional system of particles interacting via a pair potential not considered previously in this thesis. We refer to this pair potential as the BEL potential, since it was introduced by Barkan, Engel and Lifshitz in Ref. [71]. It combines a Gaussian envelope with a polynomial of order 8:

$$v(r) = \epsilon e^{-\frac{1}{2}\sigma^2 r^2}(1 + C_2 r^2 + C_4 r^4 + C_6 r^6 + C_8 r^8). \tag{7.1}$$

As with the GEM-n systems, where the energy required for one particle to sit directly on top of another is finite and is determined by the parameter ϵ, in the BEL model the energy penalty for complete overlap is also determined by the parameter ϵ. The parameter σ determines the diameter of the particles and the coefficients C_n for $n = 2, 4, 6$ and 8 are constants. In Fourier space Eq. (7.1) becomes:

$$\hat{v}(k) = \epsilon e^{-\frac{k^2}{2\sigma^2}}(D_0 + D_2 k^2 + D_4 k^4 + D_6 k^6 + D_8 k^8). \tag{7.2}$$

It is because of this simple form that this potential is used – it gives a high level of precision to control the shape and where minima occur in both real and Fourier

space. This precision allows us to find solid phases that require very specific conditions. One of the features of the BEL potential is that multiple length scales can arise. This is a vital ingredient in the formation of Quasicrystals (QC) and the BEL model does indeed form QC. They can be found in metals, colloidal systems and soft matter systems, among others. Unlike crystals, which are regular ordered arrangements of atoms or molecules with rotational and transitional symmetries, QCs, discovered in 1982 [72], lack the periodic lattice structure [73]. The possibility of designing soft-matter QCs that self assemble has generated considerable interest. Due to their high degree of rotational symmetry such materials could have useful applications owing to their novel optical properties [74, 75]. Some important insights into the mechanisms for QC formation in soft matter were gathered from understanding the mechanisms for the formation of quasipatterns in Faraday wave experiments [76, 77]. A nice recent review drawing these connections together is Ref. [78]. The insight of this work is that it is the coupling of periodic modes with different length scales, that can give rise to QC. An important paper that helped make the connection to soft matter QC, was Ref. [79], which generalised the Swift-Hohenberg equation (an equation akin to the phase field crystal model in Chapter 4, but with a non-conserved dynamics) to include two length scales. It is this interaction of modes at two length scales that we observe using the BEL potential and describe in further detail below. While QC structures can be stabilised under certain conditions, this does not necessarily mean that QC structures correspond to the global minima of the free energy. In fact, for the model studied in [73] it was shown that the QC is not the minimum free energy state, but that nonetheless the QC forms for dynamical reasons.

Fig 7.1 shows the BEL potential for various values of C_4 while C_2, C_6 and C_8 remain constants – the values used are given in the caption of Fig. 7.1. The given values of C_2, C_6 and C_8, together with $C_4 = 0.439744$ are the values proposed by Barkan *et. al.* [71] because, as discussed below, this gives a system that is marginally unstable at two particular wave numbers. By varying only C_4 we get

a potential that changes from having two minima to a potential with one minimum. When $C_4 = 0.42$ there are two minima, at $r \approx 1.5, 3.5$, but when $C_4 = 0.55$ there is only one minimum at $r \approx 1.2$. The control over the shape of the potential is important because its shape affects the length scales it produces. The importance of these length scales is discussed below.

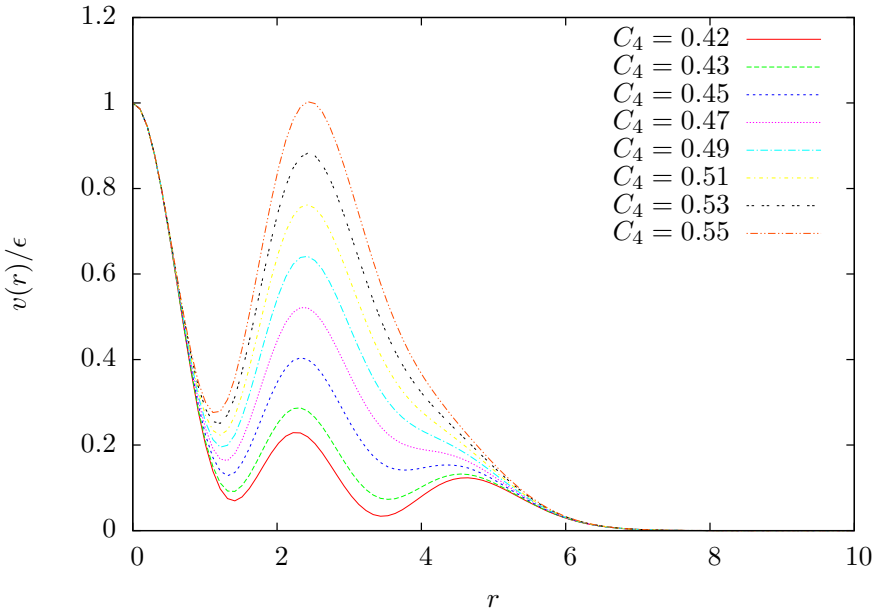

FIGURE 7.1: The BEL potential in Eq. (7.1) where we show the effect of changing only C_4 while the other parameters remain constant with values: $\sigma = 0.770746$, $C_2 = -1.09456$, $C_6 = -0.0492739$ and $C_8 = 0.00183183$.

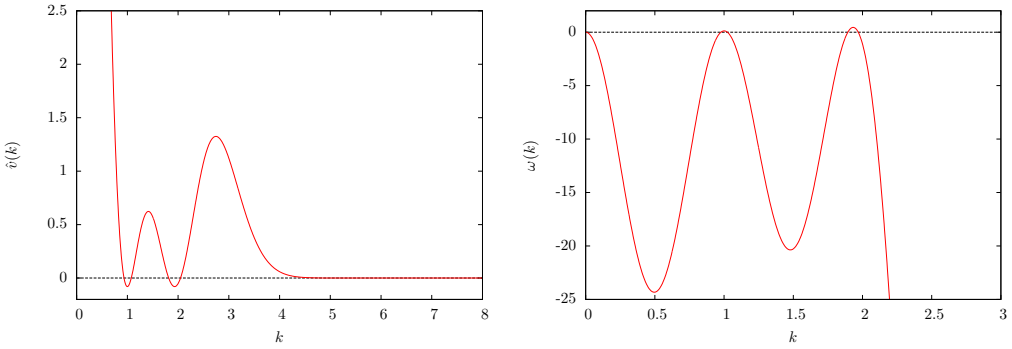

FIGURE 7.2: Left: The Fourier transform of the BEL potential displayed in Fig 7.1 with $C_4 = 0.44$. Right: The corresponding dispersion relation for when the fluid has density $\rho_0 = 1.3$ and $\beta\epsilon = 10$. The peaks in $\omega(k)$ are at $k = k_1 \approx 1$ and $k = k_2 \approx 1.93$.

In Fig. 7.2, we display the Fourier transform of the BEL potential (left). We see that for this value of C_4, the Fourier transform of the potential has two minima

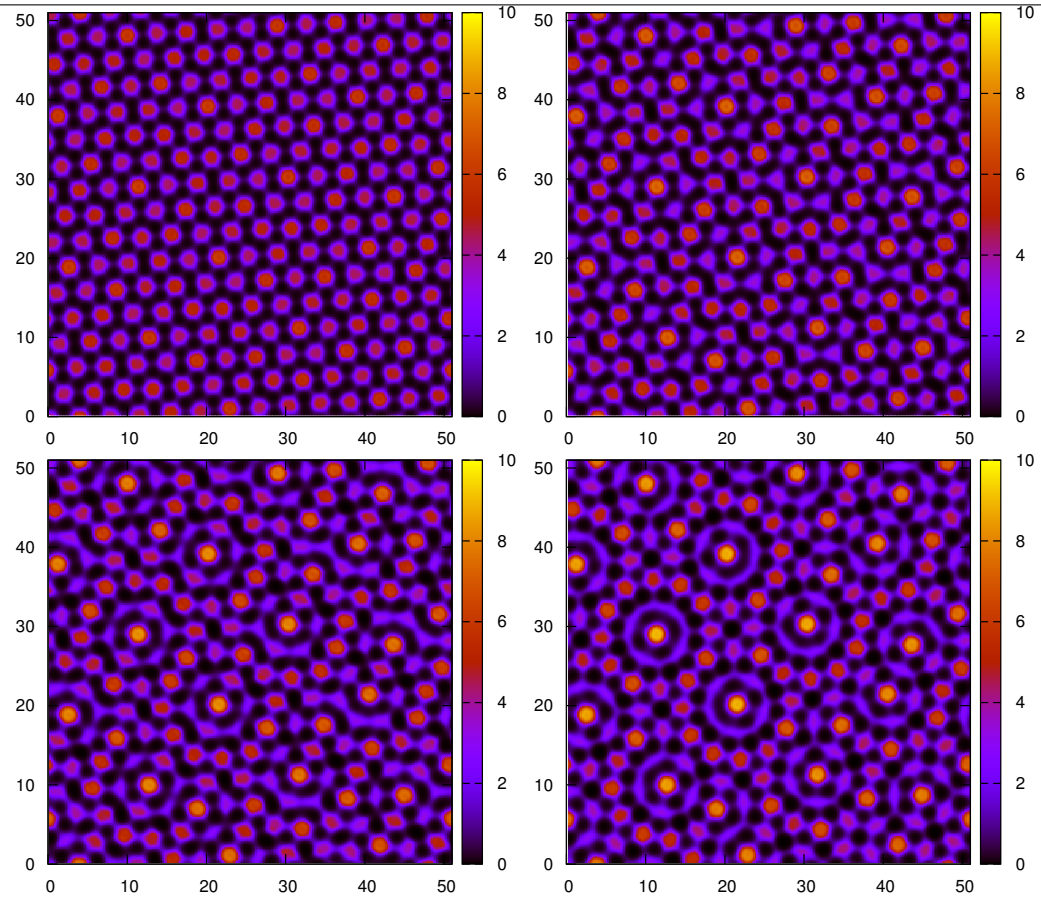

FIGURE 7.3: DDFT results for the time evolution of the density after a quench with $C_4 = 0.44$, $\rho_0 = 1.3$ and $\beta\epsilon = 10$. We see 12 fold Quasicrystal structure formation, although in the early stages, the shorter length scale is more visible. The profiles are for the times $t^* = 16$ (top left), $t^* = 40$ (top right), $t^* = 80$ (bottom left) and $t^* = 200$ (bottom right).

at $k_1 \approx 1$ and $k_2 \approx 1.93$. On the right we display the dispersion relation $\omega(k)$, defined in Eq. (3.17), for the uniform fluid with density $\rho_0 = 1.3$. We see that at this state point $\omega(k)$ has two maxima, at $k_1 \approx 1$ and $k_2 \approx 1.93$. Since the value of $\omega(k)$ is positive for these two wave numbers, the fluid is linearly unstable, so quenching the uniform fluid to this state point leads to solidification. The presence of two unstable wave numbers means that the system favours two distinct length scales, $2\pi/k_1$ and $2\pi/k_2$. In Fig. 7.3 we show DDFT results [i.e. from solving Eq. (3.7)] for the time evolution of the density profile following a quench. The $t = 0$ initial density profile is the uniform density plus a small amplitude random value at each point in space. We observe the initial growth of both length scales, as predicted by the dispersion relation. Note that since the peak in $\omega(k)$ at k_2 is

higher than the peak at k_1, the density modulations with wave number k_2 initially grow faster, as can be seen in the top left profile for $t^* = 16$ in Fig. 7.3 where the smaller length scale density modulations are more clear to see. However, the subsequent non-linear evolution maintains both length scales to produce the QC structure seen for $t^* = 200$, which is the final equilibrium. The presence of these two competing length scales and the ability to control their position in both real and Fourier space is one of the main reasons this potential was created, as explained in [71]. In their paper, Barkan, Engel and Lifshitz find many different crystal structures including regular hexagonal, stripe phase and QC's.

7.1.1 Length scales

As discussed above in section 7.1, the length scales that arise from the pair potential determine the structures formed during solidification, following a quench of the uniform liquid. Initially, after the quench, the two different wavelength density modes can grow. Subsequently, as the amplitudes grow, in the non-linear regime it is possible for the density modes of varying wavelength to interact with each other (i.e. become coupled), resulting in interesting non-uniform structures. The structures created depend on how these density modes interact with each other. QC formation is just one example of a structure that requires multiple length scales.

The understanding of how modes at different wavenumbers couple was worked out in Refs. [80, 79, 81, 82, 83, 84]. Following this initial work, there have been several applications and extensions in the context of soft matter [71, 85, 86, 87, 88, 73, 76, 89]. The key ideas are as follows: By considering the dispersion relation Eq. (3.17) we can determine the linear stability of a system, and its shape depends on the pair potential. On the right hand side of Fig. (7.2) we see the dispersion relation for the BEL potential, which is typical for these QC forming systems and is unlike the dispersion relation in the GEM-n case because there are two maxima i.e. two wave numbers k for which the liquid is linearly unstable. If we consider

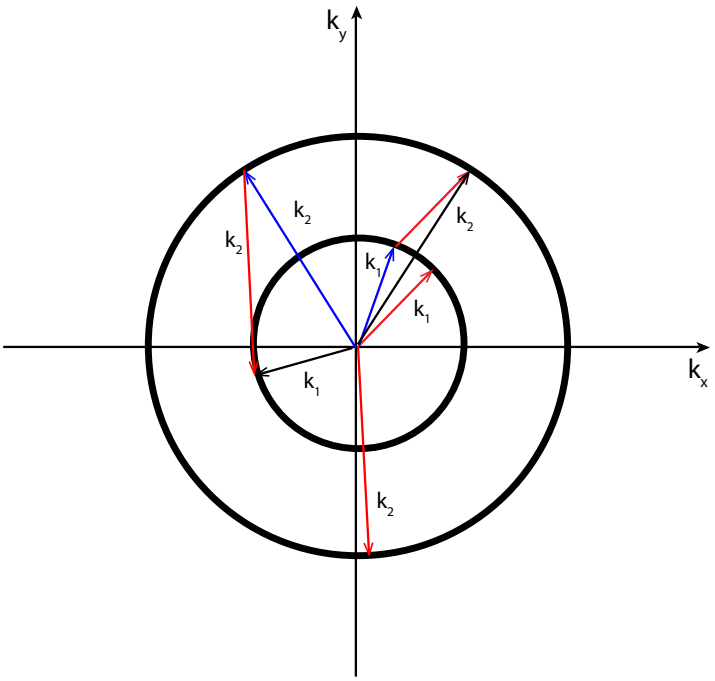

FIGURE 7.4: Plot showing wave vectors of density modes in the (k_x, k_y) plane. The dispersion relation has two peaks, hence the modes involved are in two rings: The inner ring is where $|\mathbf{k}| \approx k_1$ and the outer ring where $|\mathbf{k}| \approx k_2$. These are the wave numbers $\mathbf{k}$ of the density modes that grow over time. All other wave numbers not on or close to these rings decay. The blue and red vectors show the initial two waves, the black vector shows the resultant wave created by the interaction.

too, the time evolution – see Eq.(3.15) – we see that only wave numbers with $|\mathbf{k}| \approx k_1, k_2$ will initially grow, which allows us to express the density perturbations Eq. (3.17) as a sum over the leading order modes with wavenumbers k_1 and k_2:

$$\tilde{\rho}(\mathbf{r}, t) = \sum_{j=1,|\mathbf{k}_j|=k_1}^{\infty} \tilde{\rho}_{\mathbf{k}_j} e^{\omega t} e^{i\mathbf{k}_j \cdot \mathbf{r}} + \sum_{j=1,|\mathbf{k}_j|=k_2}^{\infty} \tilde{\rho}_{\mathbf{k}_j} e^{\omega t} e^{i\mathbf{k}_j \cdot \mathbf{r}} + \ldots \tag{7.3}$$

where the initial ($t = 0$) amplitudes $\tilde{\rho}_{\mathbf{k}_j}$ are assumed to be small. In the subsequent non-linear evolution it is possible for these modes to combine. These wave interactions creates a variety of different patterns and has a marked effect on the density profiles.

When two waves interact with each other and create a third wave this is known as a 3 wave interaction (3WI). For example, in the (k_x,k_y) plane displayed in Fig. 7.4 we consider two outcomes of 3WIs. In one case two waves with small

wave numbers $|\mathbf{k}| \approx k_1$ interact at a specific angle, and are able to create a wave with $|\mathbf{k}| \approx k_2$. The same is possible for two waves with larger wave number $|\mathbf{k}| \approx k_2$ which can combine to create a wave with $|\mathbf{k}| \approx k_1$. In the cases in Fig. 7.4 we see an example of two 'inner' (short) wave vectors, the red and blue vectors of length k_1, summing (i.e. interacting) to produce a third wave (black) with wave number k_2. We also see a red and a blue 'outer' (long) wave vectors summing to form an inner mode. QC arise when the non-linear interactions reinforce the coupling between modes. It also requires the 3WIs to close - by this we mean that the set of modes that are involved is finite. As illustrated in Fig. 7.4, we see two inner modes coupling to create a mode on the outer circle and two outer modes coupling to create an inner. In general, this process of creating new modes can go on indefinitely. However, when the ratio of the radii of the inner and outer circles are particular values, then this process ends – i.e. one can find only a finite set of wave vectors. When $k_1/k_2 = 2\cos(75^\circ) = 0.5176$, then one finds a closed set of 12 equally spaced vectors on the outer circle together with 12 others on the inner circle [84]. These modes couple to reinforce on another and create a structure with 12-fold symmetry, a dodecagon. One cannot tile the plane with such a shape, i.e. one can not form a regular crystal from a unit cell with this symmetry. Instead, the system forms a QC. For more information on QC formation see [71, 80, 79, 81, 82, 83, 84, 85, 86, 87, 88, 73, 76, 89] and references therein.

7.2 Liquid state correlations

Having discussed how multiple length scales can create various solid structures including QC's, we now focus on the effect these length scales have on the liquid state structure. Knowing the structure of the (linearly stable) equilibrium liquid, is important for determining the thermodynamics of the system and gives insight when considering how and why a liquid freezes. As in Section 2.4, we use both the test particle method together with the RPA-DFT, Eq. (2.24), and also the HNC approximation in the Ornstein Zernike equation (2.33) to calculate the radial distribution function $g(r)$. Three examples, for $C_4 = 0.42$ and bulk densities $\rho_0 = 0.1, 0.5$ and 1.0 are displayed in Fig. 7.5 and for $C_4 = 0.43$ and the same three densities in Fig. 7.6. If we compare Figs 7.5–7.6 to Fig 2.4 we can see the influence of the two length scales on $g(r)$. If we consider the higher density plots in Figs. 7.5–7.6 we see a split second peak emerging at about $\rho_0 \approx 1$. This is usually attributed to freezing [90]. However, in the present case the state points where this occurs are far in the phase diagram from where freezing occurs (and even further from where the linear instability line is located) and therefore the split peak can not be related to freezing. Here, the split peak come from the multiple length scales in the pair potential. Also note that the agreement between the HNC approximation and the RPA-DFT is rather good, despite the highly complex liquid structure. Since for such soft core systems the HNC is generally highly accurate [7] the good agreement gives confidence that the RPA-DFT is accurate, so in the remainder this is the theory that we use.

Important insight into the length–scales that dominate the correlations in the liquid state can be obtained by studying the asymptotic $r \to \infty$ decay of $g(r)$, or equivalently of $h(r)$ (recall $h(r) = g(r) - 1$, see Sec. 2.3 for more details). Some early work on the asymptotic decay of correlation functions was that of Fisher and Widom [91], who considered a one dimensional system with only nearest neighbour interactions. They found that at a certain line in the phase diagram

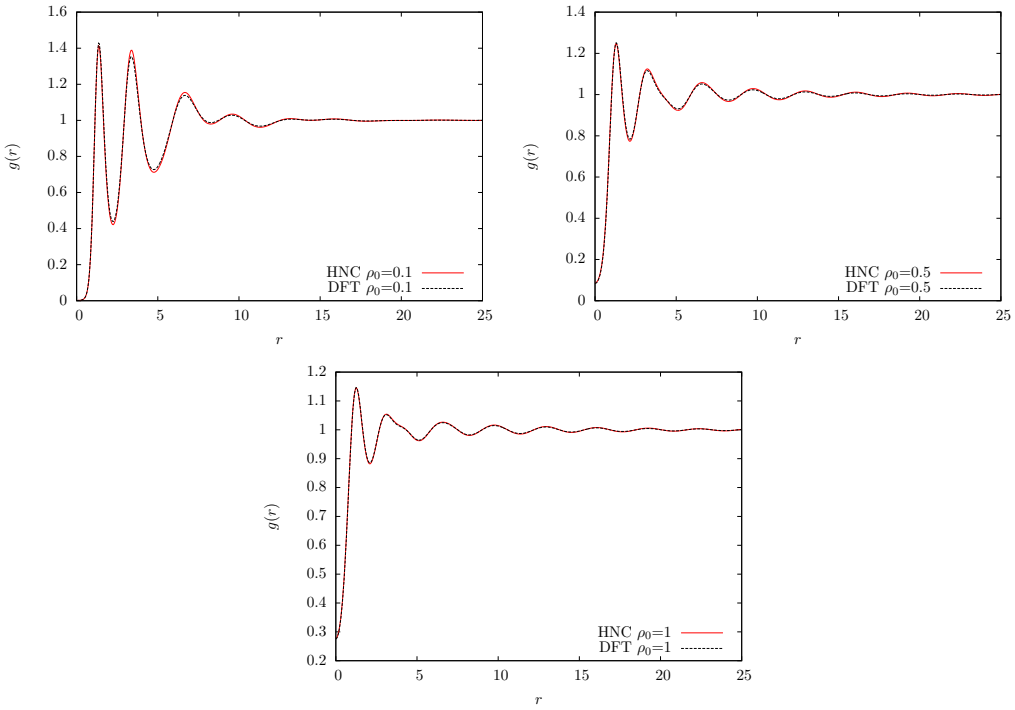

FIGURE 7.5: The radial distribution function $g(r)$, for $C_4 = 0.42$, $\beta\epsilon = 10$ and for the densities $\rho_0 = 0.1, 0.5$ and 1. We see good agreement between the HNC and the RPA-DFT test particle results.

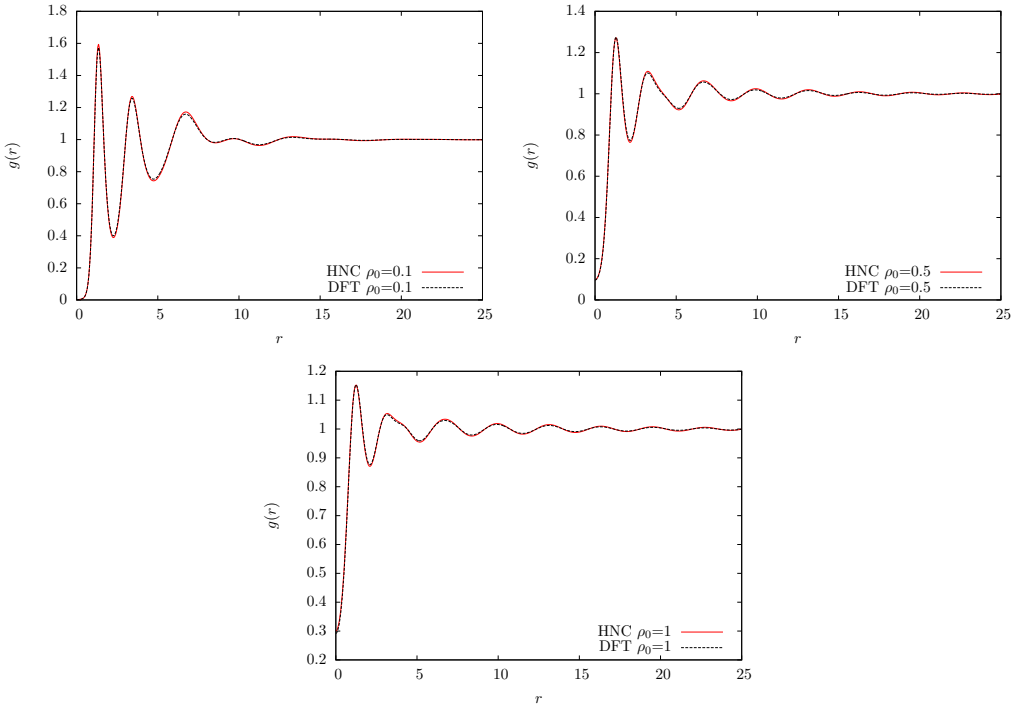

FIGURE 7.6: The radial distribution function $g(r)$, for $C_4 = 0.43$, $\beta\epsilon = 10$ and for the densities $\rho_0 = 0.1, 0.5$ and 1. We see good agreement between the HNC and the RPA-DFT test particle results.

(the Fisher-Widom line), the $r \to \infty$ asymptotic decay of $h(r)$ changes from monotonic and oscillatory decay [91]. This crossover can be understood by studying the poles in the complex plane of a certain contour integral which we discuss later in this chapter. The full theory of the asmptotic decay of $h(r)$ was worked out later by Evans *et al.* [92, 93]. In the BEL model, we do not observe a Fisher-Widom line. However, we do observe a crossover from oscillatory decay with one wavelength, to oscillatory decay with a different wavelength. This has been observed once perviously for a system that forms clusters, where one of the oscillatory wavelengths is from the packing of the particles and the other is from the cluster-cluster correlations [94]. What we observe here is different: both wavelengths are inter-particle length scales. These are the two length-scales required for QC formation. In the following section we review the theory of the asymptotic decay of $h(r)$ for 3D fluids, before generalising to 2D, the case of interest here, in order to understand the decay of $g(r)$ for the BEL model liquid in more detail.

7.3 Analysis of the asymptotic decay of $h(r)$ in 3D

In the following we review the analysis of the asymptotic decay of $h(r)$ for 3D fluids, following the presentation in Ref. [93]. We then show how to extend the arguments to a fluid in 2D. We begin by rearranging Eq. (2.28), the Ornstein-Zernike equation in Fourier space, to obtain:

$$\hat{h}(k) = \frac{\hat{c}(k)}{1 - \rho_0 \hat{c}(k)}. \tag{7.4}$$

This gives us an expression for the total correlation function in Fourier space $\hat{h}(k)$, in terms of the Fourier transform of the pair direct correlation function $\hat{c}(k)$. We seek an expression for $h(r)$ in real space, and in particular the asymptotic decay form for $r \to \infty$. Taking the inverse Fourier transform and noting that $\hat{h}(k)$ is even, it follows from Eq. (7.4) that [93]:

$$\begin{aligned} h(r) &= \frac{1}{2\pi^2} \int_0^\infty dk \, \left[k \sin(kr) \hat{h}(k) \right] \\ &= \frac{1}{4\pi^2 i} \int_{-\infty}^\infty dk \, \left[\frac{k e^{ikr} \hat{c}(k)}{1 - \rho_0 \hat{c}(k)} \right] \end{aligned} \tag{7.5}$$

The integral in Eq. (7.5) can be evaluated by performing a contour integral in the complex plane. The contour used is illustrated in Fig. 7.7. It consists of the semi-circle in the upper half of the complex plane and it gives the required integral in the limit of the radius of the circle $R \to \infty$, since the integral along the arc of the circle contributes zero to the contour integration in this limit. Using the residue theorem we can therefore transform the integral in Eq. (7.5) into a sum of residues of poles in the upper half of the complex plane. The poles of the integrand of the right hand side of Eq. (7.5) can be found by finding the zeros of the denominator. The poles occur at complex $k = q = \alpha_1 + i\alpha_0$ satisfying:

$$1 - \rho_0 \hat{c}(q) = 0. \tag{7.6}$$

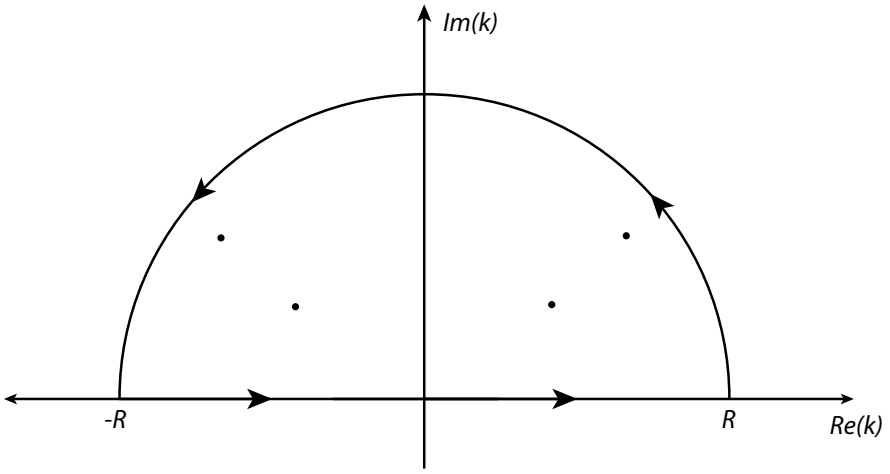

FIGURE 7.7: The contour integral in the complex-k plane used to evaluate the integral in Eq. (7.5). The points indicate the typical location of poles.

For many systems there are two kinds of solution to Eq. (7.6): there can be purely imaginary poles, lying on the imaginary axis having $\alpha_1 = 0, \alpha_0 \neq 0$. As we show below, this leads to purely exponential asymptotic decay of $h(r)$ [93]. The poles can also be complex, where they occur as a pair $q = \pm\alpha_1 + i\alpha_0$, with $\alpha_1 \neq 0$ and $\alpha_0 \neq 0$. These lead to oscillatory decay in $h(r)$ [93, 95]. In general, there are infinitely many poles. However, it is the pole(s) with the smallest imaginary part α_0 that determines the asymptotic decay of $h(r)$ as $r \to \infty$.

This switching between purely exponential decay and oscillatory decay dominating for $r \to \infty$ marks the Fisher-Widom line since the value of α_1, α_0 is determined by the location in the phase diagram. In the case of the BEL potential, all the poles lie off the imaginary axis and so give rise to exponentially damped oscillatory decay. In 3D the poles can be found by solving the following pair of equations [93]:

$$1 = 4\pi\rho_0 \int_0^\infty dr \left[r^2 c(r) \frac{\sinh(\alpha_0 r)}{\alpha_0 r} \cos(\alpha_1 r) \right] \tag{7.7}$$

and

$$1 = 4\pi\rho_0 \int_0^\infty dr \left[r^2 c(r) \cosh(\alpha_0 r) \frac{\sin(\alpha_1 r)}{\alpha_1 r} \right], \tag{7.8}$$

which follow by equating the real and imaginary parts in Eq. (7.6). Once the poles have been found we can sum over the residues to obtain:

$$rh(r) = \frac{1}{2\pi} \sum_n e^{iq_n r} R_n, \tag{7.9}$$

where q_n is the nth pole and R_n is the residue of $\frac{q_n \hat{c}(k)}{1-\rho_0 \hat{c}(k)}$ at $k = q_n$. Thus we see from Eq. (7.9) that for $r \to \infty$ the largest contribution comes from the pole with smallest imaginary part α_0. When the pole with the smallest imaginary part is purely imaginary then one finds the following monotonic asymptotic decay form

$$h(r) \sim \frac{A}{r} e^{-\alpha_0 r}, \tag{7.10}$$

for $r \to \infty$, where the amplitude $A = -i\alpha_0/2\pi\rho^2 \hat{c}'(i\alpha_0)$ [93]. On the other hand, when it is a pair of complex poles at $q = \pm\alpha_1 + i\alpha_0$ that are the poles with the smallest α_0, then the residues sum together to give the following asymptotic decay form for $h(r)$:

$$h(r) \sim \frac{2|A|}{r} e^{-\alpha_0 r} \cos(\alpha_1 r - \theta), \tag{7.11}$$

where $\alpha_1 > 0$ is the magnitude of the real part of the pair of poles and the amplitude A and the phase θ can be obtained from R_n and are given in Ref. [93].

7.4 Asymptotic decay in a 2D fluid

We now consider the same scenario but for a 2D system. The Fourier transform $\hat{f}(k)$ of a function $f(r)$ in 2D is defined as:

$$\hat{f}(k) = \int_{-\infty}^{\infty} dx \int_{-\infty}^{\infty} dy\, e^{-i\mathbf{k}\cdot\mathbf{r}} f(r). \tag{7.12}$$

Note that we have assumed that $f(\mathbf{r}) = f(r)$ is a circularly symmetric function that only depends on the magnitude $|\mathbf{r}| = r$. Now consider Eq (7.12) in polar coordinates:

$$\hat{f}(k) = \int_{0}^{\infty} dr \int_{0}^{2\pi} d\theta\, r e^{-i\mathbf{k}\cdot\mathbf{r}} f(r). \tag{7.13}$$

We recall that $J_0(kr) = \int_0^{2\pi} d\theta e^{-i\mathbf{k}\cdot\mathbf{r}}$ is the the zeroth Bessel function of the first kind. The angular integral can be evaluated to give the zero-order Hankel transform, also known as the Fourier-Bessel transform:

$$\hat{f}(k) = \int_{0}^{\infty} dr\, r J_0(kr) f(r). \tag{7.14}$$

The inverse transform is:

$$f(r) = \frac{1}{2\pi} \int_{0}^{\infty} dk\, k J_0(kr) \hat{f}(k). \tag{7.15}$$

Thus, from Eqs. (7.4) and (7.15) we get:

$$h(r) = \frac{1}{2\pi} \int_{0}^{\infty} dk\, \left[k J_0(kr) \frac{\hat{c}(k)}{1 - \rho_0 \hat{c}(k)} \right]. \tag{7.16}$$

The integrand of Eq. (7.16) is odd, so we can not immediately extend the limits and use the contour in Fig. 7.7 as we did to evaluate the integral in Eq. (7.5). To

proceed we first recall the following asymptotic expansion for the Bessel function

$$\begin{aligned} J_0(kr) &= \sqrt{\frac{2}{\pi kr}} \sin\left(kr + \frac{\pi}{4}\right) + \mathcal{O}\left(\frac{1}{r^{\frac{3}{2}}}\right) \\ &= \sqrt{\frac{2}{\pi kr}} \Re\left[-ie^{i(kr+\frac{\pi}{4})}\right] + \mathcal{O}\left(\frac{1}{r^{\frac{3}{2}}}\right) \\ &= \frac{1}{\sqrt{\pi kr}} \Re\left[(1-i)e^{ikr}\right] + \mathcal{O}\left(\frac{1}{r^{\frac{3}{2}}}\right), \end{aligned}$$

where $\Re[z]$ denotes the real part of the complex number z. Substituting the above into Eq. (7.16) we get:

$$h(r) = \frac{1}{2(\pi^3 r)^{\frac{1}{2}}} \Re\left[(1-i)\int_0^\infty dk\, k^{\frac{1}{2}} e^{ikr} \frac{\hat{c}(k)}{1-\rho_0\hat{c}(k)}\right] + \mathcal{O}\left(\frac{1}{r^{\frac{3}{2}}}\right). \tag{7.17}$$

We want to know the form of the asymptotic decay of the correlation function $h(r)$ for $r \to \infty$. Thus, we seek to evaluate the integral

$$I = \int_0^\infty dk\, k^{\frac{1}{2}} e^{ikr} \frac{\hat{c}(k)}{1-\rho_0\hat{c}(k)}. \tag{7.18}$$

To do this, we make the substitution $k = \chi^2$. This gives $dk = 2\chi d\chi$ and therefore

$$I = 2\int_0^\infty d\chi\, \chi^2 e^{i\chi^2 r} \frac{\hat{c}(\chi^2)}{1-\rho_0\hat{c}(\chi^2)}. \tag{7.19}$$

Since the argument of the above integral is an even function of χ we can change the limits and evaluate the integral as follows:

$$I = \int_{-\infty}^\infty d\chi\, \chi^2 e^{i\chi^2 r} \frac{\hat{c}(\chi^2)}{1-\rho_0\hat{c}(\chi^2)}. \tag{7.20}$$

We have now transformed the integral into a form that can be done in a manner that is analogous to the case in 3D, i.e. along the contour in Fig. 7.7, which is a semicircular contour in the upper half of the complex plane. Thus, the integral I can be evaluated as a sum over residues of poles in the upper half of the complex plane.

The poles of the integrand on the right hand side of Eq. (7.20) can be found by finding the zeros of the denominator, i.e. from Eq. (7.6) with $\chi^2 = q$. Again, it is the pole(s) with the smallest imaginary part α_0 that determine the asymptotic decay form. If the pole is purely imaginary, and assuming it is a simple pole, then the asymptotic decay form for the 2D fluid is [c.f. Eq. (7.10)]

$$h(r) \sim \frac{A}{\sqrt{r}} e^{-\alpha_0 r}, \tag{7.21}$$

for $r \to \infty$. On the other hand, when it is a pair of complex poles $\alpha = \pm\alpha_1 + i\alpha_0$ that are the poles with the smallest α_0, then assuming they are simple poles we obtain the following asymptotic decay form for $h(r)$ [c.f. Eq. (7.11)]:

$$h(r) \sim \frac{A}{\sqrt{r}} e^{-\alpha_0 r} \cos(\alpha_1 r - \theta). \tag{7.22}$$

In the BEL model all the poles are complex, so it is the asymptotic decay form in Eq. (7.22) that is relevant. As discussed in Sec. 7.1 modes with two distinct wave numbers interact to form QC structures. We show below that these two distinct wavelengths correspond to two distinct pairs of complex poles $\alpha^{(1)} = \pm\alpha_1^{(1)} + i\alpha_0^{(1)}$ and $\alpha^{(2)} = \pm\alpha_1^{(2)} + i\alpha_0^{(2)}$ with different α_1's, i.e. $\alpha_1^{(1)} \neq \alpha_1^{(2)}$, but with similar values of α_0, i.e. $\alpha_0^{(1)} \approx \alpha_0^{(2)}$ so that they both contribute to the asymptotic decay of $h(r)$. When $\frac{\alpha_1^{(1)}}{\alpha_1^{(2)}} = \frac{k_1}{k_2} = 0.5176$, i.e. the ratio discussed in Sec. 7.1.1, then we have the signature in the liquid state $h(r)$ of a system that forms QC in the solid state.

To calculate the position of the poles we solve numerically using a Newton Raphson method. This involves finding the solutions to the simultaneous equations $\Re[1 - \rho_0 \hat{c}(\alpha)] = 0$ and $\Im[1 - \rho_0 \hat{c}(\alpha)] = 0$ with $\alpha = \alpha_1 + i\alpha_0$. A selection of the lowest lying poles – those with smallest α_0 – are displayed in Fig. 7.8, for various different state points.

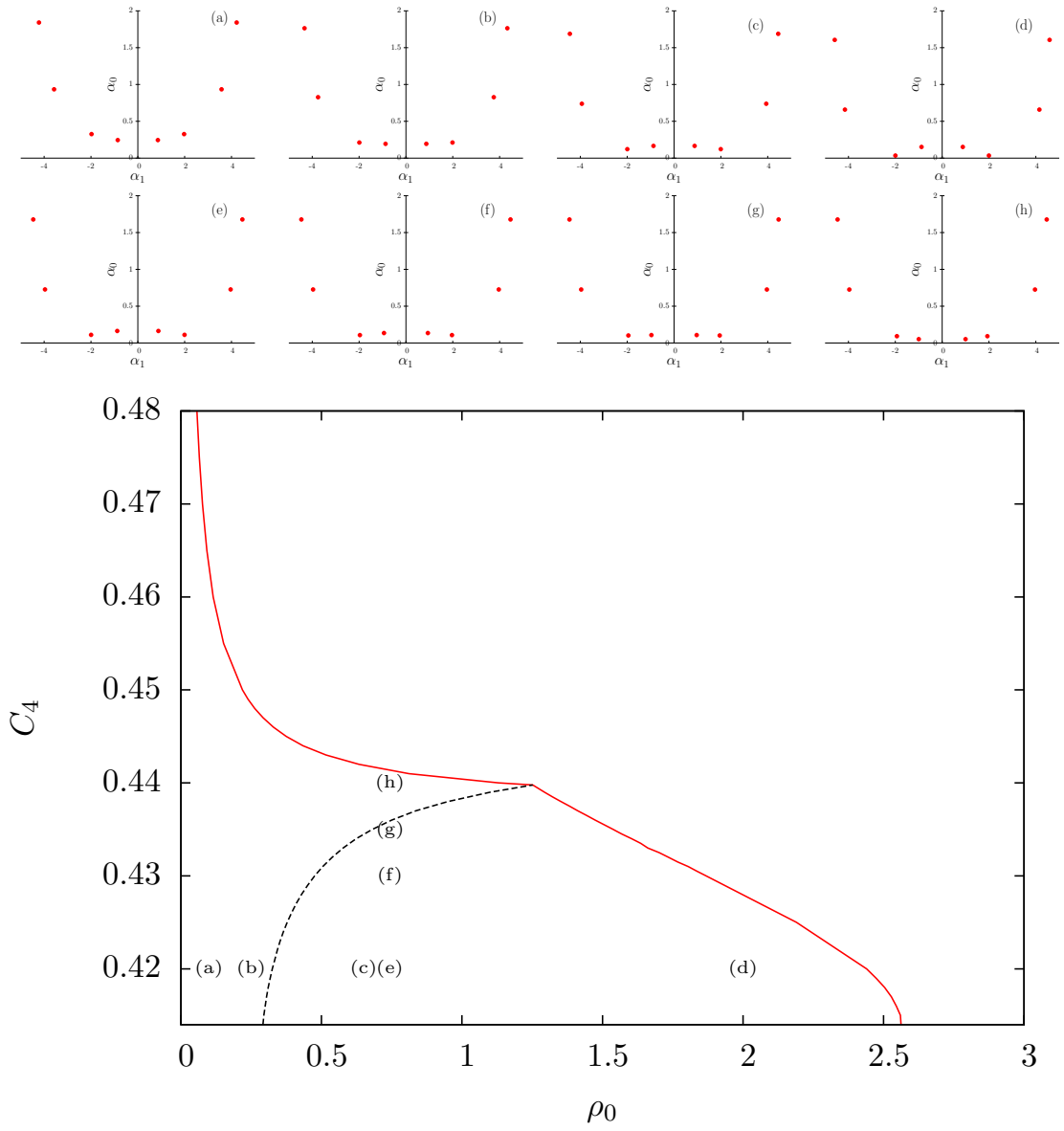

FIGURE 7.8: In the first two rows we display the lowest lying poles in the complex plane for various state points: (a)–(d) are are all for $C_4 = 0.42$ and for various densities: (a) $\rho_0 = 0.1$, (b) $\rho_0 = 0.25$, (c) $\rho_0 = 0.65$ and (d) $\rho_0 = 2$. (e)–(h) are all for the density $\rho_0 = 0.744$ and for various values of C_4: (e) $C_4 = 0.42$, (f) $C_4 = 0.43$, (g) $C_4 = 0.435$ and (h) $C_4 = 0.44$. At the bottom is the phase diagram in the density ρ_0 versus C_4 plane, showing the location of state points (a)-(f) and also the linear instability line (red) where the uniform fluid becomes linearly unstable and the dashed line is where the two leading order pairs of poles have the same value of α_0, i.e. the same decay range.

In Fig. 7.8 we see a selection of results showing how the pole structure changes as we vary C_4 and the density ρ_0. In the figure at the bottom is the phase diagram showing the linear instability line (red solid line) which is the line along which the uniform fluid becomes linearly unstable. Thus, the solid phase(s) are the equilibrium states of the system to the right of this line and also someway to the left of this line too. The overall shape of the phase diagram is very similar to that of the system studied in Refs. [44, 76], where the parameter C_4 plays a role similar to the parameter a in these works, i.e. a is the height of a shoulder in the pair potential. To the left of the red line in Fig. 7.8 the uniform liquid is linearly stable and sufficiently far from the line it is the thermodynamic equilibrium state. The plots of the poles in the α_1 versus α_0 plane in Fig. 7.8(a)–(h) show that as we move around the phase diagram the poles change their locations. In order to discuss Fig. 7.9, we must first define the following terms: 'inner' as the pair of poles closest to the α_0 axis and 'outer' as the next closest pair of poles to the α_0 axis. If we consider a horizontal line across Fig. 7.8 at $C_4 = 0.42$, the poles along this line vary as we increase the density. This can be seen in Fig. 7.9. The inset of Fig. 7.9 shows the change in α_1 and the main plot shows the change in α_0 as we increase the density along the line $C_4 = 0.42$. We observe in Fig. 7.9 a crossover between the 'inner' and 'outer' poles at $\rho_0 \approx 0.35$. The effect that this crossover has on the arrangement of the poles can be seen if we compare (b) and (c) in Fig. 7.8. Fig. 7.8 (b) shows the 'inner' poles have the lowest value of α_0, however Fig. 7.8 (c) shows the 'outer' poles have the lowest value of α_0. We see that the 'outer' poles have a value of α_1 that is almost double that of the 'inner' poles. This observation is important because if we consider Eq. (7.22), doubling the value of α_1, corresponds to halving the wavelength in the oscillatory decay of $h(r)$. In Figs. 7.10 and Fig. 7.11 we see plots of $\ln[\sqrt{r}h(r)]$ which highlights the asymptotic decay of $h(r)$. This shows the 'Full function' (calculated using the RPA-DFT test particle method) and compares with the 'Leading pole' [Eq. (7.22)]. The plots in Fig. 7.10 show the decay of $h(r)$ for two low density points within the region in Fig. 7.8, where the 'inner' poles have the lowest value of α_0 and so dominate the

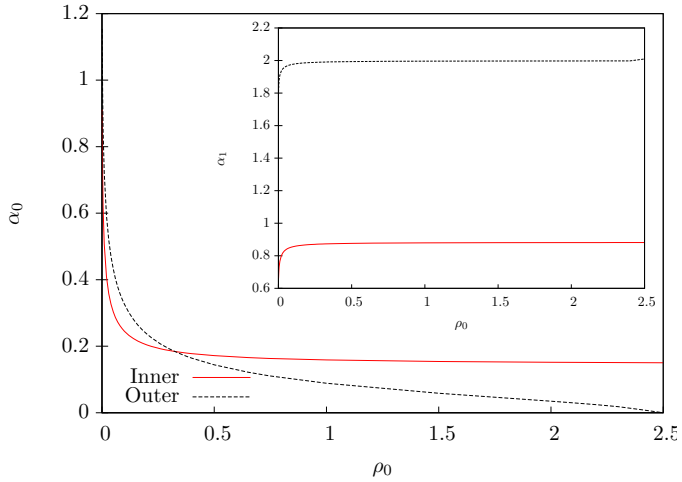

FIGURE 7.9: Plot showing the change in the value of α_0 for the 'inner' (red) and the 'outer' (green) poles as we increase the density for $C_4 = 0.42$. Inset: Plot showing the corresponding value of α_1.

asymptotic decay. The plots in Fig. 7.11 show the decay of $h(r)$ for two points within the region in Fig. 7.8, where the 'outer' poles have the lowest value of α_0. In comparing these two figures, we can clearly see the change in the wavelength of the oscillations. The initial disagreement in Figs. 7.10-7.11 is expected at small values of r since the results in Eqs. (7.21) and (7.22) are asymptotic $r \to \infty$ results. In the $0 < r < 20$ region we expect that contributions from the second and higher order poles will also effect the shape of the decay. For $r > 20$ we have generally good agreement between the full numerical result and the asymptotic form determined by the leading order poles.

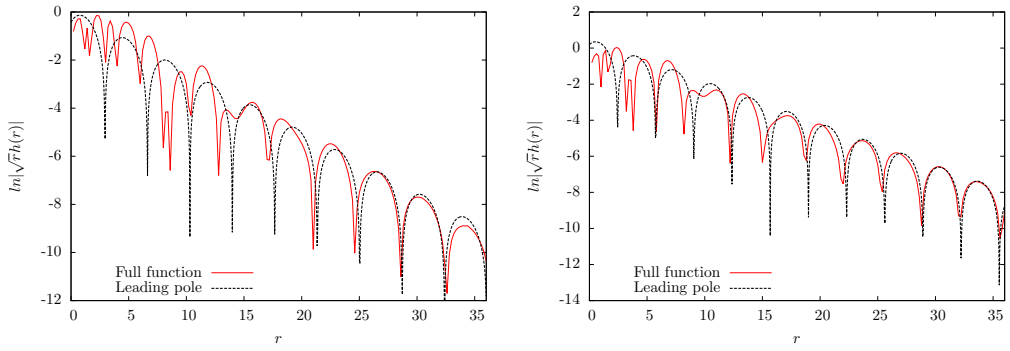

FIGURE 7.10: Plots of $\ln[\sqrt{r}h(r)]$ vs r which highlights the asymptotic decay of $h(r)$. This is compared with the form from the leading order pole in Eq. (7.22), from solving (7.6) and matching the amplitude and phase in (7.22) by eye. These plots are both from a region of the phase diagram Fig. 7.8 where the 'inner' pole is leading order. The left hand plot has $\beta\epsilon = 10$, $C_4 = 0.42$, $\rho_0 = 0.09$ and leading order pole with values $\alpha_0 = 0.2528$ and $\alpha_1 = 0.8535$. The right hand plot has $\beta\epsilon = 10$, $C_4 = 0.44$, $\rho_0 = 0.08$ and leading order pole with values $\alpha_0 = 0.2424$ and $\alpha_1 = 0.9037$.

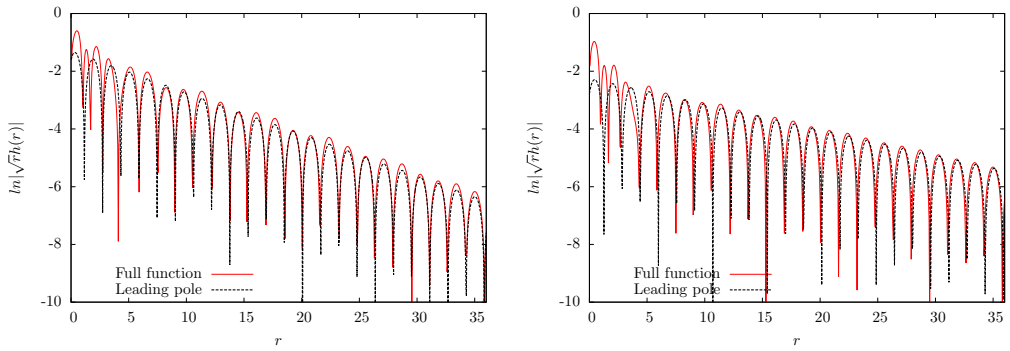

FIGURE 7.11: Plots of $\ln[\sqrt{r}h(r)]$ vs r which highlights the asymptotic decay of $h(r)$. This is compared with the form from the leading order pole in Eq. (7.22), from solving (7.6) and matching the amplitude and phase in (7.22) by eye. These plots are from a region of the phase diagram Fig. 7.8 where the 'outside' pole is leading order. The left hand plot has $\beta\epsilon = 10$, $C_4 = 0.42$, $\rho_0 = 0.5$ and leading order pole with values $\alpha_0 = 0.0888$ and $\alpha_1 = 1.996$. The right hand plot has $\beta\epsilon = 10$, $C_4 = 0.42$, $\rho_0 = 1$ and leading order pole with values $\alpha_0 = 0.1440$ and $\alpha_1 = 1.993$.

7.5 Concluding remarks

In this chapter we have introduced the BEL potential (7.1) and reviewed why it forms QCs and other crystalline structures. The formation of a QC with 12-fold symmetry was demonstrated using DDFT, illustrating the effect that competing length scales can have in the creation of crystalline structures. These competing length scales are generated by the structured shape of the BEL potential, whose form gives a high level of control and precision over the length scales that emerge. The leading order density modes that correspond to these length scales interact with one another, reenforcing specific wave numbers.

The main interest here is in the liquid state structure of the BEL model. We have compared the RPA-DFT and the HNC approximations for the liquid state structure. There is good agreement between the two theories even though the BEL potential is highly structured. The theory for the asymptotic decay of $h(r)$ is well understood and extensively studied for fluids in 3D. We have briefly reviewed this theory (see also Ref. [93]) before then generalising these results for fluids in 2D. Our analysis shows that in 2D, like in 3D, the asymptotic decay $r \to \infty$ of $h(r)$ is determined by the contribution from the pole(s) with the smallest value of α_0. Applying this theory to the BEL model shows that the asymptotic decay of $h(r)$ can vary significantly, depending on the state point in the phase diagram. There are two pairs of poles that can dominate the asymptotic decay. We find that moving from one point in the phase diagram to another can lead to a crossover in the asymptotic decay form of $h(r)$ from oscillatory decay with one wavelength to oscillatory decay with a very different wavelength, that is almost double. Plotting $\ln[\sqrt{r}h(r)]$ we see that there is good agreement between the full function and the leading order pole approximation when $r > 20$.

The two length scales that define the wavelength of the oscillations in the asymptotic decay of $h(r)$ are important, because it is the interplay of these two length scales that leads to QC formation. The line in the portion of the phase

diagram where the liquid is the stable phase (dashed black line in Fig. 7.8), where these two decay forms contribute equally, leads directly to the state point where the system becomes marginally unstable at two length scales. This is also the point in the phase diagram where QC occur. Thus, our results show that a good strategy for finding state points where QC form is to examine the liquid state correlations and to seek for where the asymptotic decay contribution with the two characteristic length-scales with ratio approximately 1:1.93 have decay lengths that are equal and then to follow the line in the phase diagram towards where the solid phase occurs, keeping these two asymptotic decay contribution with the same decay length. Doing that will lead to state points where QC formation is likely.

Chapter 8

Final Remarks

In this thesis we have studied the dynamics of freezing of systems of interacting soft-core particles. The particular situation we have discussed in detail is the process of solidification in the aftermath of a quench. Much attention was given to the solidification via a front advancing into the unstable uniform liquid. We have shown how the front speed and wave number for the density modulations in the particle density distribution created by the front can be calculated. We have demonstrated that the wavelength of these may not match the length scale corresponding to the equilibrium crystal structure. This discrepancy between the length scale dynamically chosen by the front and the equilibrium crystal length scale (i.e. the lattice spacing), can lead to disorder in the crystalline structure that is formed. However, there are other ways competing length scales can be generated within a system that are also discussed: (i) in a binary system, competing length scales arise from the different sizes of the particles and the different competing crystal structures that the system can potentially form. (ii) In a system where the particle interactions exhibit more than one length scale, such as the BEL model studied in Chapter 7, there can also be more than one competing length scale. This manifests in a dispersion relation, which can have more than one maxima and possibly more than one simultaneously unstable wave numbers. These different length-scales can lead to disorder in the crystalline structures that are formed and so they contain no long range order, even after the system has finally

finished evolving to equilibrium, which, due to the disorder and complex underlying free energy landscape, can take a long time to equilibrate. In some of these systems, and under very specific conditions QC's can be created and stabilised.

Our detailed study of solidification fronts in two particular systems, the first a single component system and the second, a binary mixture, shows considerable differences in the crystal structure left behind by the front. There are also crucial differences in both the short time and the long time evolution that are immediately apparent. The crystal structure of the one component system has some defects present immediately after the passage of the front, but most of these defects disappear shortly after the front has passed through the system. In contrast, in the binary model the defects created by the front do not disappear and remain prevalent through out the crystal structure, even at long times. The defects in both cases arise from the front selecting a length scale not equal to that corresponding to the equilibrium crystal structure. However, unlike in the single species system, the defects in the binary systems remain long after the front has passed and often even indefinitely. This can be attributed to competing low energy structures that arise from the differing sizes in the particles.

We have also considered the structure of the liquid phase of these soft-core systems. We have used the 'test particle' method together with the RPA-DFT in order to calculate the correlation functions for the liquid state. Comparing the accuracy of the RPA-DFT with the HNC approximation to the OZ equation, we find that the RPA-DFT is remarkably accurate, even at low density and also for the more complicated and highly structured BEL potential. This shows that it is not only the crystal structure of the frozen system which is affected by the competing length scales. The competing lengths scales are also present in the liquid state particle correlations. This can most clearly be seen when we perform an asymptotic analysis of the total correlation function $h(r)$, to understand the decay for $r \to \infty$. In order to do this we had to generalise to 2D the approach known for 3D. Studying the BEL potential model, we observed a crossover in the asymptotic decay from damped oscillatory with one wavelength to damped oscillatory with

a different wavelength. This is the first observed example of structural crossover in a one-component fluid that is not of the type observed in systems that form clusters and exhibit micro-phase separation [94]. This study has provided good insight for what features to look for in the liquid state correlations if the goal is to find new systems that exhibit QC formation.

The results presented in this thesis for a variety of different systems of soft core particles show that in contrast to what one might initially assume, namely that such systems can not exhibit much structure due to the soft penetrable cores and fairly weak interactions, in actual fact these systems of particles act collectively to form highly correlated complex structures, including QC.

Appendix A

Picard iteration

The Picard iterative process is a numerical method for solving the equations of equilibrium DFT. The method is discribed in Ref. [22, 23]. The basic idea is as follows. We take the Euler-Lagrange equation, for example Eq. (2.15):

$$\rho(\mathbf{r}) = \rho_0 e^{\int d\mathbf{r}' c^{(2)}(\mathbf{r},\mathbf{r}')(\rho(\mathbf{r}')-\rho_0)-\beta V_{ext}(\mathbf{r})}, \tag{A.1}$$

where ρ_0 is the bulk fluid density. We make an initial guess for the density profile $\rho^{n=0}(\mathbf{r})$, which we label with the index n. In some circumstances this might be the ideal gas profile i.e.

$$\rho^{n=0}(\mathbf{r}) = \rho_0 e^{-\beta V_{ext}(\mathbf{r})}, \tag{A.2}$$

or in other circumstances we choose $\rho^{n=0}(\mathbf{r}) = \rho_0 + \rho_r(\mathbf{r})$, where $\rho_r(\mathbf{r})$ is a small amplitude random field with $\frac{|\rho_r|}{\rho_0} << 1$. We then insert this initial guess into the right hand side of Eq. (A.1) in order to generate a density profile $\rho^{n=0}_{sub}(\mathbf{r})$. We then mix a little of this new profile together with a majority of the old density profile to obtain our new guess. This is then iterated until convergence is achieved. Thus, we iterate:

$$\rho^{n+1}(\mathbf{r}) = m\rho^{n}_{sub}(\mathbf{r}) + (1-m)\rho^{n}(\mathbf{r}), \tag{A.3}$$

where the mixing parameter m is typically $0.2 > m > 0.001$. Convergence is determined by requiring that the integral $\int d\mathbf{r}(\rho^{n+1}(\mathbf{r})-\rho^{n}(\mathbf{r}))^2$ is a small quantity, typically $O(10^{-6})$.

Bibliography

[1] R. Evans, Advances in Physics **28**, 143 (1979).

[2] R. Evans, in *Fundamentals of Inhomogeneous Fluids*, edited by D. Henderson (CRC Press, New York, 1992), Chap. 3, pp. 85–175.

[3] I. R. McDonald J.-P. Hansen, *Theory of Simple Liquids*, 4th ed. (Elsevier, Oxford, 2013).

[4] J. F. Lutsko, Adv. Chem. Phys. **144**, 1 (2010).

[5] R. Evans, J. R. Henderson, and R. Roth, J. Chem. Phys. **121**, 12074 (2004).

[6] H. Löwen, Phys. Reports **237**, 249 (1994).

[7] C. N. Likos, Phys. Rep. **348**, 267 (2001).

[8] J. Dautenhahn and C. K. Hall, Macromolecules **27**, 5399 (1994).

[9] C. N. Likos, H. Löwen, M. Watzlawek, B. Abbas, O. Jucknischke, J. Allgaier, and D. Richter, Phys. Rev. Lett. **80**, 4450 (1998).

[10] A. A. Louis, P. G. Bolhuis, J.-P. Hansen, and E. J. Meijer, Phys. Rev. Lett. **85**, 2522 (2000).

[11] P. G. Bolhuis, A. A. Louis, J.-P. Hansen, and E. J. Meijer, J. Chem. Phys. **114**, 4296 (2001).

[12] A. Jusufi, J. Dzubiella, C. N. Likos, C. von Ferber, and H. Löwen, J. Phys.: Cond. Mat. **13**, 6177 (2001).

[13] J. Dzubiella, A. Jusufi, C. N. Likos, C. von Ferber, H. Löwen, J. Stellbrink, J. Allgaier, D. Richter, A. B. Schofield, P. A. Smith, W. C. K. Poon, and P. N. Pusey, Phys. Rev. E **64**, 010401(R) (2001).

[14] A. A. Louis, P. G. Bolhuis, R. Finken, V. Krakoviack, E. J. Meijer, and J.-P. Hansen, Physica A **306**, 251 (2002).

[15] C. N. Likos and H. M. Harreis, Cond. Mat. Phys. **5**, 173 (2002).

[16] I. O. Gotze, H. M. Harreis, and C. N. Likos, J. Chem. Phys. **120**, 7761 (2004).

[17] B. M. Mladek, M. J. Fernaud, G. Kahl, and M. Neumann, Cond. Mat. Phys. **8**, 135 (2005).

[18] C. N. Likos, Sof. Mat. **2**, 478 (2006).

[19] D. A. Lenz, R. Blaak, C. N. Likos, and B. M. Mladek, Phys. Rev. Lett. **109**, 228301 (2012).

[20] F. H. Stillinger, J. Chem. Phys. **65**, 3968 (1976).

[21] P. G. Bolhuis, A. A. Louis, J. P. Hansen, and E. J. Meijer, J. Chem. Phys. **114**, 4296 (2001).

[22] R. Roth, J. Phys.: Cond. Mat. **22**, 063102 (2010).

[23] A. P. Hughes, U. Thiele, and A. J. Archer, American Journal of Physics **82**, 1119 (2014).

[24] A. L. Thorneywork, R. Roth, D. G. A. L. Aarts, and R. P. A. Dullens, J. Chem. Phys. **140**, 161106 (2014).

[25] A.J.Archer, B. Chacko, and R. Evans, J. Chem. Phys. **147**, 034501 (2017).

[26] J. K. Percus, Phys. Rev. Lett. **8**, 462 (1962).

[27] S. Prestipino and F. Saija, J. Chem. Phys. **141**, 184502 (2014).

[28] A. J. Archer, M. C. Walters, U. Thiele, and E. Knobloch, Phys. Rev. E **90**, (2014).

[29] A. J. Archer and R. Evans, Phys. Rev. E **64**, 041501 (2001).

[30] A. J. Archer and R. Evans, J. Phys.: Cond. Mat. **14**, 1131 (2002).

[31] A. J. Archer, R. Evans, and R. Roth, Europhys. Lett. **59**, 526 (2002).

[32] A. J. Archer, C. N. Likos, and R Evans, J. Phys.: Cond. Mat. **14**, 12031 (2002).

[33] A. J. Archer, C. N. Likos, and R Evans, J. Phys.: Cond. Mat. **16**, L297 (2004).

[34] I. O. Gotze, A. J. Archer, and C. N. Likos, J. Chem. Phys. **124**, 084901 (2006).

[35] B. M. Mladek, D. Gottwald, G. Kahl, M. Neumann, and C. N. Likos, Phys. Rev. Lett. **96**, 045701 (2006).

[36] B. M. Mladek, D. Gottwald, G. Kahl, M. Neumann, and C. N. Likos, J. Phys. Chem. B **111**, 12799 (2007).

[37] A. J. Moreno and C. N. Likos, Phys. Rev. Lett. **99**, 107801 (2007).

[38] C. N. Likos, B. M. Mladek, D. Gottwald, and G. Kahl, J. Chem. Phys. **126**, 224502 (2007).

[39] B. M. Mladek, P. Charbonneau, C. N Likos, D. Frenkel, and Ge. Kahl, J. Phys.: Cond. Mat. **20**, 494245 (2008).

[40] C. N. Likos, B. M. Mladek, A. J. Moreno, D. Gottwald, and G. Kahl, Comp. Phys. Comm. **179**, 71 (2008).

[41] S. D. Overduin and C. N. Likos, J. Chem. Phys. **131**, 034902 (2009).

[42] S. D. Overduin and C. N. Likos, Europhys. Lett. **85**, 26003 (2009).

[43] S. van Teeffelen, A. J. Moreno, and C. N. Likos, Sof. Mat. **5**, 1024 (2009).

[44] M. Camargo, A. J. Moreno, and C. N. Likos, J. Stat. Mech.: Theory and Exp. **2010**, P10015 (2010).

[45] M. Camargo and C. N. Likos, Mol. Phys. **109**, 1121 (2011).

[46] A. Nikoubashman, G. Kahl, and C. N. Likos, Sof. Mat. **8**, 4121 (2012).

[47] M. Carta, D. Pini, A. Parola, and L. Reatto, J. Phys.: Cond. Mat. **24**, 284106 (2012).

[48] D Pini, Trans. R. Norw. Soc. Sci. Lett. **3**, 99 (2014).

[49] A. J. Archer, A. M. Rucklidge, and E. Knobloch, Phys. Rev. Lett. **111**, 165501 (2013).

[50] U. M. B. Marconi and P. Tarazona, J. Chem. Phys. **110**, 8032 (1999).

[51] A. J. Archer and M. Rauscher, J. Phys. A: Math. Gen. **37**, 9325 (2004).

[52] A. J. Archer and R. Evans, J. Chem. Phys. **121**, 4246 (2004).

[53] A. J. Archer, M. J. Robbins, U. Thiele, and E. Knobloch, Phys. Rev. E **86**, 031603 (2012).

[54] J. Berry, M. Grant, and K. R. Elder, Phys. Rev. E **73**, 031609 (2006).

[55] K. R. Elder, M. Katakowski, M. Haataja, and M. Grant, Phys. Rev. Lett. **88**, 245701 (2002).

[56] K. R. Elder and M. Grant, Phys. Rev. E **70**, 051605 (2004).

[57] S. van Teeffelen, R. Backofen, A. Voigt, and H. Löwen, Phys. Rev. E **79**, 051404 (2009).

[58] M. J. Robbins, Ph.D. thesis, Loughborough University, 2012.

[59] P. C. Hohenberg and B. I. Halperin, Rev. Mod. Phys. **49**, 435 (1977).

[60] P. K. Galenko and K. R. Elder, Phys. Rev. B **83**, 064113 (2011).

[61] G. Dee and J. S. Langer, Phys. Rev. Lett. **50**, 383 (1983).

[62] E. Ben-Jacob, H. Brand, G. Dee, L. Kramer, and J. S. Langer, Physica D **14**, 348 (1985).

[63] A. Hari and A. A. Nepomnyashchy, Phys. Rev. E **61**, 4835 (2000).

[64] A. Couairon and J.-M. Chomaz, Physica D **108**, 236 (1997).

[65] W. van Saarloos, Phys. Reports **386**, 29 (2003).

[66] G. Tegze, L. Granasy, G. I. Toth, J. F. Douglas, and T. Pusztai, Sof. Mat. **7**, 1789 (2011).

[67] A. Doelman, B. Sandstede, A. Scheel, and G. Schneider, Euro. J. Appl. Math. **14**, 85 (2003).

[68] M. de Berg, O. Cheong, M. van Kreveld, and M. Overmars, *Computational Geometry: Algorithms and Applications*, 3 ed. (Springer-Verlag, Heidelberg, 2008).

[69] A. J. Archer, J. Phys.: Cond. Mat. **17**, 1405 (2005).

[70] A. J. Archer, J. Phys.: Cond. Mat. **17**, S3253 (2005).

[71] K. Barkan, M. Engel, and R. Lifshitz, Phys. Rev. Lett. **113**, 098304 (2014).

[72] D. Shechtman, I. Blech, D. Gratias, and J. W. Cahn, Phys. Rev. Lett. **53**, 1951 (1984).

[73] A. J. Archer, A. M. Rucklidge, and E. Knobloch, Phys. Rev. Lett. **111**, 165501 (2013).

[74] S. Kim, C. Kee, and J. Lee, Opt. Express **15**, 13221 (2007).

[75] Z. V. Vardeny, A. Nahata, and A. Agrawal, Nature Photonics **7**, 177 (2013).

[76] A. J. Archer, A. M. Rucklidge, and E. Knobloch, Phys. Rev. E **92**, 012324 (2015).

[77] W.S. Edwards and S. Fauve, Phys. Rev. E **R788**, (1993).

[78] S. Savitz, M. Babadi, and R. Lifshitz, J. Phys.: Cond. Mat. (2017).

[79] R. Lifshitz and D. M. Petrich, Phys. Rev. Lett. **79**, 1261 (1997).

[80] W. Zhang and J. Viñals, J. Fluid Mech. **336**, 301–330 (1997).

[81] C. M. Topaz, J. Porter, and M. Silber, Phys. Rev. E **70**, 066206 (2004).

[82] A. C. Skeldon and G. Guidoboni, Siam J. App. Math. **67**, 1064 (2007).

[83] A. M. Rucklidge and M. Silber, Siam J. App. Dyn. Sys. **8**, 298 (2009).

[84] A. M. Rucklidge, M. Silber, and A. C. Skeldon, Phys. Rev. Lett. **108**, 074504 (2012).

[85] R. Lifshitz and H. Diamant, Philo. Mag. **87**, 3021 (2007).

[86] M. Engel and H. Trebin, Phys. Rev. Lett. **98**, 225505 (2007).

[87] K. Barkan, H. Diamant, and R. Lifshitz, Phys. Rev. B **83**, 172201 (2011).

[88] J. Rottler, M. Greenwood, and B. Ziebarth, J. Phys.: Cond. Mat. **24**, 135002 (2012).

[89] P. Subramanian, A. J. Archer, E. Knobloch, and A. M. Rucklidge, Phys. Rev. Lett. **117**, 075501 (2016).

[90] S. Ranganathan and K. N. Pathak, Phys. Rev. A **45**, 5789 (1992).

[91] M. E. Fisher and B. Wiodm, J. Chem. Phys. **50**, 3756 (1969).

[92] R. Evans, J.R. Henderson, D.C. Hoyle, A.O. Parry, and Z.A. Sabeur, Mol. Phys. **80**, 755 (1993).

[93] R. Evans, R. J. F. Leote de Carvalho, J. R. Henderson, and D. C. Hoyle, J. Chem. Phys. **100**, 591 (1994).

[94] A. J. Archer, D. Pini, R. Evans, and L. Reatto, J. Chem. Phys. **126**, 014104 (2007).

[95] C. Vega, L. F. Rull, and S. Lago, Phys. Rev. E **51**, 3146 (1995).